Leveraging Efficient Physics-based Models for Insights into Lithium Sulfur Batteries

Caitlin D. Parke

A dissertation

Submitted in partial fulfillment of the

Requirements for the degree of

Doctor of Philosophy

University of Washington

2021

Reading Committee:

Venkat R. Subramanian, Chair

Daniel T. Schwartz, Chair

Jihui Yang

Program Authorized to Offer Degree:

Chemical Engineering

University of Washington

Abstract

Leveraging Efficient Physics-based Models for Insights into Lithium Sulfur Batteries

Caitlin D. Parke

Chairs of the Supervisory Committee:
Professor Venkat R. Subramanian
Professor Daniel T. Schwartz
Chemical Engineering

Energy storage is critical to adoption of renewables and combating climate change. As the burgeoning requirements for electric transportation outpace the current lithium-ion technology, the race to commercialize the next-generation battery is still ongoing. Lithium sulfur (LiS) is a promising candidate with a practical energy density predicted to be 2-3 times that of lithium-ion battery systems. However, LiS cells suffer from safety issues, poor cycle life, and low coulombic efficiency. Alongside materials science and cell engineering, physics-based modeling can be a powerful tool to analyze and interpret experimental data and guide design and identify optimal conditions. The power of physics-based models is the prediction of internal states that can contribute to degradation or performance. The prediction power of these models comes at high computational cost. The development of efficient yet accurate models for whole-cell predictions can aid experimental efforts through model-based design or parameter

estimation. Optimization calls of the model can number into the 1000s for each experiment, underpinning the importance of computational efficiency and speed. This work details a novel physics-based model that considers the battery as a series of connected tanks, resulting in a significant upgrade in speed compared to the conventional one-dimensional (1D) model for LiS batteries with similar predictive power. This suggests real potential for applications such as optimal charging, cell-balancing, and estimation. As new materials, coatings, and electrolyte systems are considered and tested, standardized cell conditions for LiS batteries are yet to be determined. This presents an exciting opportunity for modeling efforts to collaborate with experimentalists, in analyzing the effect of novel experiments and identifying important measurements to do next. The application of efficient models that incorporate experimental insights is the other focus of this work. The implications of radical anion formation on the current-voltage behavior are explored for the first time; parameters describing the dissociation reaction equilibrium and kinetics are shown to alter the electrolyte speciation in ways that can be linked to observations from LiS electrolyte engineering experiments. The efficient models are also utilized in characterizing pouch cells for electric flight in collaboration with BAE Systems and predicting the thermal behavior of an LiS sandwich cell. The culmination of this work is the ongoing collaboration with Pacific Northwest National Laboratory and Brookhaven National Laboratory to identify unknown XRD spectra through speciation insights gleaned from parameter estimation. These contributions represent a step forward in efforts to incorporate detailed and accurate electrochemical models for experimental insights and advanced Battery Management Systems for LiS batteries.

Table of Contents

List of Figures

List of Tables

Acknowledgments

I want to thank so many different people that have played a part in where I am today. First of all, I want thank my reading committee, Venkat R. Subramanian, Daniel T. Schwartz, and Jihui Yang for their guidance and support. I especially want to acknowledge my advisors. Venkat, thank you for the support and encouragement over the years on research and extracurricular activities that took me out of the lab. Dan, I have appreciated all of our stimulating conversations that helped shape my work in the past year.

To my lab members, you all not only helped me through this process but made it an enjoyable and enriching experience. Surya, Akshay, and Krishna, your help has been invaluable. Neal and TJ, thanks for always helping me with my many, many technical difficulties. To my Schwartz team, Victor, Erica, Mihyun, I will miss our group yoga and fun banter. Yanbo, Mengdi, and Maitri, thanks for being my ladies of the lab. Manan, thank you for the stimulating conversations and letting me rant when I needed it. Linnette, you have been such a great friend and research collaborator, and I owe you so much for motivating me and make me laugh when I really needed it. Sabiha, my first friend in Seattle, I have appreciated your cheerleading, coffee dates, and support.

To my best friends, Rosalee and Nicole, every step I have taken forward is with the knowledge of your love and support. To Biraj, there is no one else I want to talk through submissions of important papers or stress dilemmas than you; I hope to one day selflessly give of myself in the same way as you do. To my siblings, Cole, Caleb, and Chloe, you challenge me and make me better. To my parents, to whom I owe all my successes, this is as much your victory as it is mine.

Dedication

To my loving and dedicated parents

who always believed I could do anything,

you were right.

Chapter 1
Introduction

1.1 Lithium Sulfur Batteries

As energy requirements outpace advanced lithium-ion battery technology, lithium sulfur (LiS) has emerged as a promising candidate with a practical energy density predicted to be 2-3 times that of lithium-ion battery systems. Furthermore, sulfur is a cheap and abundant material, making it an alluring choice for both cost and supply chain stability. However, LiS cells suffer from the myriad of issues that have plagued the development and commercialization of lithium metal batteries; in the 1980s, a company specializing in lithium metal batteries folded after several explosive fires[1]. The sulfur cathode brings its own set of challenges to overcome, including an insulating active material, complex reduction scheme, and soluble and reactive. Overcoming the safety issues, poor cycle life, and low coulombic efficiency requires an arsenal of interdisciplinary work focusing on the interactions between the anode, cathode, and electrolyte system. Alongside materials science and cell engineering, physics-based modeling can be a powerful tool to analyze and interpret experimental data and guide design and identify optimal conditions.

1.2 Brief Literature Review of Physics-based Modeling for Lithium Sulfur Batteries

Predictive models are vital in accelerating the field. Physics-based continuum models

offer a glimpse into the internal states of the battery. Experimentalists have devised clever ways to probe these states, but they are both time-consuming and expensive. For example, the synchrotron at Brookhaven National Laboratory probes the material makeup of a sample through X-Ray diffraction, with a hefty price tag of almost $1 billion[2]. The importance of modeling becomes clear when the time and cost of experiments is factored in.

Fast yet accurate models can doubly help accelerate research through enabling model-based design and optimization. After model validation, a model can be used to search a parameter space dependent on material constraints and end use in mind. Models are also useful in interpretation of data and illuminating important next measurements and experiments.

Predictive models can help augment experimental work by elucidating the underlying mechanisms and exploring design space without the time and cost of experiments. One class of predictive models is electrochemical physics-based models, which give further insight into the internal states of the battery. The first physics-based model for lithium sulfur batteries was a 0D lumped model published in 2004[3]. The model included simple kinetic two-plateau mechanism and thermodynamics. In 2008, Kumaresan et al.[4] published a 1D mathematical model of lithium sulfur batteries. This model included transport in the cathode and separator and a more complex sulfur reduction scheme. The morphology of the battery is tracked through chemical dissolution and precipitation, and the diffusion effects are captured through a porosity evolution with time. A similar model was developed by Neidhardt et al.[5] in 2012. A series of papers were published with a similar 1D model that explored impedance[6], charging[7], and

degradation[8-10], lumped models with simplified reaction mechanisms and fewer parameters[11-13], and precipitation of lithium sulfide[14,15].

Most models have not been experimentally validated, and the ones that are compared to experiments generally over predict capacity and miss the transition between the two plateaus. Better model experimental agreement remains an important objective. Simplified models with fewer parameters have been developed specifically for ease of parameterization and computational efficiency. Although simpler models have faster solution times, the power of using physics-based models is the insight into the internal states of the battery, like overpotentials and concentrations. These internal states are directly affected by physical properties, like electrode length. The more complex 1D models are computationally intensive, which hinders the use in optimization tools where model calls can be up to the thousands. This work focuses on developing efficient physics-based models that maintain accuracy and predictive capabilities while also being computationally efficient enough for parameter estimation and design. With the use of these models, the development of experimentally-aligned tools for analyzing speciation and electrolyte engineering is discussed.

1.3 Thesis Roadmap

The focus of this work is twofold: developing efficient and accurate models for optimization and control and aligning modeling tools to the latest experimental insights to collaboratively accelerate the field. To that end, Chapter 2 details the development of the Tanks-in-Series (Tank) model for LiS batteries. This model bridges the gap between computationally efficient zero-dimensional (0D) models and the more complex one-

dimensional (1D) models that describe transport behavior and spatial phenomena. One advantage of 0D models is the ease of parameterization due to the lack of transport, and the other is the low computational footprint. The benefit of the Tank model is realized in the speed with the predictive power of the 1D model.

Chapter 3 details recent work that introduces new dissociation chemistry to understand the effect of electrolyte engineering. Experimental studies have identified a radical anion that some electrolyte systems stabilize identified in spectroscopic studies and identified by its unique blue color. This work includes the dissociation chemistry that produces the radical anion and explores the effects of the thermodynamics and kinetics on the voltage performance under different conditions. This work utilizes the 1D model.

Chapter 4 details the collaboration between BAE Systems and our group that explored the feasibility of current LiS technology for electric flight. Our group's contribution was electrochemical characterization of the LiS proprietary pre-commercial pouch cells to be used for parameter estimation and informing our modeling work. Cycling and flight protocol experiments were performed, and parameter estimation was performed with the ensuing data. The characterization of the data highlighted the gap between the current LiS technology and the requirements for electric flight, and recommendations for further research from an industry perspective is included. The conclusion of this work was the development of the Tanks-in-Series model. The Tank model was developed for its speed and accuracy, and the parameters derived from optimization are the ones reported in Chapter 2. The baseline parameters were also used for the coupled electrochemical-thermal model in Chapter 5. The design parameters in Chapter 3 were calculated from a high-energy cell while the other parameters are the

baseline from the pouch cell estimation.

The development of a coupled electrochemical-thermal model can be found in Chapter 5. This work utilizes the 1D model and augments it with a simple thermal model. The impact of the cell parameters on the heat generation is explored as well as recommendations for thermal characterization and further parameter studies.

This thesis culminates in the ongoing collaboration with Pacific Northwest National Laboratory and Brookhaven National Laboratory detailed in Chapter 6. This work combines the efficient Tank model with speciation work to estimate parameters from given coin cell data. The successful collaboration resulted from a sustained effort to focus modeling work in experimentally-relevant directions as well as directed and accessible communication within the Battery500 community. An auxiliary component uses data science methods to analyze the X-ray diffraction (XRD) data from BNL. With the use of an unsupervised machine learning method, peak shifts in the spectra data have been statistically linked to populations separated by particle size, charge/discharge, and voltage/SOC ranges.

Note about model formulation: Chapters 2-5 use a hybrid model formulation between the Kumaresan/reference state and Newman-type formulation where a reference state is considered, but the overpotential is not truly zero at equilibrium. For LiS batteries, where many parameters are difficult to isolate and experimental measurements are lacking, formulating the model and parameter values based on an assumed but unmeasured reference state is somewhat confusing and unnecessary. To maintain thermodynamic consistency, the work in Chapter 6 uses a Newman-type formulation of the Butler-Volmer and Nernst equations without a reference state. More

detailed information can be found in Model Development of Chapter 6.

Chapter 2

An Efficient Electrochemical Tanks-in-Series Model for Lithium Sulfur Batteries

Note: this chapter was originally published as an article.

C. Parke, A. Subramaniam, S. Kolluri, D. Schwartz, V. Subramanian, An Efficient Electrochemical Tanks-in-Series Model for Lithium Sulfur Batteries, *J. Electrochm. Soc.* **167**, 163503 (2020). https://doi.org/10.1149/1945-7111/abcc30

2.1 Abstract

This article applies and efficiently implements the Tanks-in-Series methodology (*J. Electrochem. Soc.*, **167**, 013534 (2020)) to generate a computationally efficient electrochemical model for Lithium-Sulfur batteries. The original Tank model approach for Lithium-ion batteries is modified to account for porosity changes with time. In addition, an exponential scaling method is introduced that enables efficient simulation of the model equations to address the wide range of time constants present for different reactions in the Lithium-Sulfur system. The Tank Model achieves acceptable voltage error even for transport-limited discharged conditions. Predictions of internal electrochemical variables are examined, and electrochemical implications of the approximations discussed. This suggests significant potential for real-time applications such as optimal charging, cell-balancing, and estimation, and represents a step forward in efforts to incorporate detailed electrochemical models in advanced Battery Management Systems for Lithium-Sulfur batteries.

2.2 Introduction

Research on Lithium-Sulfur batteries has increased dramatically in recent years due to the high theoretical energy density of 2500 Wh/kg[16]. Despite their promise, Lithium-Sulfur batteries suffer from several challenges that are unique to this chemistry that contribute to low cycle life and poor stability. Soluble polysulfides travel to the anode to react and form lower-order polysulfides that move back to the cathode through the shuttle mechanism, which contributes to reversible and irreversible loss of active material and self-discharge[17,18]. The highly reactive lithium metal anode consumes electrolyte via parasitic side reactions and forms dendrites and dead lithium clusters, resulting in capacity loss, increased cell resistance, and safety concerns[19-22]. With cycling, a passivation layer forms within the cathode due to the insoluble and insulating solid sulfur precipitates which affects sulfur utilization, cathode structural integrity, and overall capacity retention[23-25]. Due to these issues, the power capabilities of lithium sulfur batteries are limited.

Mathematical modeling can help accelerate commercialization of Li-S batteries by elucidating the underlying mechanisms and enabling exploration of the design space without the time and cost of experiments. Electrochemical physics-based models offer insight into the internal states of the battery, such as local overpotentials and concentrations throughout a cell. These quantities are seldom accessible experimentally, indicating the value of rigorous electrochemical models. The first effort in this direction was a zero-dimensional lumped model published in 2004 by Mikhaylik and Akridge[3], which included simple kinetics and thermodynamics. In 2008, Kumaresan et al.[4]

introduced a one-dimensional (1D) mathematical model for the discharge of Li-S batteries. This model included transport effects, a more realistic set of sulfur reduction chemistries, and morphological changes in the cathode. A related model was developed by Neidhardt et al.[5] in 2012. A series of papers were published with a similar 1D model that explored impedance[6], charging[7], and degradation[8-10], as well as lumped models with simplified reaction mechanisms, reduced number of parameters[11-13], and precipitation of lithium sulfide[14,15].

For all models, there exists an inherent tradeoff with computational efficiency, ease of parameterization, and model complexity. Within the literature on lithium sulfur models, the 1D models are more descriptive and can capture experimentally-observed voltage characteristics reasonably well, such as the relative length and potential of the typical two-plateau discharge curve and the voltage dip and recovery between the two plateaus. Simplified models have been developed specifically for increased computational efficiency and ease of parameterization, and they have been used to predict general trends of the second voltage plateau rather than the overall shape of voltage curves[12,13,26,27]. Although these simplified models have reduced computation times relative to 1D models, the utility of using physics-based models is the insight provided into the internal states that contribute to cell performance, and the direct linkage to the geometric, chemical, and physical properties of the electrodes, electrolyte, and separator. Furthermore, Li-S system dynamics, including reaction mechanisms, are sensitive to the electrolyte[28], which highlights the importance of parameter estimation to improve individual system predictions. Leveraging the prediction power of the 1D models for parameter estimation can enable better agreement between models and experiments.

Another application of physics-based models is design space exploration and optimization. Optimization of parameters can mean hundreds to thousands of model calls (in sequential optimization framework which is the most commonly used approach in the optimization community), which quickly can become computationally intractable[29]. Fast and robust models that maintain high predictive capabilities can accelerate research by allowing greater exploration of design space and optimization with efficiency. Both parameter estimation and exploration of design space underpin the importance of efficient yet descriptive models.

This work focuses on developing an efficient physics-based model that maintains similar predictive capabilities to 1D models under a wide range of conditions while also ensuring computational efficiency. The model presented herein applies the Tank-in-Series methodology[30] to the Li-S electrochemical model based on the work by Kumaresan et al[4]. No additional physics or mechanisms have been included, thereby allowing this work to focus on further development of the volume-averaging method. With this flexible framework, more physics and chemistry can be added as needed while maintaining model efficiency.

2.3 Mathematical and Experimental Methods

The following reactions describe the discharge of a lithium sulfur battery.

$$Li_{(s)} \rightleftharpoons Li^{+} + e^{-} \tag{2.1}$$

$$\frac{1}{2} S_{8(l)} + e^{-} \rightleftharpoons \frac{1}{2} S_8^{2-} \tag{2.2}$$

$$\frac{3}{2} S_8^{2-} + e^{-} \rightleftharpoons 2 S_6^{2-} \tag{2.3}$$

$$S_6^{2-} + e^{-} \rightleftharpoons \frac{3}{2} S_4^{2-} \tag{2.4}$$

$$\frac{1}{2} S_4^{2-} + e^{-} \rightleftharpoons S_2^{2-} \tag{2.5}$$

$$\frac{1}{2} S_2^{2-} + e^{-} \rightleftharpoons S^{2-} \tag{2.6}$$

$$S_{8(s)} \rightleftharpoons S_{8(l)} \tag{2.7}$$

$$2Li^{+} + S^{2-} \rightleftharpoons Li_2S_{(s)} \tag{2.8}$$

Reaction (2.1) describes the oxidation of the lithium foil anode. Reactions (2.1-6) refer to the electrochemical reduction of liquid S_8 in the cathode. Reactions (2.7) and (2.8) are the dissolution and precipitation of the two solid species, $S_{8(s)}$ and $Li_2S_{(s)}$. The work assumes the same reaction mechanism as the Kumaresan model[4]. However, Li_2S is the only solid product considered as the presence of other precipitates is still debated[10,11,31].

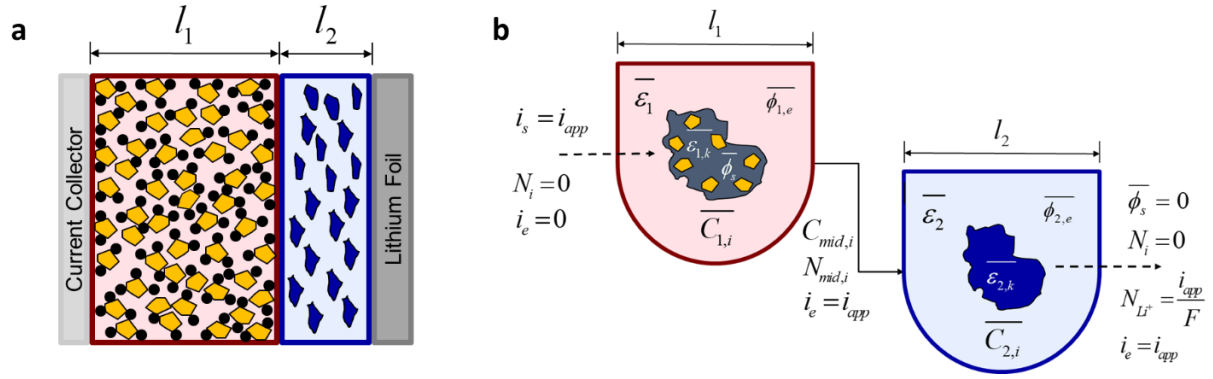

Figure 2.1 **(a)** Physical representation of the lithium sulfur battery, left to right: aluminum current collector, cathode with thickness of l_1 filled with yellow S_8(s) particles and conductive carbon additives with electrolyte, porous separator in blue with thickness of l_2, and the lithium foil anode, **(b)** Schematic of the Tank-in-Series model that volume averages the cathode and separator of corresponding thicknesses of l_1 and l_2, resulting in average variables in each tank. Mass flow between the tanks is connected through interfacial fluxes. The sign convention is such that the applied current is negative for discharge.

Figure 2.1 (a) is the physical representation of lithium sulfur batteries. Because the focus of this work is primarily the sulfur cathode dynamics, the lithium anode has been included as a constant source of lithium ions without furthering considering side reactions or limitations.

Table 2.1.1-D Lithium Sulfur Mathematical Discharge Model.

Governing Equations	**Boundary Conditions**
Positive Electrode (Region 1)	
$\frac{\partial \varepsilon_1 C_{1,i}}{\partial t} = -\frac{\partial N_{1,i}}{\partial x} + r_i - R_{1,i}$	$C_{1,i}\Big\|_{x=l_1} = C_{2,i}\Big\|_{x=l_1}$
$N_{1,i} = -D_{1,i}\frac{\partial C_{1,i}}{\partial x} - z_i \frac{D_{1,i}}{RT} F C_{1,i} \frac{\partial \phi_{1,e}}{\partial x}$	$N_{1,i}\Big\|_{x=0} = 0$
$i_s = -\sigma \frac{\partial \phi_s}{\partial x}$	$-\sigma \frac{\partial \phi_s}{\partial x}\Big\|_{x=0} = i_{app}$
$i_{1,e} = F\sum_i z_i N_{1,i}$	$i_{1,e}\Big\|_{x=0} = 0$
$\frac{\partial \varepsilon_{1,k}}{\partial t} = \tilde{V}_k R'_k$	$N_{1,i}\Big\|_{x=l_1} = N_{2,i}\Big\|_{x=l_1}$
$\frac{\partial \varepsilon_1}{\partial t} = -\sum_k \tilde{V}_k R'_k$	$-\sigma \frac{\partial \phi_s}{\partial x}\Big\|_{x=l_1} = 0$

Separator (Region 2)

$$\frac{\partial \varepsilon_2 C_{2,i}}{\partial t} = -\frac{\partial N_{2,i}}{\partial x} - R_{2,i}$$

$$N_{2,i} = -D_{2,i}\frac{\partial C_{2,i}}{\partial x} - z_i \frac{D_{2,i}}{RT} F C_{2,i} \frac{\partial \phi_{2,e}}{\partial x}$$

$$i_{2,e} = F\sum_i z_i N_{2,i}$$

$$\frac{\partial \varepsilon_{2,k}}{\partial t} = \tilde{V}_k R'_k$$

$$\frac{\partial \varepsilon_2}{\partial t} = -\sum_k \tilde{V}_k R'_k$$

$$N_{2,i}\Big|_{x=l_1+l_2} = 0$$

$$N_{2,Li^+}\Big|_{x=l_1+l_2} = \frac{i_{app}}{F}$$

$$i_{1,e}\Big|_{x=l_1} = i_{2,e}\Big|_{x=l_1}$$

$$\phi_s\Big|_{x=l_1+l_2} = 0$$

$$i_{2,e}\Big|_{x=l_1+l_2} = FN_{2,Li^+}$$

Other Expressions

$$r_i = -a\sum_j \frac{s_{i,j} i_j}{n_j F}$$

$$\frac{\partial i_s}{\partial x} + \frac{\partial i_e}{\partial x} = 0$$

$$\eta_j = \phi_s - \phi_e - U_{j,ref}$$

$$R_i = \sum_k \gamma_{i,k} R'_k$$

$$i_j = i_{o,j_{ref}} \left\{ \left(\frac{C_{i,anodic}}{C_{i,ref}} \right)^{s_{a,j}} \exp\left(\frac{\alpha_{a,j} F}{RT} \eta_j \right) - \left(\frac{C_{i,cathodic}}{C_{i,ref}} \right)^{-s_{c,j}} \exp\left(-\frac{\alpha_{c,j} F}{RT} \eta_j \right) \right\}$$

$$a = a_0 \left(\frac{\varepsilon}{\varepsilon_{initial}} \right)^{\xi}$$

$$\frac{\partial i_e}{\partial x} = a\sum_j i_j$$

$$U_{j,ref} = U_j^{\theta} - \frac{RT}{n_j F}\sum_i s_{ij} \ln\left[\frac{C_i}{1000} \right]$$

$$R'_k = k_k \varepsilon_{1,k} \left(\prod_i C_{1,i}^{\gamma_{i,k}} - K_{sp,k} \right)$$

The governing equations, shown in Table 2.1, are taken from the 1D mathematical model by Kumaresan et al[4]. The model assumes dilute solution theory that does not consider the effect of species' interactions on diffusion. Each part of the voltage curve can be attributed to the physical phenomena that is happening during discharge, which physics-based models capture. The model includes transport by migration and diffusion, Butler-Volmer kinetics, thermodynamics described by Nernst equations, and morphology changes in the cathode. The porosity and volume fractions of solid sulfur and lithium sulfide change with time, and the available volume of the cathode then

Table 2.2. Parameters for the Ionic Species.

Species (i)	z_i	D_{i0} (m^2/s)	$C_{i,ref}$ (mol/m^3)
Li^+	+1	1 x 10^{-10} [c]	1033 [a]
$S_{8(l)}$	0	1 x 10^{-10} [c]	19.9 [a]
S_8^{2-}	-2	1 x 10^{-10} [c]	0.16 [a]
S_6^{2-}	-2	1 x 10^{-10} [c]	0.31 [a]
S_4^{2-}	-2	1 x 10^{-10} [c]	0.020 [b]
S_2^{2-}	-2	1 x 10^{-10} [c]	0.56 x 10^{-6} [a]
S^{2-}	-2	1 x 10^{-10} [c]	0.78 x 10^{-9} [a]
A^-	-1	1 x 10^{-9} [a,30]	1032 [a]

Table 2.3. Cathode and Separator Parameters

Parameter	Cathode	Separator
Thickness (μm)	40 [a]	21 [b]
a_0 (m^2/m^3) [a]	143292	-
$\varepsilon_{initial}$ [a]	0.54	0.6
$\varepsilon_{S_{8(s)},initial}$	0.24 [c]	1 x 10^{-12} [b]
$\varepsilon_{Li_2S_{(s)},initial}$ [b]	1 x 10^{-7}	1 x 10^{-7}
σ [a]	937	-
ξ [b]	1.5	-
T (K) [b]	293	293
b [b]	2.5	2.5

[a] estimated parameters, [b] taken from Kumaresan, [c] design parameters

Table 2.4. Properties of the Electrochemical Reactions

Reaction (j)	$i_{0,jref}$ (A/m^2) [c]	U_j^θ (V) [a]	$s_{a,j}$	$s_{c,j}$	$\alpha_{a,j}$ [b]	$\alpha_{c,j}$ [b]
2	1.972	2.50	-1/2	1/2	1/2	1/2
3	0.019	2.49	-3/2	2	1/2	1/2
4	0.019	2.42	-1	3/2	1/2	1/2
5	1.97 x 10^{-4}	2.12	-1/2	1	1/2	1/2
6	1.97 x 10^{-7}	2.00	-1/2	1	1/2	1/2

directly affects the diffusion of the ionic species. Both electrochemical and chemical reactions are present in the model as there are both reduction reactions involving sulfur species and non-charge transfer dissolution and precipitation reactions. The parameters used in this work are included in Tables 2.2-.5, which have been modified from the base parameters in the Kumaresan model[4]. Where indicated, the parameters reflect the best fit from parameter estimation to experimental data from a C/5 discharge curve. The effect of the diffusion constants, the cathode thickness, and the exchange current densities in particular is considered in the Discussion, and the parameter values listed here represent the baseline.

Table 2.5. Parameters for the Precipitation Reactions.

Precipitate (k)	Rate Constant (k_k)	Solubility Product (K_k) [a]	Molar Volume (V_k) (m^3/mol)[b]
$S_{8(s)}$	1.0 s^{-1} [b]	20. mol m^{-3}	1.239 x 10^{-4}
$Li_2S_{(s)}$	27. m^6 mol^2 s^{-1} [a]	2.8 x 10^{-5} mol^3 m^{-9}	2.768 x 10^{-5}

2.4 Model Development

In this section, we propose and discuss the development of the mass-conserving volume-averaged Tank-in-Series model for lithium sulfur batteries, summarized in Table 2.6. In the Tank model, each region is approximated as a tank connected in series. Previously, our group has developed and validated this approach for Lithium-ion batteries[30], and one of the key differences and challenges is the dynamic porosity within lithium sulfur batteries. The equations are spatially integrated over the two regions, the cathode and the separator. The anode is modeled as a constant flux boundary condition for lithium ions. The result is average variables in each region, and the midpoint approximation is used to calculate interfacial fluxes and species between the cathode and separator. The cathode and separator are treated as separate tanks as depicted in Figure 2.1 (b), and the equations for each variable is volume averaged over that region. Through the use of the flux boundary conditions, the mass flow between the tanks is coupled. The sign convention employed results in a negative applied current during discharge.

To illustrate volume averaging, the sulfide ion, S^{2-}, the final ionic species in the reduction scheme, is considered. The governing equations for the cathode, Equation (2.9), is written for S^{2-}. In the cathode, the governing equation for the sulfide ions is

$$\frac{\partial \varepsilon_1 C_{1,S}}{\partial t} = -\frac{\partial N_{1,S}}{\partial x} + r_S - R_{1,S} \qquad 0 < x < l_1 \quad (2.9)$$

where ε_1 denotes the porosity in region 1 or the cathode, $C_{1,S}$ is the concentration of S^{2-} in the cathode, r_s is the rate of the production of all of the electrochemical reactions involving S^{2-}, $R_{1,S}$ is the rate of consumption of the precipitation reaction in the cathode

for S^{2-}. For subscripts on variables, 1 denotes a variable in the cathode or region 1, and 2 is the separator or region 2. The subscript S denotes the S^{2-} species. $N_{1,S}$ represents the flux in the cathode, which considers both diffusion and migration, defined as

$$N_{1,S} = -D_{1,S}\frac{\partial C_{1,S}}{\partial x} - z_S \frac{D_{1,S}}{RT} F C_{1,S} \frac{\partial \phi_{1,e}}{\partial x} \tag{2.10}$$

where $D_{1,S}$ is the effective diffusion coefficient corrected by the Bruggeman expression where $D_{1,i} = D_{i,0}\varepsilon_1^b$, D_{io} is the intrinsic diffusion coefficient and b is the Bruggeman coefficient, z_S is the charge number of S^{2-}, $\phi_{1,e}$ is the electrolyte-phase potential in the cathode.

Similarly, the overall species balance for the separator is

$$\frac{\partial \varepsilon_2 C_{2,S}}{\partial t} = -\frac{\partial N_{2,S}}{\partial x} - R_{2,S} \qquad l_1 < x < l_1 + l_2 \tag{2.11}$$

Where $N_{2,S}$ is defined as

$$N_{2,S} = -D_S \frac{\partial C_{2,S}}{\partial x} - z_S \frac{D_S}{RT} F C_{2,S} \frac{\partial \phi_{2,e}}{\partial x} \tag{2.12}$$

The flux boundary conditions for sulfide ions are

$$N_{0/1,S} = 0 \qquad x = 0 \tag{2.13}$$

$$N_{2/3,S} = 0 \qquad x = l_1 + l_2 \tag{2.14}$$

Where 0/1 indicates the interface of the cathode and the current collector and 2/3 indicates the interface between the separator and the lithium foil anode. Between the cathode and separator, continuity of fluxes is maintained. The governing equations are then volume averaged by integrating over the volume of each region. For illustration, the governing equation for S^{2-} is integrated over the volume, V_1, in Equation (2.15).

$$\frac{d\int_{V_1}\varepsilon_1 C_{1,S}dV}{dt} = -\int_{V_1}\frac{\partial N_{1,S}}{\partial x}dV + \int_{V_1} r_S dV - \int_{V_1} R_{1,S}dV \tag{2.15}$$

In the one-dimensional model, the volume integral is over the differential volume dV, which is considered to be $dV = Adx$, where A is a constant cross-sectional area. For each average quantity, the integral is expressed as $\bar{y} = \frac{\int_V ydV}{\int_V dV}$, with $\bar{y}$ denoting the volume average of variable y in the given region or 'tank'. We also make the assumption that the product of the averages is equal to the average of the products, i.e. $\frac{\int_{V_1}\varepsilon_1 C_{1,i}dV}{\int_{V_1}dV} = \overline{\varepsilon_1 C_{1,i}} \approx \overline{\varepsilon_1}\,\overline{C_{1,i}}$. For terms like r_i, the approximation is made that the volume averaged term is simply evaluated with the average variables of that function, $\frac{\int_{V_1} r_i dV}{\int_{V_1}dV} = \bar{r_i} = \overline{f\left(C_i,\phi_1,\phi_2\right)} \approx f\left(\overline{C_i},\overline{\phi_1},\overline{\phi_2}\right)$. Substituting these relations back into the governing equation gives a one-dimensional integral over the length of the cathode

$$\frac{d(\overline{\varepsilon_1}\,\overline{C_{1,S}})}{dt} = -\frac{\int_{x=0}^{x=l_1}\frac{\partial N_{1,S}}{\partial x}dx}{l_1} + \overline{r_S} - \overline{R_{1,S}} = \frac{N_{1,S,x=0} - N_{1,S,x=l_1}}{l_1} + \overline{r_S} - \overline{R_{1,S}} \tag{2.16}$$

Substituting $N_{1,S,x=0} = 0$ into the previous equation, results in

$$\frac{d(\overline{\varepsilon_1}\,\overline{C_{1,S}})}{dt} = \frac{-N_{1,S,x=l_1}}{l_1} + \overline{r_S} - \overline{R_{1,S}} \tag{2.17}$$

The same can be done for the separator to arrive at the following with the substitution $N_{2,S,x=l_1+l_2} = 0$

$$\frac{d(\overline{\varepsilon_2}\,\overline{C_{2,S}})}{dt} = \frac{N_{2,S,x=l_1}}{l_2} - \overline{R_{2,S}} \tag{2.18}$$

Next, let us consider how to approximate the flux at the interface of the cathode and the separator. Through the use of the flux boundary conditions, the mass flow between the tanks can be coupled. For the approximation, a 'driving force' ΔC_m and a 'length scale' δ_m is defined for interface between the separator and cathode, where subscript m denotes 1 for cathode or 2 for separator. The 'driving force' ΔC_m is the difference between the average concentration of the region and the unknown concentration at the interface $\Delta C_m = \overline{C_m} - C_{x=interface}$. The 'length scale' is δ_m, defined by $\delta_m = delta \cdot l_m$, where *delta* is the dimensionless fraction where concentration gradients are assumed to be, and l_m is the thickness of the domain. The same *delta* value is used in the separator and the cathode. Note, the variable *delta* will be discussed throughout the Results and Discussion to consider the effect the length scale approximation has on the Tank model predictions.

Similarly, a 'driving force' $\Delta\phi_{m,e}$ can be defined for the liquid potential that is approximated as $\Delta\phi_{m,e} = \overline{\phi_{m,e}} - \phi_{m,e,x=interface}$. For each concentration, the interfacial boundary conditions from each region can be equated to determine the unknown value at the interface. This assumption is equivalent to performing Gauss collocation with one collocation point at the midpoint of the region. For these approximations, the error scales with the square of the domain thickness. The resulting flux equation becomes

$$N_{1,S,x=l_1} = -\overline{D_{1,S}}\left.\frac{\partial C_{1,S}}{\partial x}\right|_{x=l_1} - z_S\frac{\overline{D_{1,S}}}{RT}FC_{1,S,x=l_1}\left.\frac{\partial \phi_{1,e}}{\partial x}\right|_{x=l_1} \cong +\overline{D_{1,S}}\frac{\Delta C_1}{\delta_1} + z_S\frac{\overline{D_{1,S}}}{RT}FC_{1,S,x=l_1}\frac{\Delta \phi_{1,e}}{\delta_1}$$
$$= +\overline{D_{1,S}}\left(\frac{\overline{C_{1,S}} - C_{1,S,x=l_1}}{\delta_1}\right) + z_S\frac{\overline{D_{1,S}}}{RT}FC_{1,S,x=l_1}\left(\frac{\overline{\phi_{1,e}} - \phi_{1,e,x=l_1}}{\delta_1}\right) \quad (2.19)$$

For terms in the flux equation without spatial derivatives, the values are taken to be the average in the region; the diffusivity is evaluated at the average porosity, where $\overline{D_{1,S}} = D_{i=S,0}\overline{\varepsilon_1}$.

A similar expression can be written for the interfacial flux from the separator.

$$N_{2,S,x=l_1} = -\overline{D_{2,S}}\left.\frac{\partial C_{2,S}}{\partial x}\right|_{x=l_1} - z_S\frac{\overline{D_{2,S}}}{RT}FC_{2,S,x=l_1}\left.\frac{\partial \phi_{2,e}}{\partial x}\right|_{x=l_1} \cong -\overline{D_{2,S}}\frac{\Delta C_2}{\delta_2} - z_S\frac{\overline{D_{2,S}}}{RT}FC_{2,S,x=l_1}\frac{\Delta \phi_{2,e}}{\delta_2}$$
$$= -\overline{D_{2,S}}\left(\frac{\overline{C_{2,S}} - C_{2,S,x=l_1}}{\delta_2}\right) - z_S\frac{\overline{D_{2,S}}}{RT}F\overline{C_{2,S}}\left(\frac{\overline{\phi_{2,e}} - \phi_{2,e,x=l_1}}{\delta_2}\right) \quad (2.20)$$

The electroneutrality expression is given by

$$\sum_i z_i C_i = 0 \quad (2.21)$$

Electroneutrality provides the equation for the potential. Using this expression to eliminate one of the concentration variables and substituting back into the boundary conditions at the interface $N_{1,i,x=l_1} = N_{2,i,x=l_1}$, the boundary conditions simplify to

$$\varepsilon_1^{b_1}\left.\frac{\partial \phi_{1,e}}{\partial x}\right|_{x=l_1} = \varepsilon_2^{b_2}\left.\frac{\partial \phi_{2,e}}{\partial x}\right|_{x=l_1} \quad (2.22)$$

This can be approximated as

$$\varepsilon_1^{b_1}\left.\frac{\Delta \phi_{1,e}}{\delta_1}\right|_{x=l_1} = \varepsilon_2^{b_2}\left.\frac{\Delta \phi_{2,e}}{\delta_2}\right|_{x=l_1} \quad (2.23)$$

Which can be further approximated as

$$(\overline{\varepsilon_1})^{b_1}\left(\frac{\phi_{1,e,x=l_1}-\overline{\phi_{1,e}}}{\delta_1}\right)=(\overline{\varepsilon_2})^{b_2}\left(\frac{\overline{\phi_{2,e}}-\phi_{2,e,x=l_1}}{\delta_2}\right) \tag{2.24}$$

Next, we can use the interfacial boundary condition of continuity where $\phi_{1,e,x=l_1}=\phi_{2,e,x=l_1}=\phi_{e,mid}$ to simplify Equation (2.24).

$$\phi_{e,mid}=\frac{\left(\overline{\varepsilon_1}\right)^{b_1}\delta_2\overline{\phi_{1,e}}+\left(\overline{\varepsilon_2}\right)^{b_2}\delta_1\overline{\phi_{2,e}}}{\left(\overline{\varepsilon_1}\right)^{b_1}\delta_2+\left(\overline{\varepsilon_2}\right)^{b_2}\delta_1} \tag{2.25}$$

Similarly, for concentration, simplification of the flux conditions at the interface results in

$$\varepsilon_1^{b_1}\frac{\partial C_{1,i}}{\partial x}_{x=l_1}=\varepsilon_2^{b_2}\frac{\partial C_{2,i}}{\partial x}_{x=l_1} \tag{2.26}$$

Where after substituting the 'driving force' and 'diffusion length' expression becomes

$$C_{mid,S}=\frac{\delta_2\left(\overline{\varepsilon_1}\right)^{b_1}\overline{C_{1,S}}+\delta_1\left(\overline{\varepsilon_2}\right)^{b_2}\overline{C_{2,S}}}{\left(\overline{\varepsilon_1}\right)^{b_1}\delta_2+\left(\overline{\varepsilon_2}\right)^{b_2}\delta_1} \tag{2.27}$$

Now that we have defined the interfacial quantities for concentration and liquid-phase potential, the flux at the interface $N_{mid,S}$ can be determined.

$$N_{mid,S}=D_{S0}\frac{\left(\overline{\varepsilon_1}\right)^{b_1}\left(\overline{\varepsilon_2}\right)^{b_2}}{\left(\overline{\varepsilon_1}\right)^{b_1}\delta_2+\left(\overline{\varepsilon_2}\right)^{b_2}\delta_1}\left[\left(\overline{C_{1,S}}-\overline{C_{2,S}}\right)+\frac{z_S}{RT}FC_{mid,s}\left(\overline{\phi_{1,e}}-\overline{\phi_{2,e}}\right)\right] \tag{2.28}$$

Let us now consider the potential equations, and in this case, the current equations are used instead of explicit potential equations. Let us consider the equation for conservation of charge.

$$\frac{\partial i_s}{\partial x}+\frac{\partial i_e}{\partial x}=0 \tag{2.29}$$

Where i_s is the current within the solid phase and i_e is current in the liquid phase.

After substituting in $\frac{\partial i_e}{\partial x} = a\sum_j i_j$ for the liquid phase current term, we arrive at the following

$$\frac{\partial i_s}{\partial x} + a\sum_j i_j = 0 \tag{2.30}$$

Where a is the specific surface area of the cathode.

Through volume averaging and substituting the boundary conditions for the solid phase current, the following expression can be determined

Table 2.6. Equations for the Tanks-in-Series Model for Lithium Sulfur Batteries.

Cathode (Region 1)	**Separator (Region 2**
$\frac{d(\overline{\varepsilon_1}\overline{C_{1,i}})}{dt} = \frac{-N_{mid,i}}{l_1} + \overline{r_i} - \overline{R_{1,i}}$	$\frac{d(\overline{\varepsilon_2}\overline{C_{2,i}})}{dt} = \frac{N_{mid,i} - N_{2,i=Li^+,x=l_1+l_2}}{l_2} - \overline{R_{2,i}}$
$\sum_i z_i \frac{d(\overline{\varepsilon_1}\overline{C_{1,i}})}{dt} = 0$	$N_{2,i=Li^+,x=l_1+l_2} = \frac{i_{app}}{F}$
$\frac{i_{app}}{l_1} = a\sum_j \overline{i_j}$	$\sum_i z_i \frac{d(\overline{\varepsilon_2}\overline{C_{2,i}})}{dt} = 0$
$\frac{d\overline{\varepsilon_{1,k}}}{dt} = \tilde{V}_k R'_k$	$\frac{d\overline{\varepsilon_{2,k}}}{dt} = \tilde{V}_k R'_k$
$\frac{d\overline{\varepsilon_1}}{dt} = -\sum_k \tilde{V}_k R'_k$	$\frac{d\overline{\varepsilon_2}}{dt} = -\sum_k \tilde{V}_k R'_k$
Interfacial Expressions	
$\phi_{e,mid} = \frac{\left(\overline{\varepsilon_1}\right)^{b_1}\delta_2\overline{\phi_{1,e}} + \left(\overline{\varepsilon_2}\right)^{b_2}\delta_1\overline{\phi_{2,e}}}{\left(\overline{\varepsilon_1}\right)^{b_1}\delta_2 + \left(\overline{\varepsilon_2}\right)^{b_2}\delta_1}$	$C_{mid,i} = \frac{\delta_2\left(\overline{\varepsilon_1}\right)^{b_1}\overline{C_{1,i}} + \delta_1\left(\overline{\varepsilon_2}\right)^{b_2}\overline{C_{2,i}}}{\left(\overline{\varepsilon_1}\right)^{b_1}\delta_2 + \left(\overline{\varepsilon_2}\right)^{b_2}\delta_1}$
$N_{mid,i} = D_{i0}\frac{\left(\overline{\varepsilon_1}\right)^{b_1}\left(\overline{\varepsilon_2}\right)^{b_2}}{\left(\overline{\varepsilon_1}\right)^{b_1}\delta_2 + \left(\overline{\varepsilon_2}\right)^{b_2}\delta_1}\left[\left(\overline{C_{1,i}} - \overline{C_{2,i}}\right) + \frac{z_i}{RT}FC_{mid,i}\left(\overline{\phi_{1,e}} - \overline{\phi_{2,e}}\right)\right]$	

Other Expressions

$$\bar{r}_i = -\bar{a}\sum_j \frac{s_{i,j}\bar{i}_j}{n_j F} \qquad \overline{U_{j,ref}} = U_j^{\theta} - \frac{RT}{n_j F}\sum_i s_{ij} \ln\left[\frac{\bar{C}_i}{1000}\right]$$

$$\bar{a} = a_0\left(\frac{\bar{\varepsilon}}{\varepsilon_{initial}}\right)^{\xi} \qquad \bar{R}_i = \sum_k \gamma_{i,k}\bar{R}'_k$$

$$\overline{\eta_j} = \bar{\phi}_s - \bar{\phi}_e - \overline{U_{j,ref}} \qquad \bar{R}'_k = k_k \bar{\varepsilon}_k\left(\prod_i \overline{C_i^{\gamma_{i,k}}} - K_{sp,k}\right)$$

$$\bar{i}_j = i_{o,j_{ref}}\left\{\left(\frac{e^{C_{i,anodic}}}{e^{C_{i,ref}}}\right)^{s_{i,j}} \exp\left(\frac{\alpha_{a,j}F}{RT}\bar{\eta}_j\right) - \left(\frac{e^{C_{i,cathodic}}}{e^{C_{i,ref}}}\right)^{-s_{i,j}} \exp\left(-\frac{\alpha_{c,j}F}{RT}\bar{\eta}_j\right)\right\}$$

$$-\frac{i_{s,x=l_1} - i_{s,x=0}}{l_1} = -\frac{0 - i_{app}}{l_1} = \frac{i_{app}}{l_1} = \overline{a\sum_j i_j} = \bar{a}\sum_j \bar{i}_j \tag{2.31}$$

In simplifying Equation (2.32), we have made the standard Tank Model approximation $\overline{a\sum_j i_j} \approx \bar{a}\sum_j \bar{i}_j$.

For the liquid phase potential, we start with the electroneutrality expression, Equation 2.21, and multiply by the porosity, ε. After averaging, we take the derivative with respect to time to arrive at the following

$$\sum_i z_i \frac{d(\overline{\varepsilon_m}\,\overline{C_{m,i}})}{dt} = 0 \tag{2.32}$$

Then, substitute the mass balance expression for the term $\frac{d(\overline{\varepsilon_m}\,\overline{C_{m,i}})}{dt}$ for the liquid phase potential equation. This results in the system of nonlinear differential algebraic equations (DAE) shown in Table 2.6.

Typically DAE models are written in the form $dy/dt = f(y,z)$, $0 = g(y,z)$, where y is the variable mapped to the differential equations and z is the variable mapped to the

algebraic equations. This system can be solved using any DAE solver in time such as IDA in C, DASKR in FORTRAN, ode15s or ode15i in MATLAB, etc. However, likely because of varying dynamics in the system and the multiscale nature of different time constants and reactions, most adaptive solvers cannot simulate beyond 2.0 V during discharge. For example, a past MATLAB code (simple scheme listed elsewhere[24]) fails when the solver reaches 1.9 V. In this paper, we propose an effective scaling methodology to scale multiple variables. The equation for concentration is of the form is $dC/dt = aC + f(C)$, and we define log scaling as $\hat{z} = \ln(z)$. The scaled variables are species concentrations, volume fractions, and porosities while the potentials are not scaled. With the combined time scaling and the averaging of the spatial variables, the Tank model consistently reaches the voltage cutoff whereas a singularity occurs in the 1D model at the end of discharge for most conditions. This scaling helps the original 1D model as well. The singularity in the 1D model is due to the extreme gradients that arise at the end of discharge when concentration variables rapidly approach zero at some points within the cathode. The Tank model through the volume averaging maintains much higher values for concentrations with comparatively quasi-steady-state values and is therefore more numerically stable. The singularity in the 1D model occurs most often with rates less than 1C and low cutoff voltages of 1.9 V and below.

To illustrate the time scaling, let us consider the mass balance of the S^{2-} species again. For the concentrations, porosities, and volume fractions, the exponential of the logarithmic variable is taken and substituted back into the equation, $z = e^{\hat{z}}$, resulting in

$$\frac{d(e^{\varepsilon_1}e^{C_{1,S}})}{dt} = e^{C_{1,S}}e^{\varepsilon_1}\frac{d(\varepsilon_1)}{dt} + e^{\varepsilon_1}e^{C_{1,S}}\frac{d(C_{1,S})}{dt} = \frac{-N_{1,S,x=l_1}}{l_1} + \overline{r_S} - \overline{R_{1,S}} \tag{2.33}$$

which simplifies to

$$\frac{d(\varepsilon_1)}{dt}+\frac{d(C_{1,S})}{dt}=\frac{1}{e^{C_{1,S}}e^{\varepsilon_1}}\left(\frac{-N_{1,S,x=l_1}}{l_1}+\overline{r_S}-\overline{R_{1,S}}\right) \tag{2.34}$$

The flux is now

$$N_{1,S,x=l_1}=-D_{1,S}\left(\frac{e^{C_{1,S}}-C_{mid,S}}{\delta_1}\right)-z_S\frac{D_{1,S}}{RT}Fe^{C_{1,S}}\left(\frac{\overline{\phi_{1,e}}-\phi_{e,mid}}{\delta_1}\right) \tag{2.35}$$

Notice that the potential variables have not been substituted because they are algebraic variables instead of differential variables, and their range is on the order of unity and does not change over orders of magnitude. The substitution can be done for the rest of the equations to arrive at the set equations found in Tables 2.7.

The resulting system of equations was written in *Maple 2018* and solved with its stiff solver based on semi-implicit Runge Kutta solver called through the *dsolve* command in implicit mode. A robust initialization strategy was used to find consistent initial conditions[30]. The same set of equations were also solved in IDA which enables order of magnitude faster computation compared to *Maple*. The computational speeds were calculated on an Intel (R) Xeon (R) E-2176M processor with a clock speed of 2.70 GHz and 64 GB RAM.

Experimental data is from the first discharge cycle of a proprietary, pre-commercial 19.5 Ah Li-S pouch cell. The C/5 discharge was performed using an Arbin high current battery cycler with cell temperature of 20˚C. The estimated parameters denoted in Tables 2.2-2.5 were derived from a preliminary study on parameter estimation from this discharge data.

Table 2.7. Equations of the Tanks-in-Series Model with Logarithmic Time Scaling.

Cathode (Region 1)

$$\frac{d(\varepsilon_1)}{dt}+\frac{d(C_{1,i})}{dt}=\frac{1}{e^{C_{1,i}}e^{\varepsilon_1}}\left(\frac{-N_{mid,i}}{l_1}+\bar{r_i}-\overline{R_{1,i}}\right)$$

$$\sum_i z_i\frac{d(e^{\varepsilon_1}e^{C_{1,j}})}{dt}=0$$

$$\frac{i_{app}}{l_1}=\bar{a}\sum_j\bar{i_j}$$

$$\frac{d\varepsilon_{1,k}}{dt}=\frac{1}{e^{\varepsilon_{1,k}}}\left(\tilde{V}_k\overline{R'}_k\right)$$

$$\frac{d\varepsilon_1}{dt}=\frac{1}{e^{\varepsilon_1}}\left(-\sum_k\tilde{V}_k\overline{R'}_k\right)$$

Separator (Region 2

$$\frac{d(\varepsilon_2)}{dt}+\frac{d(C_{2,i})}{dt}=\frac{1}{e^{C_{2,i}}e^{\varepsilon_2}}\left(\frac{N_{mid,i}-N_{2,Li^+,x=l_1+l_2}}{l_2}-\overline{R_{2,i}}\right)$$

$$N_{2,i=Li^+,x=l_1+l_2}=\frac{i_{app}}{F}$$

$$\sum_i z_i\frac{d(e^{\varepsilon_2}e^{C_{2,i}})}{dt}=0$$

$$\frac{d\varepsilon_{2,k}}{dt}=\frac{1}{e^{\varepsilon_{2,k}}}\left(\tilde{V}_k\overline{R'}_k\right)$$

$$\frac{d\varepsilon_2}{dt}=\frac{1}{e^{\varepsilon_2}}\left(-\sum_k\tilde{V}_k\overline{R'}_k\right)$$

Interfacial Expressions

$$\phi_{e,mid}=\frac{e^{\left(\varepsilon_1\right)^{b_1}}\delta_2\overline{\phi_{1,e}}+e^{\left(\varepsilon_2\right)^{b_2}}\delta_1\overline{\phi_{2,e}}}{e^{\left(\varepsilon_1\right)^{b_1}}\delta_2+e^{\left(\varepsilon_2\right)^{b_2}}\delta_1}$$

$$C_{mid,i}=\frac{\delta_2e^{\left(\varepsilon_1\right)^{b_1}}e^{C_{1,i}}+\delta_1e^{\left(\varepsilon_2\right)^{b_2}}e^{C_{2,i}}}{e^{\left(\varepsilon_1\right)^{b_1}}\delta_2+e^{\left(\varepsilon_2\right)^{b_2}}\delta_1}$$

$$N_{mid,i}=D_{i0}\frac{e^{\left(\varepsilon_1\right)^{b_1}}e^{\left(\varepsilon_2\right)^{b_2}}}{e^{\left(\varepsilon_1\right)^{b_1}}\delta_2+e^{\left(\varepsilon_2\right)^{b_2}}\delta_1}\left[\left(e^{C_{1,i}}-e^{C_{2,i}}\right)+\frac{z_i}{RT}FC_{mid,i}\left(\overline{\phi_{1,e}}-\overline{\phi_{2,e}}\right)\right]$$

Other Expressions

$$\bar{r_i}=-\bar{a}\sum_j\frac{s_{i,j}\bar{i_j}}{n_jF}$$

$$\overline{U_{j,ref}}=U_j^{\theta}-\frac{RT}{n_jF}\sum_i s_{ij}\ln\left[\frac{e^{C_i}}{1000}\right]$$

$$\bar{a}=a_0\left(\frac{e^{\varepsilon_1}}{e^{\varepsilon_{1,initial}}}\right)^{\xi}$$

$$\overline{R_i}=\sum_k\gamma_{i,k}\overline{R'_k}$$

$$\overline{\eta_j}=\overline{\phi_s}-\overline{\phi_{1,e}}-\overline{U_{j,ref}}$$

$$\overline{R'_k}=k_ke^{\varepsilon_k}\left(\prod_i e^{C_i^{\gamma_{i,k}}}-K_{sp,k}\right)$$

$$\bar{i}_j=i_{o,j_{ref}}\left\{\left(\frac{e^{C_{i,anodic}}}{e^{C_{i,ref}}}\right)^{s_{i,j}}\exp\left(\frac{\alpha_{a,j}F}{RT}\overline{\eta_j}\right)-\left(\frac{e^{C_{i,cathodic}}}{e^{C_{i,ref}}}\right)^{-s_{i,j}}\exp\left(-\frac{\alpha_{c,j}F}{RT}\overline{\eta_j}\right)\right\}$$

2.5 Results and Discussion

The Tank-in-Series model (Tank model) was developed through volume averaging of the one-dimensional model (1D model), which necessitated assumptions for interfacial flux. The dimensionless parameter delta, where $delta = \delta_l / l_l$, i.e., the dimensionless fraction of the cathode and the separator, was introduced to describe the approximate length scale where gradients occur within the domain. To understand how well the Tank model performs in comparison with the 1D model, a preliminary parametric study was performed by varying the C rate, intrinsic diffusion coefficients, the cathode thickness, and exchange current densities, listed in Table 2.8. The three different rates considered are 0.2C, 0.5C, and 1C, which are appropriate for the energy demands for electric vehicles[33]. The diffusion coefficient for all ionic species except the anion was assumed, to simplify the model, while the anion was assumed to be a typical lithium salt, such as bis(trifluoromethane)sulfonimide (TFSI−), with an appropriate diffusion coefficient[34]. The cathode thickness included the base case from the Kumaresan model and twice the base case. The exchange current densities for each reaction were varied orders of

Table 2.8. Values of the Parameter Study

Parameter	Value
C Rate	0.2, 0.5, 1.0
Diffusion Coefficient, D_{i0} (m^2/s)	1×10^{-10}, 1×10^{-11}, 1×10^{-12}
Cathode thickness, l_1 (μm)	40, 80
Exchange current density, $i_{0\,j}$, $j = 2..6$ *	1×10^{-4}, 1×10^{-2}, 1×10^{2}

*not shown

magnitude above and below the base case; the results follow the general trends discussed below and are not shown.

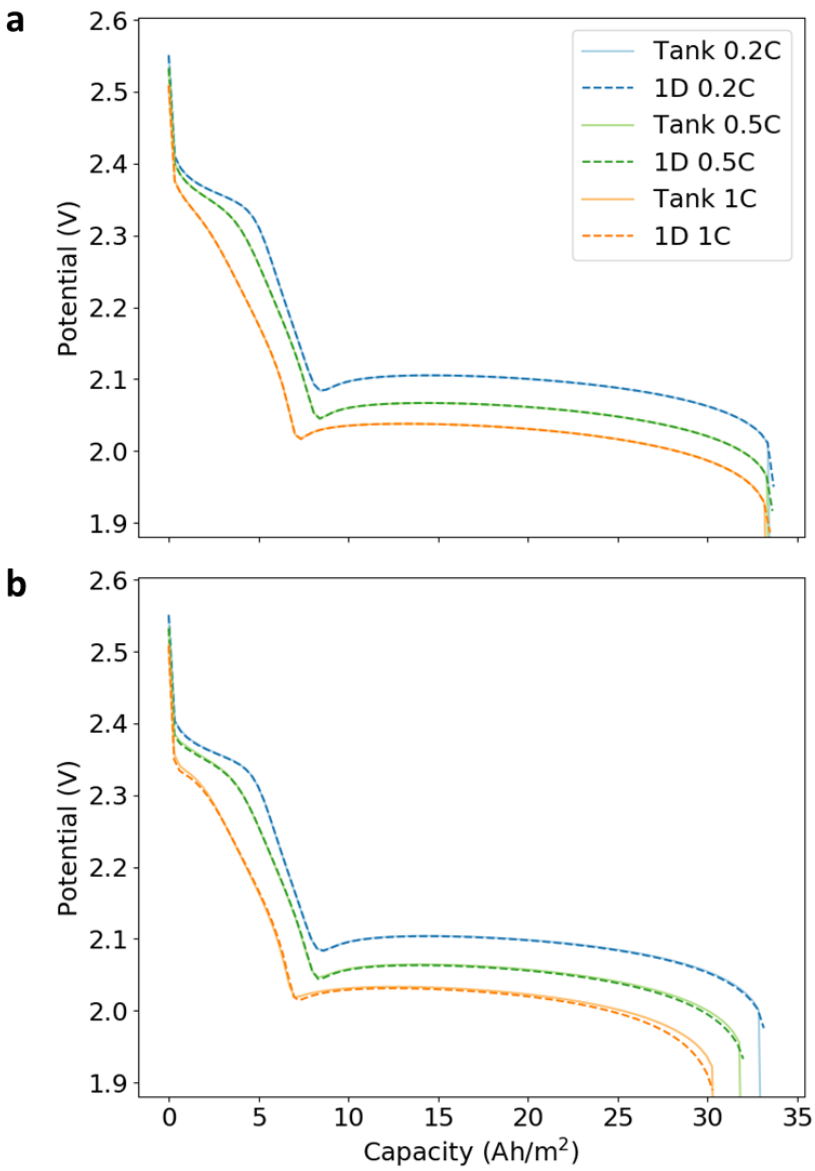

Figure 2.2. Comparison of Tank-in-Series model ($delta = 1/3$) and 1D model predictions at rates of 0.2C (blue), 0.5C (green), and 1C (orange) (a) with diffusion coefficient $D_{i,0} = 1 \times 10^{-10}\ m^2/s$ where results are almost identical, (b) with diffusion coefficient of $D_{i,0} = 1 \times 10^{-11}\ m^2/s$ where transport limitations are introduced and some variation is introduced at the end of discharge.

Results with the base case parameters are shown in Figure 2.2 (a). For this parameter set and discharge rates, the 1D model shows there are negligible transport limitations in the Li-S cell. That means species concentrations and partial currents are relatively uniform across the electrode, reducing the underlying cause of distinctions between the Tank model and the 1D model. In this limiting case of negligible transport, we expect the Tank model to match the more complete 1D model, and this is observed

in Figure 2.2 (a). Convergence between two independent models under appropriate limiting conditions is good evidence for computational accuracy.

The computation time for the discharge curve in Figure 2.2 (a) was 40 ms. In contrast, the 1D model required at least 10x more time for evaluation. The benefits of this 5-10-fold computational speed up is critically felt in model-based parameter estimation or optimal design, where thousands of model calls are implemented. To have confidence using this fast-computing Tank model for parameter estimation or optimal design outside of the negligible transport limitation regime, we explore parameters and operating rates that induce concentration gradients within the cell, allowing us to probe the Tank model suitability (compared to the 1D model) under more challenging conditions.

To explore the Tank model approximations, the diffusion coefficient was varied over 3 orders of magnitude, which resulted in different transport effects on the solution. For the voltage curves in Figure 2.2 (a), the diffusion coefficient of $1x10^{-10}$ m^2/s was used in the Tank model and the 1D model, which match at all rates, indicating that the concentration profile is in fact uniform. To quantify the variation in concentration across the cathode, we can calculate a spread of the soluble sulfur equivalents and normalize by the average concentration, resulting in 42% ($\Delta C/C_{avg}$ x 100%) for the 1D model at the 1C rate at 95% of total discharge. The diffusion coefficients are the same order of magnitude as the base parameters from the work by Kumaresan et al. Work by Zhang et al.[10] show that the original Kumaresan model parameters are kinetically-limited and do not capture rate capability well at higher discharge rates. Their work found that changing the ionic diffusion coefficients by one to two orders of magnitude, the model was able to predict experimental data more accurately under varying rates.

Next, let us consider the next set of simulations with diffusion coefficient of $1x10^{-11}$ m^2/s to introduce additional transport limitations, (Figure 2.2 (b)). At 0.2C and 0.5C rates, the difference in predictions between the 1D and Tank models is negligible. The simulations at 1C indicate the overall voltage response is closely matched until the end of discharge, where there is slight deviation. Lowering the diffusion coefficient to $1x10^{-11}$ m^2/s increases transport limitations, as indirectly evidenced by the reduction in overall capacity as a function of rate. The more direct measure of increased transport limitations is the variation in concentration across the cathode, which is 287% ($\Delta C/C_{avg}$ x 100%) for the 1C rate in the 1D model for normalized soluble sulfur equivalents at 95% of discharge. In Figure 2.2, a *delta* value of $\frac{1}{3}$ is used to best match the 1D model predictions.

As we decrease the diffusion coefficient by an additional order of magnitude, further accentuating transport effects, the effect of the Tank model parameter, *delta*, becomes more important (Figure 2.3). This extra parameter, *delta*, is an approximate diffusion length that can be seen as a transport fitting parameter. Under conditions where transport limitations are significant, the Tank model approximations break down, and the 1D model and the Tank model are expected to deviate. In fact, the Tank model predictions

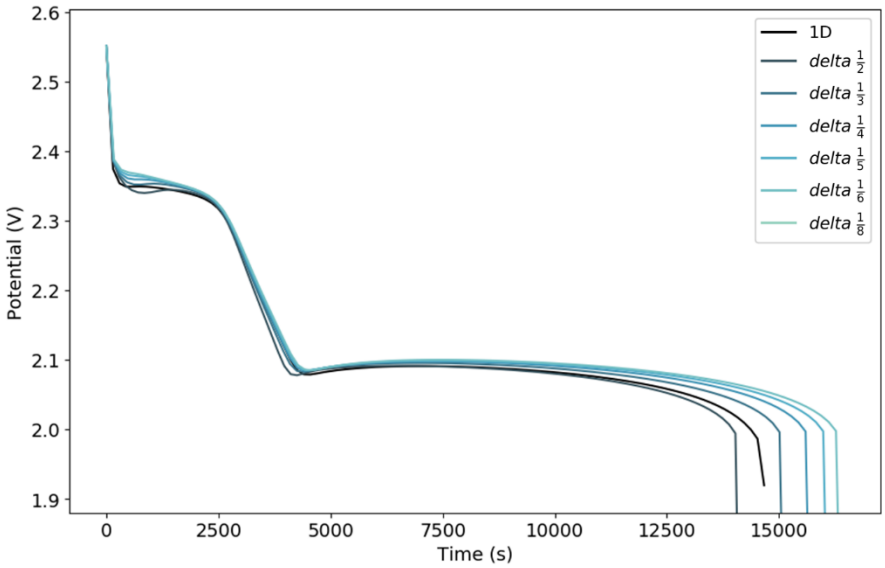

Figure 2.3. Effect of the parameter *delta* on the Tank predictions at 0.2C with diffusion coefficient of $D_{i,0} = 1 \times 10^{-12}\ m^2/s$.

become sensitive to the *delta* chosen. As *delta* is increased, the apparent transport limitations increase in the Tank model, resulting in decreased capacity and increased polarization. Generally, the Tank model matches best with a *delta* between ½ and ⅓, depending on the parameters and rates being used. With the diffusion coefficient of 1x10^{-12} m^2/s, the simulations are limited to the 0.2C rate and base case cathode thickness; higher rates and cathode thicknesses cause the Tank model to experience a singularity. Under such extreme transport conditions, the Tank model greatly overpredicts interfacial fluxes and potentials, leading to the numerical instability at higher rates.

When considering thicker cathodes, the trends are similar to the impact of lowering diffusion coefficients. Figure 2.4 (a) shows the voltage curves of the Tank and 1D model with double the cathode thickness (80 μm and 1x10^{-11} m^2/s diffusion coefficient at 1C rate). The diffusion limitations are increased when compared to the base case of 40 μm. As transport becomes more limiting, some detailed features of the discharge curve are missed in the Tank model, such as the voltage dip in the 1D model, and the Tank model

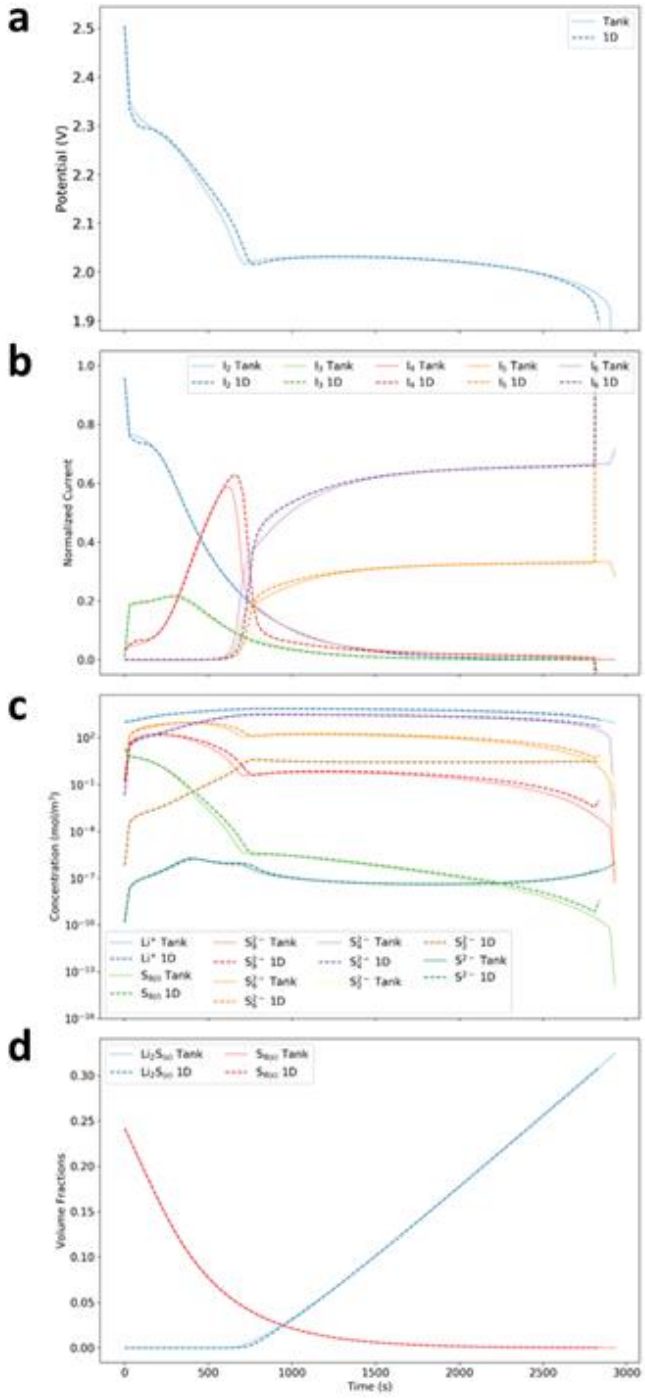

Figure 2.4. Predictions for the $D_{l,0} = 1 \times 10^{-11}\ m^2/s$ case with l_1 x 2 at a rate of 1C with the Tank model ($delta = 1/2$) and the 1D model **(a)** voltage curves; **(b)** the partial currents of Reactions (2) through (6) normalized by the overall applied current, i_{app}; **(c)** logarithmic plot of the concentration of ionic species within the cathode, **(d)** plot of the volume fractions of the species, S_8(s) and Li_2S(s). In Figure 2.4**(b)-(d)**, the values for the 1D model have been integrated over the cathode domain to compare to the Tank model.

somewhat overpredicts the capacity.

The power of physics-based models is the ability to identify underlying physical phenomena that govern the overall battery's voltage response. To illustrate this point, the temporal progression of partial currents for each charge transfer reaction (Eqs. 2.2-6) within the cathode are shown in Figure 2.4 (b) for the Tank model and the 1D model, where the values are normalized by the applied current (set by C-rate) so they sum to 1 at all times. For the 1D model, the partial

currents are integrated across the cathode to obtain average values. Figure 2.4 (b) shows that the beginning of discharge is dominated by charge transfer through Reaction (2.2) with some contributions from Reaction (2.3), the next reaction in the reduction cascade. Small discrepancies between the 1D and Tank model begin with the peak partial current from Reaction (2.4), around the voltage transition between the two plateaus. The second voltage plateau is primarily set by the passage of current through the last two reactions, until the end of discharge. The 1D model better accounts for the increased spatial variations at the end of discharge, which explains the decreased capacity compared to the Tank model. When the 1D model reaches the end of discharge, the S_4^{2-} and S_2^{2-} species concentrations fall to zero near the terminals, while the concentrations near the separator dramatically increase. The resulting divergences in local currents are reflected in the average values. The Tank Model does not exhibit this effect to the same extent since the average reaction rates are estimated using the average concentrations, resulting in underprediction of the currents.

Figure 2.4 (c) shows the concentrations of all the ionic species within the cathode. Over different orders of magnitude, the models match well, and the shapes of the concentrations are captured well by the Tank model even at these conditions. The volume fractions of the solid species are shown in Figure 2.4 (d). Both the concentrations and the volume fractions in the 1D model have been integrated across the cathode to calculate average values. The Tank model matches the 1D model well with a slight discrepancy at the beginning of the Li_2S precipitation, corresponding to the beginning of the second plateau in the voltage curve.

The solution for the Tank model is more computationally efficient, has fewer

numerical instabilities, and does not require discretization along the cell thickness. However, there is a key dilemma in using a simplified model ideally suited to a limiting case (such as modest transport limitations); namely, are there short cut methods that can help us have confidence in a simplified model output, without needing to run the 1D model? To quantify the 1D model and Tank model prediction accuracy, model variance was calculated in two different ways.

The first type of error calculation was the root mean square error (RMSE) of the voltage responses between different pairs of model predictions. In Figure 2.5 (a), the y axis represents the error between the 1D model and the Tank model with *delta* of ½ while the x axis of Figure 2.5 (a) is the difference between two instances of the Tank model with *delta* of ½ and ⅓. Recall *delta* represents the fraction of each region where gradients are expected. As shown in Figure 2.3, the Tank model is sensitive to delta and deviates from

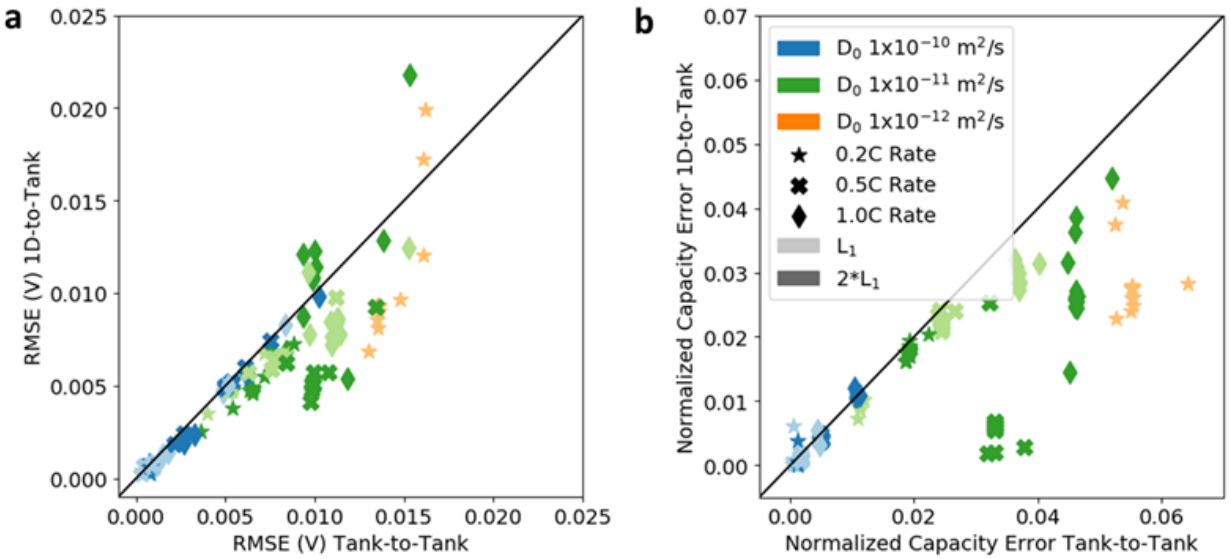

Figure 2.5. Plots of the **(a)** of the Root Mean Square Error (RMSE) of the voltage, **(b)** of the total capacity normalized by the theoretical capacity error where the y axis is the error between the 1D model and the Tank model ($delta = ½$) and the x axis denotes the error between two Tank model simulations ($delta = ½, ⅓$). Each of the symbol and color combinations represents a different set of levels for each parameter, denoted by color (diffusion coefficient), symbol (rate), and shade (cathode thickness).

the 1D model when transport limitations matter. Figure 2.5 (a) shows two ways to probe transport errors, by the RMSE error of the voltage measures. For every simulation performed, the variables being modified from base conditions are represented by color (diffusion), symbol shape (C-rate), and electrode thickness (light or dark shade). The majority of the points lie near or below around the 45-degree line, indicating the error between the 1D model and the Tank model is equal to or less than the error between the two Tank models with *delta* varied. Fundamentally, this means that changing *delta* in the Tank model is typically a more sensitive probe of whether the Tank model approximations are breaking down than a comparison of the Tank to 1D model. Thus, it is generally not needed to use the 1D model to assess if transport is increasingly important. It is important to note that the RMSE for all simulations shown are below 25 mV. For the parameter ranges explored here, the Tank model thus predicts the voltage response accurately.

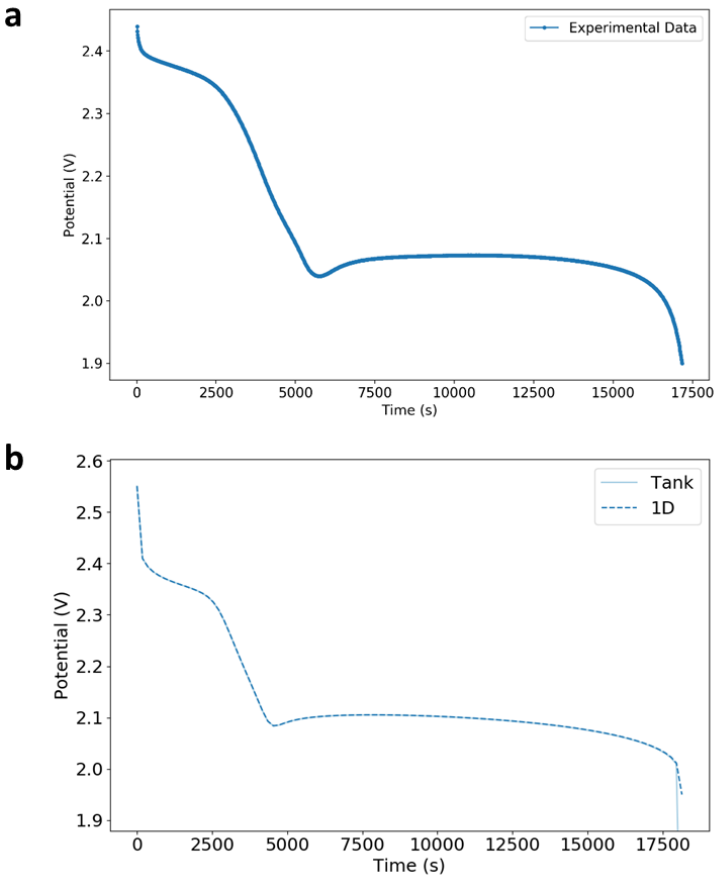

Figure 2.6. Lithium Sulfur Discharge Curves (a) from experimental data of a proprietary, pre-commercial pouch cell at C/5, (b) simulated curves comparing the 1D model and the Tanks-in-Series model at C/5 with estimated parameters that exhibit the all the main features from the experimental curve.

While the RMSE captures deviations in voltage between the two models, the second type of error emphasizes the total capacity, another important feature. In Figure 2.5 (b), the normalized capacity errors between the models are plotted, with the differences between the 1D model and Tank model on the y axis and differences between the two deltas in Tank models on the x axis. To make these calculations, every final capacity value is divided by the theoretical capacity. On average, the capacity errors lie in an envelope below the 45-degree line, again indicating better agreement between the 1D model and the Tank model with *delta* of $\frac{1}{2}$ than between the Tank models with *deltas* of $\frac{1}{2}$ and $\frac{1}{3}$. The same general trends related to the effects of diffusion coefficients, C-rates, and cathode thicknesses are seen in Figure 2.5 (a) and Figure 2.5 (b), with more clustering by parameter within the capacity errors. Importantly, the errors in capacity are less than 7%, for all simulations considered.

To illustrate the relevance of both the 1D and the Tank model for experiments, Figure 2.6 (a) shows a C/5 discharge curve from the proprietary Li-S pouch cell. In Figure 2.6 (b), the Tank and the 1D model predictions are compared at a C/5 rate. The overall features and shape of the experiment curve, including the characteristic two plateaus, are captured well by both the Tank and the 1D models. The agreement between the two models and experiment in Figure 2.6 indicates that the chosen values of base case parameters are experimentally meaningful. Future work will present detailed discussion on parameter estimation and validation at different conditions and rates for Li-S batteries.

2.6 Conclusions and Implications

In this work, we have discussed the development of a Tanks-in-Series model that is volume averaged from the 1D discharge model for lithium sulfur batteries. The Tank model captures overall trends and average variables. Although a lumped model, the diffusion coefficients play a role in transport between the two tanks through the interfacial fluxes, in a similar fashion to the detailed 1D, spatially resolved model. For the parameter set considered in this work, the Tank model predictions match well in the majority of simulations and are able to recreate the qualitative features predicted by the 1D model. The voltage trends are matched closely, even though the accuracy of capacity prediction is somewhat variable in diffusion-limited regimes.

While the 1D model contains more information than the Tank-in-Series model, this comes at a computational cost, evidenced in the computation times, which are higher by 1-2 orders of magnitude. The increased efficiency makes the Tank model an ideal candidate for parameter estimation, where it can be leveraged to identify regions where the model achieves acceptable agreement with experimental data. If further spatial resolution is vital to understanding a problem, the initial guesses from the Tank model can then be fed into the 1D model, given the one-to-one correspondence of parameters. While other lumped models focus on trend predictions and speed, the Tank model can match experimental data with increased speed compared to the 1D model.

Based on an analysis of errors in Figure 2.5, it is recommended users implement the Tank model with *delta* as ½ for parameter estimation or design. When parameters are found, we can compare the simulations between the Tank models with *delta* of ½ and

a second calculation with *delta* of ⅓ (and all other parameters set). If there is an acceptable voltage RMSE or capacity difference between the two Tank simulations, then transport limitations are deemed modest, and the Tank model is expected to be an acceptable representation of the 1D model. If the error between the two Tank models (with *delta* of ½ and ⅓) is unacceptably large, the Tank results can be deemed a first guess for a 1D model estimation or design analysis.

As modeling of lithium sulfur batteries advances and mechanisms are improved, the Tanks-in-Series model can be modified to include more physics as needed. For future studies, the focus will be on using the Tanks-in-Series model in parameter estimation to improve model fit to experimental data for a range of rates and conditions.

2.7 Acknowledgments

The authors would like to thank the U.S. Department of Energy (DOE) for providing partial financial support for this work, through the Advanced Research Projects Agency (ARPA-E) award number DE-AR0000275, Advanced Battery Material Research (BMR) Program (Battery 500 Consortium). The authors would also like to thank the Clean Energy Institute (CEI) at the University of Washington, and Texas Materials Institute for partial monetary support of this work.

Chapter 3

Realigning the Chemistry and Parameterization of Lithium Sulfur Battery Models to Accommodate Emerging Experimental Evidence and Cell Configurations

Note: this chapter was published as an article.

C. Parke, A. Subramaniam, V. Subramanian, D. Schwartz, Realigning the Chemistry and Parameterization of Lithium Sulfur Battery Models to Accommodate Emerging Experimental Evidence and Cell Configurations, *Beyond Lithium Ion Special Collection of ChemElectroChem*. **8**, 1098 (2020).

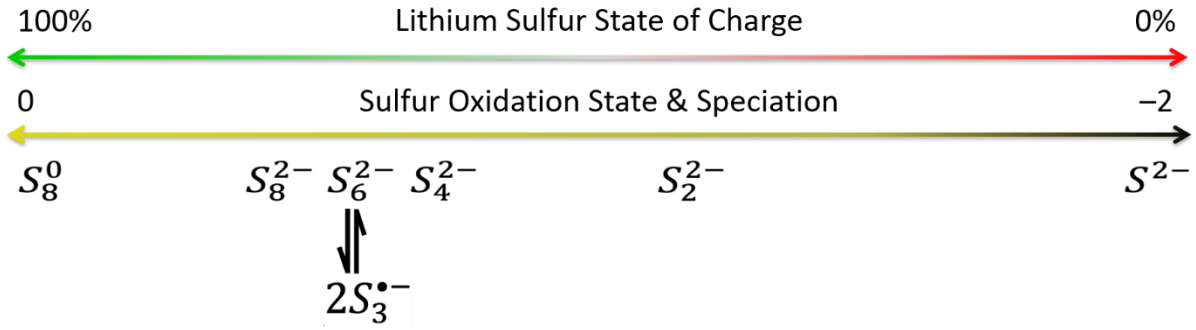

Figure 3.1. Schematic that shows the variation of sulfur oxidation state and speciation with state of charge.

The electrochemical model for lithium sulfur batteries is updated to include a radical species that is widely reported in spectroscopy studies of Li-S electrolytes, but has never been included in physics-based models of the Li-S battery. Model parameters are also updated to reflect experimental advances in cell energy density.

Keywords: Batteries, Electrochemistry, Lithium, Modeling, Sulfur

3.1 Abstract

Experimental insights into lithium sulfur (LiS) battery chemistry have resulted in practical improvements in cell coulombic efficiency, sulfur utilization, and cycle life. However, optimization of this complex battery chemistry requires experimentally-aligned modeling tools. A porous electrode theory-based model incorporating key electrolyte dissociation chemistry is developed for the LiS cell. The proposed chemistry produces a radical anion species that is widely observed spectroscopically in LiS electrolytes. We explore the implications of radical anion formation on the current-voltage behavior within the context of a state-of-art high energy density LiS cell with low electrolyte:sulfur (E/S) ratio and ideally-protected anode. Parameters describing the dissociation reaction equilibrium and kinetics are shown to alter the electrolyte speciation in ways that can be linked to observations from LiS electrolyte engineering experiments.

3.2 Introduction

As lithium ion batteries reach their theoretical limits, lithium sulfur (LiS) chemistry is emerging as a promising next-generation battery with high energy density to meet the burgeoning demands for electric transport applications. Lithium sulfur batteries have a theoretical energy density of 2600 Wh/kg, and some companies are claiming 400 Wh/kg already[16]. The challenges facing adoption of this chemistry include poor cycle life, low Coulombic efficiency, and loss of active material during cycling[35].

For practical lithium sulfur batteries, polysulfide speciation and transport in the electrolyte, so-called polysulfide shuttling, is central to understanding LiS performance. Specifically, soluble higher-order polysulfide anions form during discharge and their transport to the anode leads to deleterious reactions with the lithium metal[3,17]. Protection of reactive lithium surfaces, either through formation of a stable solid-electrolyte interface (SEI) or via engineered coatings, is crucial to cyclability[36]. The sulfur in a fully charge cathode is insulating, as is the conversion product $Li_2S_{(s)}$ in a fully discharged cathode. Thus, the conductivity of the cathode is typically enhanced by making a porous sulfur/carbon composite electrode, lowering the energy density of the cell[37]. During discharge, the distribution of precipitated $Li_2S_{(s)}$ within the composite cathode can contribute to passivation and poor sulfur utilization[38]. Ultimately, the electrolyte formulation plays an especially important role in this battery chemistry and makes up a large amount of the overall weight (about 40% in a calculation for 300 Wh/kg cell)[39]. To support the highest practical energy densities, the experimental trend is toward “lean”

cells with ever lower electrolyte to sulfur ratios (E/S)[16,40,41].

Electrolyte engineering — the design of solvent, salt, and additive systems — has profound impact on the shape of the voltage curve, cell capacity, and cyclability, owing to changes in soluble polysulfide speciation, insoluble product formation, conductivity, and reactivity with the anode[36,42-45]. Experimental methods such as *in situ* Raman spectroscopy have proven valuable for showing how specific additives[46] and ether-based electrolytes[47] can alter speciation between long and short-chain polysulfides within the electrolyte, while also squelching or promoting stable formation of polysulfide radicals such as $S_3^{\bullet-}$. Likewise, the effects of varying solvent donor numbers (DN) on polysulfide speciation has been probed using UV-Vis spectroscopy[48], a technique that is sensitive to a wide array of polysulfide species[49,50]. It was shown that solvent choice significantly impacts homogeneous chemistry in the electrolyte, sometimes favoring the stable formation of radical anion $S_3^{\bullet-}$ from its dimer anion S_6^{-2} via the dissociation reaction[48]

$$S_6^{2-} \rightleftharpoons 2S_3^{\bullet-} \tag{3.1}$$

Though quantitative experimental measures of all the polysulfide species concentrations under battery-like operating conditions have not been reported, *in situ* and *operando* spectroscopy experiments clearly show the balance of species in dissociation Reaction (3.1) are strongly modulated by electrolyte engineering strategies, along with the overall discharge behavior of LiS batteries.

Physics-based modeling of batteries seeks to integrate experimentally-relevant chemistry and transport in ways that yield important insights about system performance and key underlying mechanisms. Modeling studies for lithium sulfur batteries began in 2004 with a lumped model that described thermodynamics and kinetics primarily with a

simplified reaction scheme[3]. In 2008, Kumaresan et. al.[4] developed what has become the *de facto* standard one-dimensional model (1D) for LiS batteries. Kumaresan et. al. included a multi-step sulfur reduction cascade with several soluble polysulfide intermediates and the insoluble $Li_2S_{(s)}$ precipitate, morphology evolution, kinetics, transport, and thermodynamics to describe lithium sulfur battery behavior. Since 2008, there have been quite a few studies to reconcile differences between experimental observations and the original Kumaresan et. al. model, but there has been no fundamental reconsideration of polysulfide chemistry and speciation within full-cell continuum modeling, despite advances in understanding of electrolyte homogeneous chemistry driven by *in situ* and *operando* spectroscopy experiments.

For example, Ghaznavi et al. probed the parameter space of Kumaresan's model, and found that the model was only suitable for representing the discharge curve, and failed upon charging[51-53]. Neidhardt et al. published a similar model[5] and later explored impedance[6] and capacity fade through polysulfide shuttle[8]. Further work assumed trapped polysulfides and modeled only lithium ion transport within a nano-structured cathode[54]. A study by Zhang et. al. with a lumped model added electrolyte conductivity to better match experimental impedance data[14]. Moy et al. developed a one-dimensional model for shuttle current under constant voltage operation; their work was combined with experimental efforts involving the additive $LiNO_3$ that is purported to suppress the polysulfide shuttling[55]. With a simplified two-step reduction scheme, Marinescu and associates published a lumped model that described charge and discharge with precipitation of lithium sulfide[11]. Zhang et. al. concluded that the ionic diffusion coefficients within the Kumaresan model needed to be decreased by a factor of 100 to

introduce rate dependencies seen in experimental work[10]. A study by Yoo et. al. modified the precipitation terms of the Kumaresan model to alleviate numerical instabilities and show reasonable charging curves[7], but the results have proven difficult to reproduce[54]. Similarly, work by Ren et. al.[15] focused on improving the precipitation kinetics through rate-dependent precipitation with experimental validation through SEM characterization of electrodes. A discharge model based on concentrated solution theory was developed by Mistry and Mukherjee that focused on the transport dynamics[57]. Marinescu et. al. studied degradation and classified capacity loss as reversible from chemical dissolution issues or irreversible from the polysulfide shuttling[58]. Shim et al.[59] published a study that combined experimental work and model work to explore the effect of $LiNO_3$ that may promote formation of an irreversible solid product within the cathode. With excessive additive, their results showed distortion of the voltage curve with a third plateau at the end of discharge, and the modeling was able to replicate this feature by decreasing the rate of the last reduction reaction, which caused a third voltage drop and distinct precipitation regimes of $Li_2S_{2(s)}$ and $Li_2S_{(s)}$. Work by Kamyab et. al. reported updated $Li_2S_{(s)}$ precipitation parameters that work for charging and studied the effect of polysulfide shuttle on cycling[56].

Our recently published work detailed a reduced-order model with decreased computational footprint that lacked spatially-resolved speciation, but still incorporates transport effects between electrode and separator compartment[60]. Here we rely on macrohomogeneous porous electrode theory to represent the 1-D spatial variation of all

species across the complex sulfur/carbon composite cathode and separator, as shown in Figure 3.2. More sophisticated models for cathode structure have explicitly incorporated the influence multi-scale hierarchy in the sulfur-infused mesoporous carbon particles[61]. While our focus here is on aligning the modeled electrolyte chemistry to observed electrolyte speciation, future work may benefit from more multiscale models of the cathode itself.

Table 3.1. Geometric Parameters for 300 Wh/kg Cell.

Parameter	Value
Sulfur content in cathode (wt %)	60%
Areal sulfur loading (mg/cm^2)	4.9
Sulfur volume fraction [a]	0.24
Cathode thickness (μm) [a]	100
Separator Thickness (μm) [a]	20
E/S ratio (mL/g)	1.45
Cathode porosity [a]	0.60
Separator porosity [a]	0.60
Carbon/binder volume fraction [a]	0.16
Areal capacity (mAh/cm^2)	4.9
Cathode specific capacity (mAh/g)	1005

[a] Input parameters to the model

Although battery modeling has not yet incorporated electrolyte chemistry such as Equation (3.1) to understand its potential impact on whole-cell performance, sophisticated electroanalytical models by Thangavel et. al.[62] have. In particular, Thangavel et. al. performed cyclic voltammetry (CV) experiments in a three electrode cell using a planar glassy carbon working electrode in an electrolyte with Li_2S_8 or Li_2S_6 as the (initial) electroactive species in 1M LiTFSI supported TEGDME:DOL electrolyte. A 1D model of the working electrode and adjacent electrolyte diffusion layer could not describe experimental CV results using the original reduction chemistry cascade proposed by Kumaresan et. al. With the addition of an alternative reaction pathway involving $S_3^{\bullet-}$ and S_3^{2-} species, the entire CV was successfully modeled and a set of reaction parameters were estimated. The work by Thangavel et. al. represents one of the most promising ways to explore coupled electrochemical/chemical polysulfide chemistry and extract meaningful parameters that can be adapted to the more complex battery configuration where the

anode and cathode are strongly coupled because of the small electrolyte volumes and high surface area electrodes.

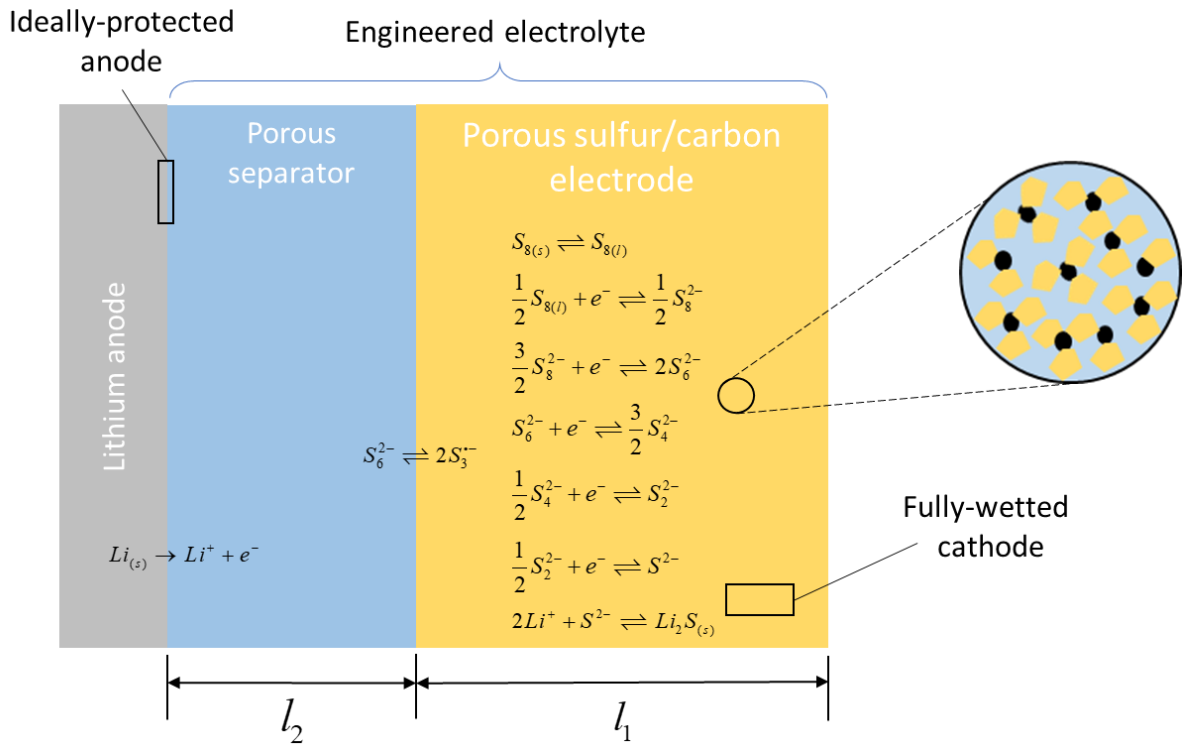

Figure 3.2. Schematic of lithium sulfur sandwich layer with lithium anode, porous separator, and composite cathode with yellow solid sulfur particles, black conductive carbon, and binder.

Other issues associated with aligning current modeling with trends in experimental research, beyond electrolyte speciation, are small but worth acknowledging. For example, the extensive experimental literature that documents how to build high energy density cells includes critical parameter ranges for sulfur areal loading and weight percent, E/S ratios, cathode thicknesses, and porosities; these parameters are often easily related to the volume fractions, porosities, and thicknesses preferred by modelers. Less straightforward is relating the E/S ratio between experiments and modeling. Generally, E/S ratio is taken as an independent parameter in experiments that can be varied for a given electrode and separator sandwich. In contrast, the E/S ratio in a 1D model is set by cathode/separator/anode sandwich geometry, combined with the assumption of a fully-

wetted pore-volume. The only way to change the E/S ratio in a 1D model is to change the pore volume of the separator and electrodes. For this model, the E/S ratio is fixed by cell geometry to a value just below 2 mL/g, which is at the highest energy-density end of experimentally-relevant values.

The work herein fundamentally builds off the Kumaresan et al. model of a LiS cell, as shown schematically in Figure 3.2. Updated geometric parameters in Table 3.1 correspond to high energy density lithium sulfur batteries, calculated according to estimates for a 300 Wh/kg pouch cell[39]. Our base case uses the most experimentally-relevant physicochemical parameters available in the battery modeling literature. Inclusion of the electrolyte chemistry shown in Equation (3.1) allows for the generation of $S_3^{\bullet -}$ radical, an electrolyte species widely observed in lithium sulfur battery studies[63-68]. By adding Reaction (3.1), we can explore, for the first time, how this homogenous, non-charge-transfer dissociation reaction is linked to the discharge behavior of a lithium sulfur battery with state-of-art geometric and physicochemical parameters.

3.3 Results and Discussion

To modernize the lithium sulfur electrochemical model and update it to match current understanding of the complex interdependence of electrolyte, additives, and speciation, new chemistry has been included. Specifically, dissociation of polysulfide anions into constituent radical anions has been reported in many experimental papers[31,47,48,63,65,67,69,70]. We take this dissociation reaction to be a reversible, non-charge transfer reaction occurring homogeneously in the electrolyte according to Reaction (3.1). Because the reaction is presumed reversible and elementary as written, the forward and backward reaction rates are $R_f = k_f \left[S_6^{2-} \right]$ and $R_b = k_b \left[S_3^{\bullet -} \right]^2$. At equilibrium, the reaction rates will be equal, which allows us to define a reaction equilibrium constant, K_{S3}

$$K_{S3} = \frac{k_f}{k_b} = \frac{\left[S_3^{\bullet -} \right]^2}{\left[S_6^{2-} \right]} \tag{3.2}$$

where the square brackets denote the activity of the respective polysulfide species, which is assumed to be the concentration here. This reversible reaction is a sink for S_6^{2-} ions and the only source of the $S_3^{\bullet -}$ radical species. In particular, the newly modified species balance for S_6^{2-} is

$$\frac{\partial \varepsilon C_{S_6^{2-}}}{\partial t} = -\frac{\partial N_{S_6^{2-}}}{\partial x} + r_{S_6^{2-}} - \varepsilon k_f \left(C_{S_6^{2-}} - \frac{C_{S_3^{\bullet -}}^2}{K_{S3}} \right) \tag{3.3}$$

Where ε is the porosity, $C_{S_6^{2-}}$ is the concentration of S_6^{2-}, $N_{S_6^{2-}}$ is the flux that includes diffusion and migration of S_6^{2-}, $r_{S_6^{2-}}$ is the rate of the electrochemical reactions that include

$S_6^{2-}, C_{S_3^{\bullet-}}$ is the concentration of $S_3^{\bullet-}$ species. The S_6^{2-} anion is directly involved in the electrochemical reduction cascade on the cathode. A wholly new species balance is added to the Kumaresan et. al. model for the radical anion $S_3^{\bullet-}$ species

$$\frac{\partial \varepsilon C_{S_3^{\bullet-}}}{\partial t} = -\frac{\partial N_{S_3^{\bullet-}}}{\partial x} + 2\varepsilon k_f \left(C_{S_6^{2-}} - \frac{C_{S_3^{\bullet-}}^2}{K_{S3}} \right) \tag{3.4}$$

We assume the $S_3^{\bullet-}$ species does not directly participate in the electrochemical reduction cascade on the cathode, and can only influence the discharge curve by acting as a sink for S_6^{2-} species, which then is not available to react within the reduction cascade. The dissociation reaction parameters k_f and K_{S3} respectively dictate the time-scale for Reaction (3.1) and the equilibrium distribution of the two species involved in Reaction (3.1). The complete set of equations for the lithium sulfur electrochemical model is included as Table 3.2.

Table 3.2. Lithium Sulfur Mathematical Discharge Model.

Governing Equations	**Boundary Conditions**
Positive Electrode (Region 1)	
$\frac{\partial \varepsilon_1 C_{1,i}}{\partial t} = -\frac{\partial N_{1,i}}{\partial x} + r_i - R_i$	$C_{1,i}\big\|_{x=l_1} = C_{2,i}\big\|_{x=l_1}$
$\frac{\partial \varepsilon_1 C_{1,S_6^{2-}}}{\partial t} = -\frac{\partial N_{1,S_6^{2-}}}{\partial x} + r_{S_6^{2-}} - \varepsilon_1 k_f \left(C_{1,S_6^{2-}} - \frac{C_{1,S_3^{\bullet-}}^2}{K_{S3}} \right)$	
$\frac{\partial \varepsilon_1 C_{1,S_3^{2-}}}{\partial t} = -\frac{\partial N_{1,S_3^{2-}}}{\partial x} + 2\varepsilon_1 k_f \left(C_{1,S_6^{2-}} - \frac{C_{1,S_3^{\bullet-}}^2}{K_{S3}} \right)$	
$N_{1,i} = -D_{1,i}\frac{\partial C_{1,i}}{\partial x} - z_i \frac{D_{1,i}}{RT} F C_{1,i} \frac{\partial \phi_{1,e}}{\partial x}$	$N_{1,i}\big\|_{x=0} = 0$
$i_s = -\sigma \frac{\partial \phi_s}{\partial x}$	$-\sigma \frac{\partial \phi_s}{\partial x}\Big\|_{x=0} = i_{app}$
$i_{1,e} = F\sum_i z_i N_{1,i}$	$i_{1,e}\big\|_{x=0} = 0$

$$\frac{\partial \varepsilon_{1,k}}{\partial t} = \tilde{V}_k R'_k \qquad N_{1,i}\Big|_{x=l_1} = N_{2,i}\Big|_{x=l_1}$$

$$\frac{\partial \varepsilon_1}{\partial t} = -\sum_k \tilde{V}_k R'_k \qquad -\sigma \frac{\partial \phi_s}{\partial x}\Big|_{x=l_1} = 0$$

Separator (Region 2)

$$\frac{\partial \varepsilon_2 C_{2,i}}{\partial t} = -\frac{\partial N_{2,i}}{\partial x} \qquad N_{2,Li^+}\Big|_{x=l_1+l_2} = \frac{i_{app}}{F}$$

$$\frac{\partial \varepsilon_2 C_{2,S_6^{2-}}}{\partial t} = -\frac{\partial N_{2,S_6^{2-}}}{\partial x} - \varepsilon_2 k_f \left(C_{2,S_6^{2-}} - \frac{C^2_{2,S_3^{\bullet-}}}{K_{S3}} \right) \qquad N_{2,i}\Big|_{x=l_1+l_2} = 0$$

$$\frac{\partial \varepsilon_2 C_{2,S_3^{\bullet-}}}{\partial t} = -\frac{\partial N_{2,S_3^{\bullet-}}}{\partial x} + 2\varepsilon_2 k_f \left(C_{2,S_6^{2-}} - \frac{C^2_{2,S_3^{\bullet-}}}{K_{S3}} \right)$$

$$N_{2,i} = -D_{2,i} \frac{\partial C_{2,i}}{\partial x} - z_i \frac{D_{2,i}}{RT} F C_{2,i} \frac{\partial \phi_{2,e}}{\partial x}$$

$$i_{2,e} = F \sum_i z_i N_{2,i} \qquad i_{1,e}\Big|_{x=l_1} = i_{2,e}\Big|_{x=l_1}$$

$$\frac{\partial \varepsilon_{2,k}}{\partial t} = \tilde{V}_k R'_k \qquad \phi_s\Big|_{x=l_1+l_2} = 0$$

$$\frac{\partial \varepsilon_2}{\partial t} = -\sum_k \tilde{V}_k R'_k \qquad i_{2,e}\Big|_{x=l_1+l_2} = F N_{2,Li^+}$$

Other Expressions

$$r_i = -a \sum_j \frac{s_{i,j} i_j}{n_j F} \qquad a = a_0 \left(\frac{\varepsilon}{\varepsilon_{initial}} \right)^{\xi}$$

$$\frac{\partial i_s}{\partial x} + \frac{\partial i_e}{\partial x} = 0 \qquad \frac{\partial i_e}{\partial x} = a \sum_j i_j$$

$$\eta_j = \phi_s - \phi_e - U_{j,ref} \qquad U_{j,ref} = U_j^{\theta} - \frac{RT}{n_j F} \sum_i s_{ij} \ln \left[\frac{C_i}{1000} \right]$$

$$R_i = \sum_k \gamma_{i,k} R'_k \qquad R'_k = k_k \varepsilon_{1,k} \left(\prod_i C_{1,i}^{\gamma_{i,k}} - K_{sp,k} \right)$$

$$i_j = i_{o,j_{ref}} \left\{ \left(\frac{C_{i,anodic}}{C_{i,ref}} \right)^{s_{a,j}} \exp\left(\frac{\alpha_{a,j} F}{RT} \eta_j \right) - \left(\frac{C_{i,cathodic}}{C_{i,ref}} \right)^{-s_{c,j}} \exp\left(-\frac{\alpha_{c,j} F}{RT} \eta_j \right) \right\}$$

In addition to updating the reaction speciation, the physicochemical parameters have been updated to reflect the latest experimental and modeling literature on high energy density LiS batteries. For example, our group published updated thermodynamic parameters (see Table 2.4 in Chapter 2) so that the high voltages observed in experimental discharge data from a pre-commercial high-energy density LiS pouch cell were adequately reflected in our modeled discharge curves[60]. Therefore, our base case thermodynamic parameters presented here now reproduce voltages seen in state-of-art cells.

Table 3.3. Properties for the Ionic Species.

Species (i)	z_i	D_{i0} (m^2/s)	$C_{i,ref}$ (mol/m^3)
Li^+	+1	1 x 10^{-11}	1033
$S_{8(l)}$	0	1 x 10^{-10}	19.9
S_8^{2-}	-2	6 x 10^{-11}	0.16
S_6^{2-}	-2	6 x 10^{-11}	0.31
S_4^{2-}	-2	1 x 10^{-11}	0.020
S_2^{2-}	-2	1 x 10^{-11}	0.56 x 10^{-6}
S^{2-}	-2	1 x 10^{-11}	0.78 x 10^{-9}
A^-	-1	7 x 10^{-10}	1032
$S_3^{\bullet-}$	-1	1 x 10^{-11}	1 x 10^{-4}

Other parameters used in our base-case simulations have also been qualitatively ground-truthed against experimental observations. For example, the diffusion coefficients from the Kumaresan et. al. model do not adequately reproduce the C-rate dependencies seen in sulfur utilization and capacity experiments and need to be reduced by 1-2 orders of magnitude to observe expected transport limitations at higher rates[10].

Table 3.4. Cathode and Separator Parameters.

Parameter	Cathode	Separator
a_0 (m^2/m^3)	143292	-
$\varepsilon_{initial}$	0.6	0.6
$\varepsilon_{S_{8(s)},initial}$	0.24	1 x 10^{-12}
$\varepsilon_{Li_2S_{(s)},initial}$	1 x 10^{-7}	1 x 10^{-7}
σ	937	-
ξ	1.5	-
T (K)	293	293
b	2.5	2.5

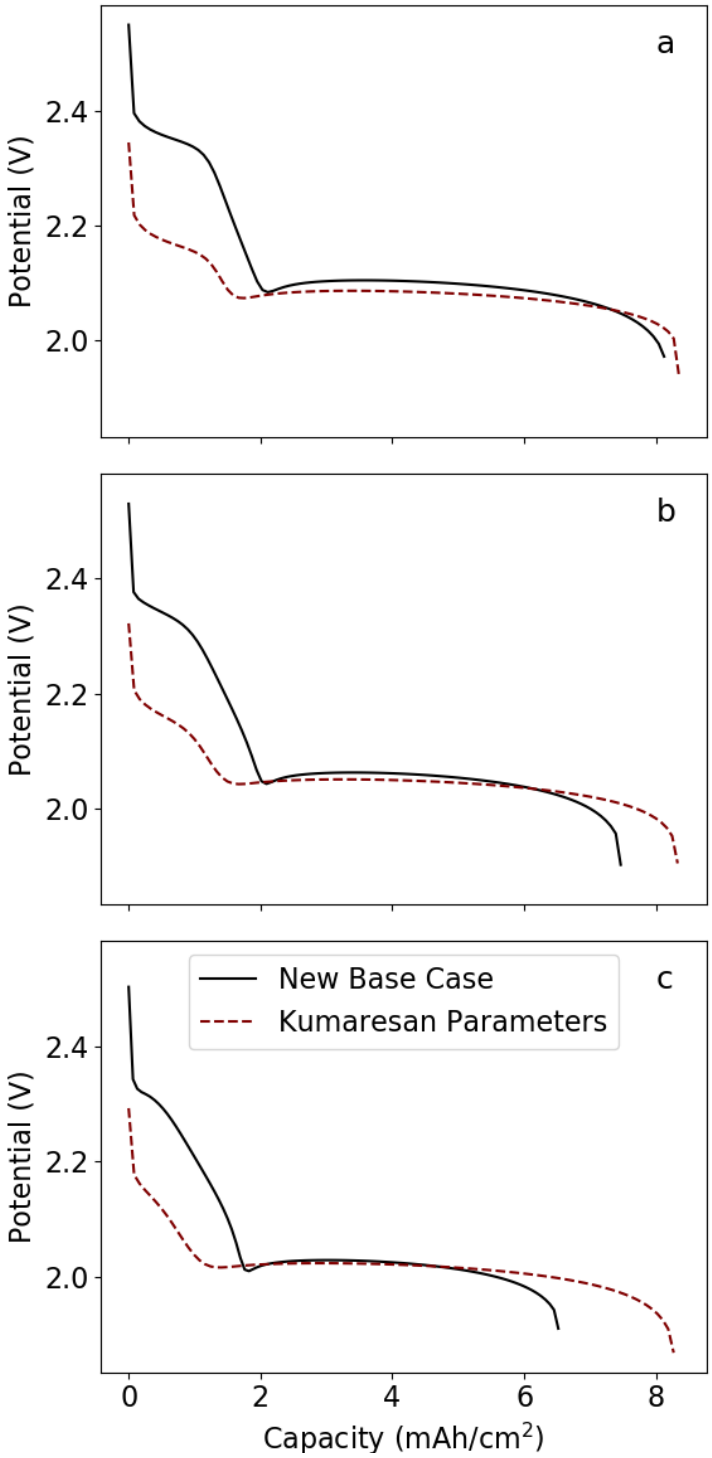

Figure 3.3. Comparison of the new base case parameters (——) developed here and the Kumaresan et. al. parameters (– – –) for the discharge rates (a) 0.2C, (b) 0.5C, and (c) 1.0C. No new dissociation chemistry is considered here (i.e., kf = 0 for the base case).

Our base case transport parameters in Table 3.3 reflect those findings, and also include a diffusion coefficient for the new radical anion species comparable to other shorter-chain polysulfide species. The remaining parameters are reported in Table 3.4 and Table 2.5, and represent values consistent with a high energy density LiS cell.

Figure 3.3 shows pairs of simulated voltage response curves for a high energy density cell using the new experimentally-aligned base case parameters developed here compared to the original values from the Kumaresan et. al. model. Here, base case simulation refers to the original chemical speciation given by Kumaresan et. al., where no radical anion

forms; this is achieved by setting the dissociation rate parameter to $k_f=0$ in Equations (3.3) and (3.4). Figure 3.3 shows that the new base case parameters lead to a longer and higher initial voltage plateau at discharge capacities below 2 mAh/cm^2. In Figure 3.3 (a), the two modeled curves are compared at a low discharge rate of 0.2C, and they have similar final discharge capacities greater than 8 mAh/cm^2 before reaching the end of discharge voltage cut-off. As the C rate is increased to 0.5C (Figure 3.3 (b)) and 1.0C (Figure 3.3 (c)), the total capacity of the battery represented by the new base case parameters declines, matching what is generally observed in the experimental literature for high energy density cells. In contrast, the Kumaresan et. al. curves in Figure 3.3 are aphysically independent of rate, retaining more than 8 mAh/cm^2 of capacity for all discharge rates. In all subsequent analysis, we will use the new base case parameters as we explore the role radical anion chemistry on the discharge behavior of the cell. While the reversible dissociation chemistry represented by Reaction (3.1) and embodied in species balance Equations (3.3) and (3.4) involves no charge transfer, the new radical anion represents a sink for partially reduced sulfur that can impact performance. The dissociation rate parameter k_f has units of inverse seconds, and dictates the timescales over which reversible Reaction (3.1) comes to equilibrium, whereas the equilibrium dissociation constant, K_{S3}, with units of mol/m^3, determines the overall ratio of the two polysulfide species at equilibrium.

Figure 3.4 shows the effect of the equilibrium dissociation constant on the 1C battery discharge curves when the reaction kinetics are fast. Here the kinetics are deemed fast because a 1C discharge takes 3600 s, whereas the time for Reaction (3.1) to achieve equilibrium scales as ~O($1/k_f$), or milliseconds for a rate constant of k_f =1000 s^{-1}. For

comparison, Figure 3.4 (a) also includes the new base case curve from Figure 3.3 (c) (where k_f=0). Figure 3.4 (b) emphasizes the impact of dissociation equilibrium on the discharge curve voltages by showing potential differences between each of the curves with dissociation chemistry and the base case simulation in Figure 3.4 (a). With a value of K_{S3} < 1000 mol/m³, the dissociation equilibrium strongly favors S_6^{2-}, diminishing the role of the radical anion product on the voltage curve. The resulting discharge curve is minimally perturbed when equilibrium favors the same speciation as the base case. However, as K_{S3} increases, reaction equilibrium increasingly favors the formation of radical anion, creating an increasingly concentrated pool of partially reduced sulfur species that is not directly involved in the

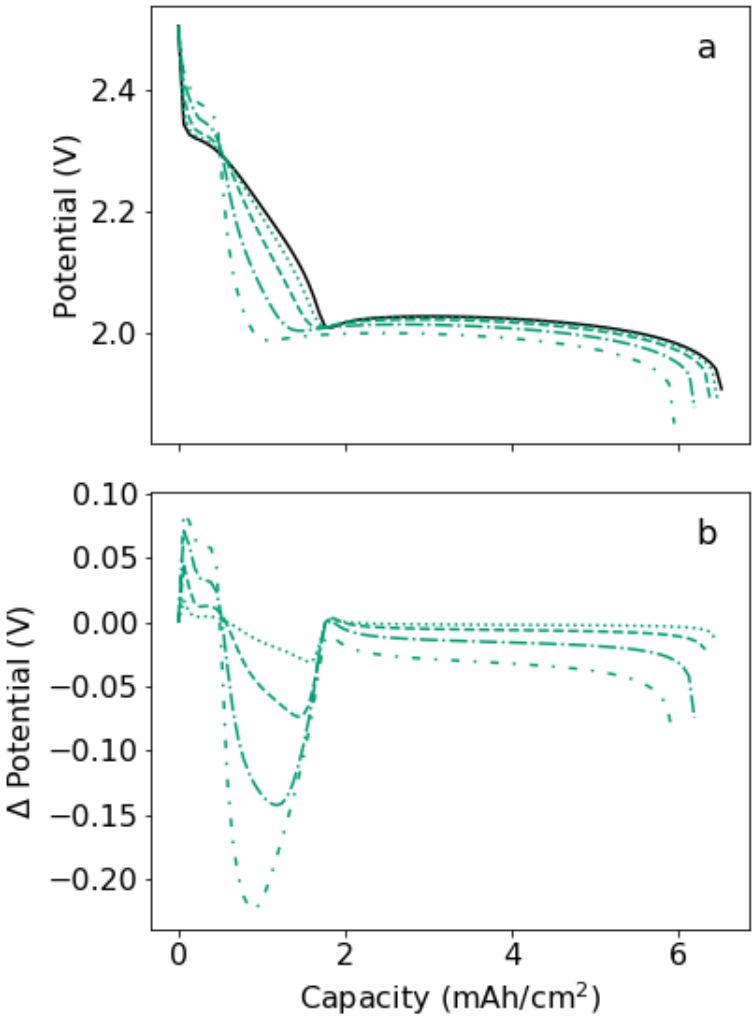

Figure 3.4. (a) The 1C discharge curves for fast dissociation kinetics k_f = 1000 s⁻¹ and increasing equilibrium coefficients K_{S3} = 10³ mol/m³ (• • •), 10⁴ mol/m³ (– – –), 10⁵ mol/m³ (— • — • —), and 10⁶ mol/m³ (- • - • -) are compared to the base case without any dissociation chemistry (k_f = 0, ––––). (b) Potential difference between each fast dissociation discharge curve and

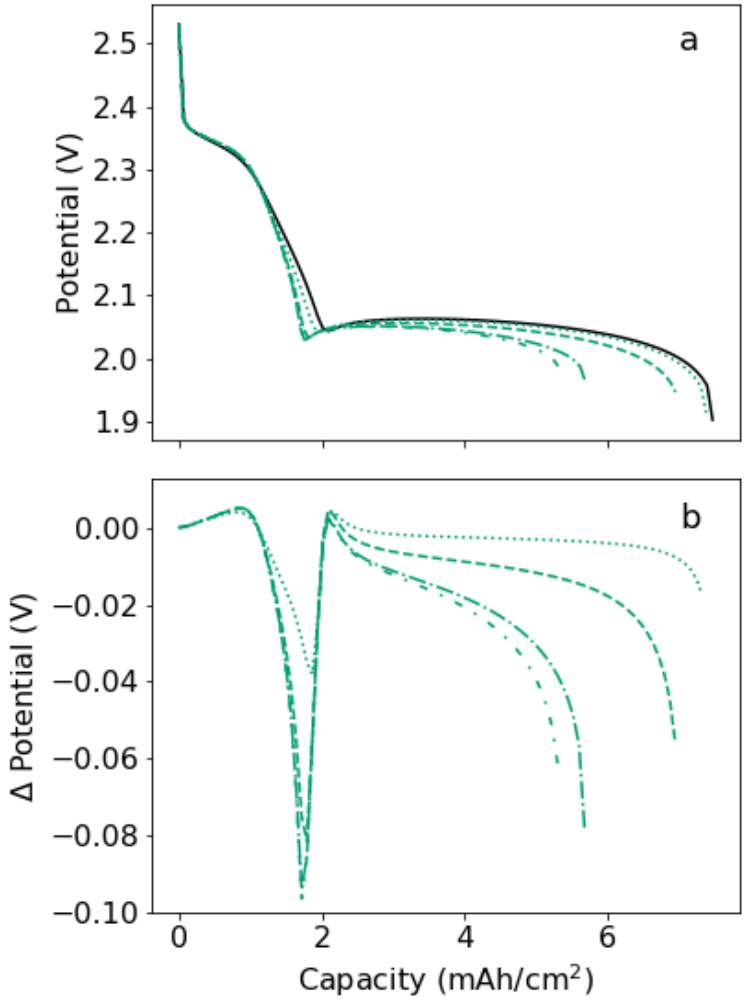

Figure 3.5. (a) The 0.5C discharge curves for slow dissociation kinetics (k_f = 0.001 s^{-1}) and increasing equilibrium coefficients K_{S3} = 10^3 mol/m^3 (• • •), 10^4 mol/m^3 (– – –), 10^5 mol/m^3 (— • — • —), and 10^6 mol/m^3 (- • - • -) are compared to the base case without any dissociation chemistry (k_f = 0, ––––). (b) Potential difference between each slow dissociation discharge curve and the base case.

reduction cascade on the cathode. Once there is a significant pool of radical anion, the reaction cascade is altered. Figure 3.4 (a) shows that the voltage of the first plateau near 2.35 V is enhanced by more than 50 mV as the electrolyte increasing favors partitioning to the radical anion rather than its dimer. This voltage support is followed by an increasing rapid transition to the ~2 V second plateau. During the transition to the second voltage plateau, the voltage deviations away from the base case can be depressed by nearly 200 mV. In Figure 3.4 (b), the transition between enhancing cell voltage (up to discharge capacities of roughly 0.75 mAh/cm^2) and depressing cell voltage (all discharge capacities greater than 0.75 mAh/cm^2) is a marker of the average sulfur redox state of the battery compared to the redox state of the polysulfide species in Reaction (3.1). Specifically, the per sulfur partial charge for both

species in Reaction (3.1) is −0.33. As the battery discharges, the average partial charge progresses from elemental sulfur (0 per sulfur charge) to the final $Li_2S_{(s)}$ discharge product with per sulfur charge of −2. The cell voltage is enhanced in the early stages of discharge when electrolyte speciation is dominated by less-reduced polysulfides than found in Reaction (3.1), and depressed when discharge progresses to more reduced forms of polysulfides.

In terms of electrolyte engineering, a rising K_{S3} value corresponds to an electrolyte that has increasingly better solvation and stabilization of the radical anion $S_3^{\bullet-}$ compared to its dimer anion the S_6^{2-} species. Gupta et. al.[48] identifies two solvents with the characteristic blue optical signature of the $S_3^{\bullet-}$ radical species, N,N-dimethylacetamide (DMA) and dimethyl sulfoxide (DMSO). The stable presence of $S_3^{\bullet-}$ radical implies a high K_{S3} for these electrolytes. Alternately, S_6^{2-} was found to be favored in 1-methylimidazole (MeIm) and a 1:1 by volume mixture of 1,2-dimethoxyethane (DME) and 1,3-dioxolane (DOL) electrolytes (*i.e.*, these electrolytes had low K_{S3}). Likewise, model fits to cyclic voltammetry experiments in DME:DOL electrolyte also produced K_{S3} values that favored S_6^{2-}.formation[62]. Unfortunately, simple molecular descriptors of a solvent such as its donor number, appear inadequate for *a priori* prediction of which polysulfide species will be preferentially solvated[48].

While thermodynamic effects dominated in Figure 3.4, where the kinetics are fast, rather different behavior is seen in Figure 3.5 when we examine 0.5 C discharge with slow dissociation kinetics of $k_f = 0.001\ s^{-1}$. Here, the time constant for the dissociation kinetics is of the order 1000 s, making it comparable to the cell discharge time of 7200 s. In this

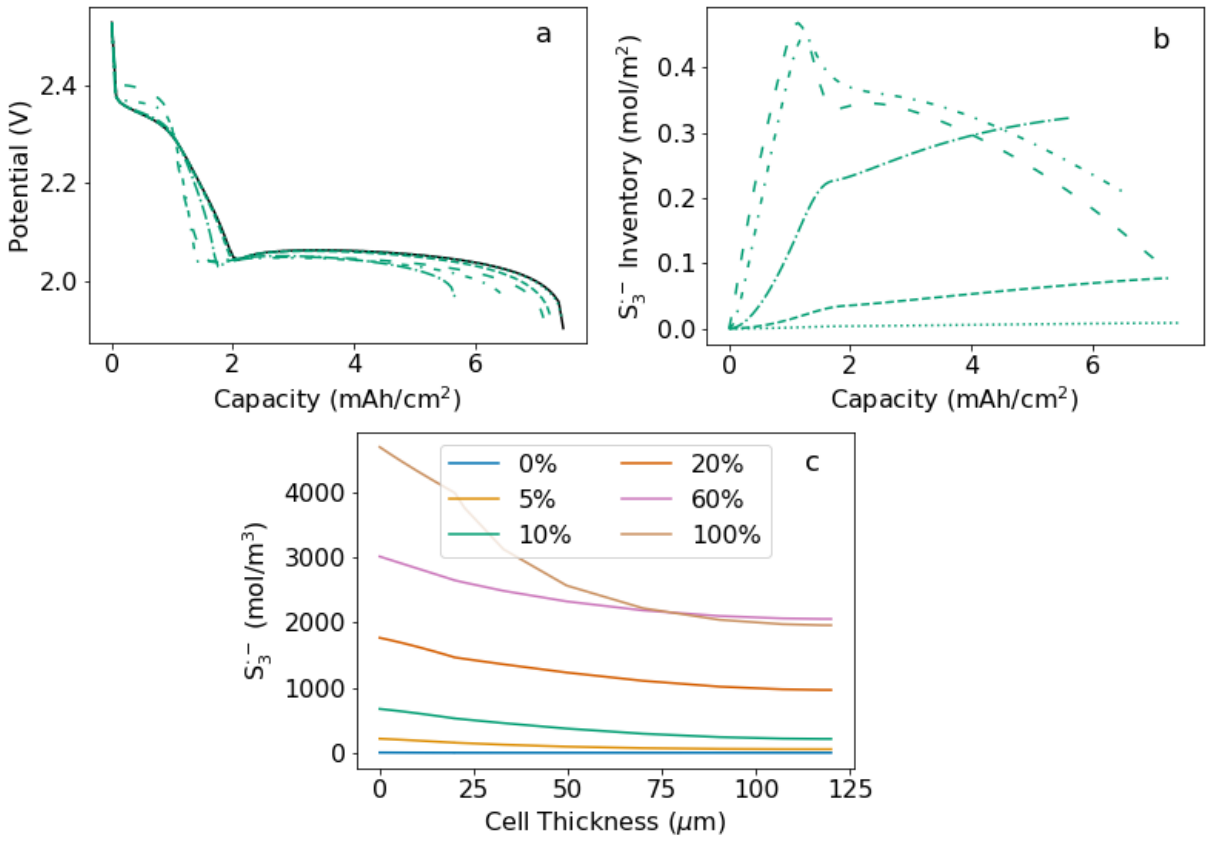

Figure 3.6. (a) Effect of varying the dissociation rate constant k_f on the 0.5C discharge curves when the equilibrium dissociation constant favors the radical anion (K_{S3} = 100,000 mol/m³). (b) Moles of radical anion per unit area of the full cell as a function dissociation rate constants. Curves represent k_f = 0 s⁻¹ (– – –), 10^{-5} s⁻¹ (• • •), 10^{-4} s⁻¹ (– – –), 10^{-3} s⁻¹ (— • — • —), 10^{-2} s⁻¹ (- • - • -), and 10^{-1} s⁻¹ (– – –). (c) Spatial variation of the concentration of the $S_3^{\cdot-}$ radical species at different percentages discharged for k_f = 10^{-3} s⁻¹ and K_{S3} = 100,000 mol/m³.

case, it takes a significant fraction of the discharge before any radical anion can build up via the forward dissociation chemistry of Reaction (3.1). Thus, even when the equilibrium dissociation constant strongly favors the formation of radical anion (e.g., K_{S3} = 10^6 mol/m³), there is no appreciable change to the discharge curve until roughly 1000 s have elapsed, or 1/7th of the capacity has been discharged. Thus, unlike the situation in Figure 3.4, the early discharge voltage is not enhanced in Figure 3.5. However, Figure 3.5 does show appreciable depression of the voltage at longer discharge times (compared to the base case) for large values of K_{S3} where radical anion is favored thermodynamically. This

has a deleterious effect on the extractable energy from the cell. Likewise, the capacity can be appreciably decreased for the slow kinetic case when there is favorable partitioning toward radical anion, as seen in Figure 3.5, owing to lower sulfur utilization when polysulfide inventory gets "stuck" in the slow converting radical anion. Unlike the fast kinetic case, where cell voltage was enhanced at low depth of discharge, slow kinetics at best have little impact and at worst depress voltages and decrease capacity.

Finally, we will consider the effect of a wide range of dissociation rate constants k_f in greater detail when the electrolyte favors partitioning toward the radical anion via a high value of K_{S3} = 100,000 mol/m^3. Figure 3.6 (a) shows a series of 0.5C discharge curves with varying k_f values. With the lowest value of $k_f = 10^{-5}$ s^{-1}, the voltage curve essentially follows the base case (k_f = 0) and there is no inventory of radical anion in the cell over the 7200 second discharge time. As the dissociation kinetics increase, the voltage curve has a higher initial voltage plateau with a steeper slope and earlier transition to the second plateau, mirroring the behavior seen in Figure 3.4.

Figure 3.6 (b) shows the total molar inventory of radical anion from Reaction (3.1) that accumulates in the cell during the 0.5 C discharge (here the total radical anion inventory is given as moles per unit electrode area). Figure 3.6 (b) shows this evolution of the radical anion $S_3^{\bullet -}$ inventory for the same parameters as in Figure 3.6 (a). For each of the simulations with a depressed discharge capacity (compared to the base case), there is significant radical anion $S_3^{\bullet -}$ inventory at the end of the discharge, representing trapped polysulfides that do not participate directly in charge transfer on the electrode. When an electrolyte design stabilizes the radical species, or forms any low reactivity polysulfides, capacity is lost in proportion to the inventory of that species at the end of discharge.

Figure 3.6 (c) shows the spatial variation of the $S_3^{\bullet-}$ radical anion concentration across the separator (from 0 to 20 μm on the spatial axis) and the cathode regions (20-120 μm) when the kinetics are given as $k_f = 10^{-3}$ s^{-1}. The family of curves represent different depths of discharge (shown as % DOD in legend). From the profiles in Figure 3.6 (c), one sees continuous growth in the concentration of radical anion in the separator, whereas the cathode region has growth in radical anion until near the end of discharge, when it is seen to begin getting reconsumed by the back reaction in (3.1). The general shape of the concentration profiles in Figure 3.6 (c) are established very quickly compared to the discharge timescale; after only 5% discharge one sees the highest radical anion concentration is adjacent to the ideally-protected anode (at 0 μm) and the concentration in the cathode is lower. This basic concentration profile persists at all subsequent discharge times. The separator concentration gradient is largely dictated by the no flux condition on the ideally-protected anode, where diffusion and migration must be equal and opposite. Only at discharge times that are short compared to the diffusion timescale across the separator (for DOD <1%, see Figure 3.7 in Supporting Information) does the profile deviate significantly from this shape. The total inventory shown in Figure 3.6 (b) is simply the integral of profiles such as these shown in Figure 3.6 (c). The spatial profiles of several other variables have been included in the Supporting Information, including the S_6^{2-} species profile, the volume fraction of $Li_2S_{(s)}$, and the cathode porosity.

It is interesting to note that the new speciation and assumptions embodied in Reaction (3.1) lead to reversible capacity loss when a highly stable radical anion is generated. Figures 3.4-6 have illuminated the interplay of discharge timescale, reaction timescale, and equilibrium propensity for a species to dissociate through Reaction (3.1).

The experimental timescale explored here was set solely by the discharge C rate, which determined if the reaction timescale (inverse of k_f.) was big or small. Thus, in Figure 3.6, we saw no appreciable change to the discharge curve (Figure 3.6 (a)) and no accumulation of radical anion inventory (Figure 3.6 (b)) over the 7200 s discharge time, when $k_f = 10^{-5}$ s^{-1}. Yet, ultraslow dissociation does not mean unimportant dissociation, especially when considering the aging of a partially discharged cell for days, weeks, or months. In particular, consider a cell partially discharged to 1 mAh/cm^2 with $k_f = 10^{-5}$ s^{-1}. This cell will have negligible radical anion inventory when initially placed into storage (see Figure 3.5 (b)), but over time, the inventory of S_6^{2-} will convert to $S_3^{\bullet-}$ if K_{S3} is large. When pulled from storage, the capacity and rate capability of the cell will have collapsed because so much sulfur inventory is in a stable, unreactive form. This collapse is reversible, but recovery of the active polysulfide is set by the dissociation kinetic timescale and would take a long trickle charge to restore the full capacity.

3.4 Conclusion

In this work, we have presented updated parameters that reflect the ongoing efforts to develop high-energy density lithium sulfur cells. The model suggests that incorporating insights from characterization of electrolyte speciation is required for subsequent LiS battery optimization. Experiments show that solvent choice can dramatically alter the equilibrium ratio of the two polysulfide species in Reaction (3.1)[48], meaning the choice of solvent either stabilizes the $S_3^{\bullet-}$ radical (represented by higher K_{S3} in our model) or the S_6^{2-} anion (lower K_{S3}, here). Likewise, solvent-driven changes in the kinetics of Reaction (3.1) can be associated with a lowering (high k_f) or raising (low k_f) the transition state activations energy. By including a reversible dissociation reaction to produce stable radical anion species seen experimentally, the electrochemical behavior of the cell was significantly changed. The equilibrium dissociation constant K_{S3} and rate constant k_f influenced the timescale and propensity of the system to convert to a less active polysulfide form.

For dissociation timescales on the order of the voltage curve discharge times, the stabilization of radical anion led to decreased overall sulfur utilization since the species is not immediately available for reduction. All of the capacity loss was reversible, but we described storage scenarios and ultraslow conversion kinetics that might look like self-discharge attributed to irreversible reactions with the lithium metal anode. However, all our modeling assumed an ideally-protected anode that excluded any polysulfide reactions or corrosion of lithium, so no irreversible chemistry was possible here. Due to the complexity of this battery chemistry, there are numerous other dissociation and

disproportionation reactions that might be considered for future work, as well as greater attention to the cathode hierarchical structure and imperfections in anode protection, if experimental studies highlight their critical role in the performance of the cell. Here we highlighted a simple reaction involving a well-documented species that had heretofore been excluded in full-cell models, and laid out a clear pathway for closer collaboration between modeling and experimental work.

Finally, this work points to the need for additional attention to quantitative experimental measurements of the solvent-dependent dissociation and disproportionation reaction equilibrium and rate constants in concentrated electrolytes (near the polysulfide solubility limit), as found in low E/S ratio batteries. The growing body of experimental spectroscopy and electroanalytical literature augurs well for battery-relevant quantitation of these parameters in the near future.

3.5 Computational Details

This work extends the standard model developed by Kumaresan et. al.[4], with the polysulfide speciation and reduction cascade we call base case chemistry shown in Figure 3.1. At the lithium anode, there is a constant flux of lithium ions set by the C rate being evaluated. The anode is assumed to be ideally-protected with no side reactions considered and facile lithium cation transport.

Within the macrohomogeneous porous cathode, solid elemental sulfur dissolves to liquid sulfur as $S_{8(l)}$. The sulfur reduction cascade includes the five electrochemical reactions shown in the schematic. The only solid product considered is $Li_2S_{(s)}$ as there is still some debate about the presence of other solid products[10,11,31]. The 1D physics-based model for lithium sulfur batteries incorporates thermodynamics, kinetics of electrochemical and precipitation reactions, transport described by the dilute solution theory, and morphology changes through the time dependence of the volume fractions and the porosities.

The subsequent set of differential algebraic equations (DAE), shown in Table 3.2, was solved in *Maple 2018* with the use of our robust DAE solver approach that combines initialization with DAE simulation as a single step. This uses the semi-implicit Runge Kutta built-in DAE solver called dsolve in implicit mode[71]. The equation set was discretized using orthogonal collocation method with 7 node points for all simulations. Model self-convergence of less than 1% error was calculated using the average error of mid-point values in the cathode at ¾ discharge between simulations with n=7 and n=9. The initial conditions were found with the robust initialization strategy described in a

previous study[32,72]. The computational time for a typical discharge curve is 65 seconds on an AMD Ryzen 7 37000U processor with 16 GB RAM.

3.6 Acknowledgments

The authors would like to thank the Assistant Secretary for Energy Efficiency and Renewable Energy, Office of Vehicle Technologies of the U.S. Department of Energy through the Advanced Battery Materials Research (BMR) Program (Battery500 Consortium) and the Boeing-Sutter Endowment.

3.7 Supporting Information

The plots in Figure 3.7 are taken from the case of k_f = 1x10^{-3} s^{-1} with K_{S3} = 1x10^{-5} at 0.5C. Shown in Figure 3.7, the values of the $S_3^{\cdot-}$ radical species have been plotted at short times, less than 1% of discharge, which translates to between 0 and 50 seconds for 0.5C discharge. The times shown are on the order of the diffusion timescales for the $S_3^{\cdot-}$ species across the separator (40 seconds). The $S_3^{\cdot-}$ radical species is generated within the cathode from the S_6^{2-} species and remain relatively uniform within the cathode at 0.3% discharge. At 0.5% of discharge, there is a gradient within the separator, which is due to the balance of migration and diffusion of the $S_3^{\cdot-}$ species. The migration forces become dominant because the balancing of the flux of the lithium ions and the rest of the polysulfides species, leading to a polysulfide shuttle-like movement of sulfur species to the anode. With the creation of the gradient at the anode, the diffusive forces balance the migration. The S_6^{2-} species is shown in Figure 3.7 (b). Initially, there is no S_6^{2-} species; however, the generation picks up quickly and reaches a maximum at 20% discharge. The S_6^{2-} species participates in the first plateau reduction scheme and therefore is generated early on in discharge and then decreases after about 20%. The $S_3^{\cdot-}$ radical species generation also plays an important part in the time evolution of the S_6^{2-}. With a k_f value of 1x10^{-3} s^{-1}, the dissociation reaction does not reach equilibrium until about a thousand seconds or 20% discharge, the time when the S_6^{2-} reaches a maximum. The S_6^{2-} that is generated after this point is consumed by either the dissociation reaction to $S_3^{\cdot-}$ or the charge transfer reaction to S_4^{2-}. The gradients that develop within the S_6^{2-} species is due to migration as well.

Figure 3.7 (c) shows the spatial variation of the volume fraction of Li_2S. The Li_2S

generation is not significant until there is enough S^{2-} generated, which then quickly precipitates out after reaction with the built-up lithium within the cathode. Due to the gradients from migration of the lithium ions, the maximum Li_2S volume fraction is at the point closest to the separator, and the gradient become more severe at the end of discharge.

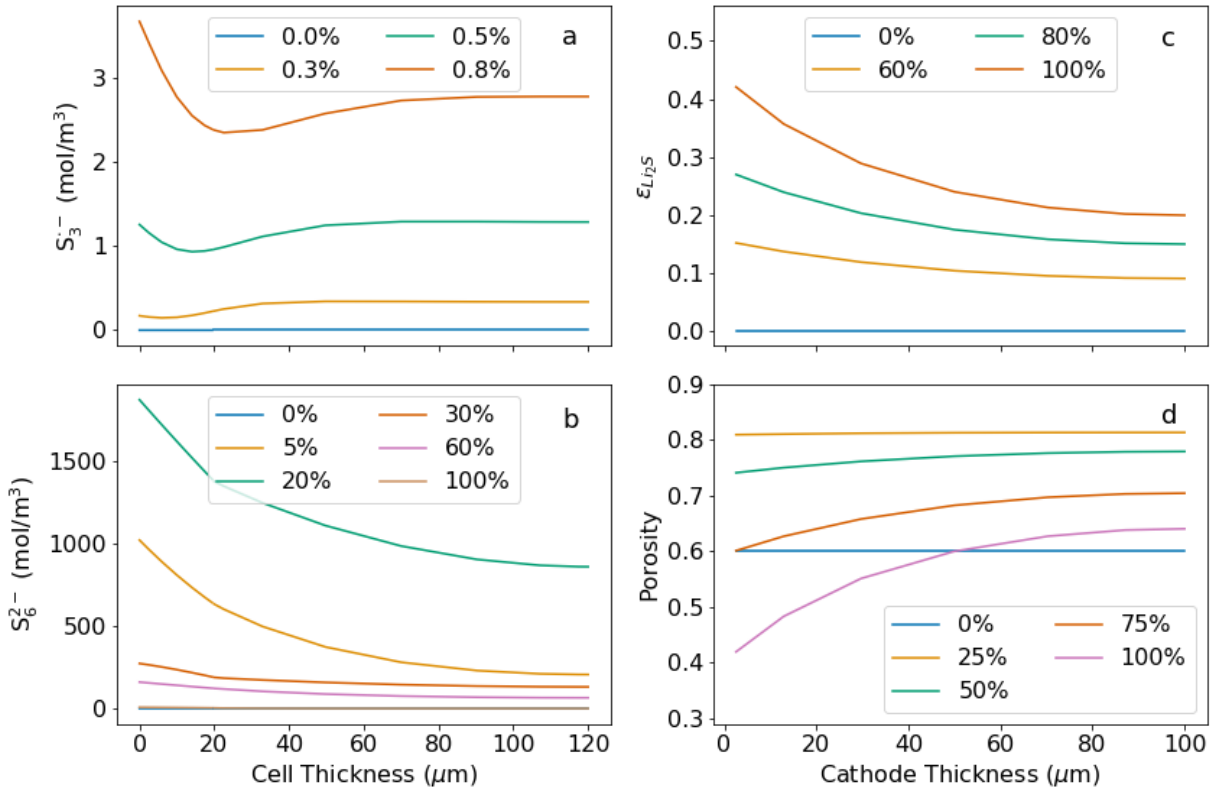

Figure 3.7. Spatial variation of (a) the concentration of the $S_3^{\cdot-}$ radical species, (b) the S_6^{2-} species, (c) the volume fraction of Li_2S, (d) the cathode porosity across the separator (0-20 µm) and the cathode (20-120 µm). The volume fraction of Li_2S and the cathode porosity are only considered within the domain of the cathode (20-120 µm).

The cathode porosity, shown in Figure 3.7 (d), is dictated by the evolution of the two solid species, $S_{8(s)}$ and Li_2S. As the $S_{8(s)}$ species dissolves, the initial gradient of the porosity is caused by the dissolution being faster near the current collector within the cathode. As discharge continues to 50%, the porosity reaches a maximum and levels off

because there is no solid sulfur species. Then, the Li_2S solid species begins to precipitate, and the porosity changes accordingly.

Chapter 4

On the Feasibility of LiS Battery for Aircraft Electric Propulsion

Note: This chapter has been published as a conference proceeding.

R. Hess, R. Arbogast, C. Parke, A. Subramaniam, S. Kolluri and V. Subramanian, *On the Feasibility of a LiS Battery for Aircraft Electric Propulsion*, 2019 AIAA/IEEE Electric Aircraft Technologies Symposium (EATS), Indianapolis, IN, USA, 2019, pp. 1-16, doi: 10.2514/6.2019-4468.

4.1 Nomenclature

A =Area
C =Capacity
C_D =drag coefficient
$^{C}rate_{max}$ = maximum C-rate
$\square T$ =differential temperature
$\square V$ =differential voltage
E =Energy
h =heat transfer coefficient
i =current
$^{i}cell_{max}$ =maximum cell current
K_{gr} =gravimetric packing factor
K_{vo} =volumetric packing factor
N_P =number of cell in parallel
N_S =number of cells in series
P_a =power required for climb
P_{max} =maximum power
P_r =power required for level flight
$Q^{\square}_{cool}$ =heat transfer rate for cooling
$Q^{\square}_{heat}$ =heat transfer rate for heating
R =electrical resistance
R_{cell} =cell electrical resistance
$\square$ =air density
S =wing area
V =voltage, velocity
$^{V}cell_{nom}$ = nominal cell voltage
$^{V}cell_{max}$ = maximum cell voltage
$^{V}pack_{max}$ = maximum pack voltage

V_Z =rate of climb
W =gross vehicle weight
W_{pack} =weight of battery pack

4.2 Introduction

The use of electrified propulsion systems is transforming all sectors of travel. Hybrid-electric and battery electric automobiles have shown a path for efficient, low-carbon transportation. Electric power is a more efficient means to propel vehicles as compared to traditional internal combustion engines and gas turbine engines. As production volumes have increased, the cost of the vehicle propulsion system, including the costs of the batteries have dropped significantly.

Electric aircraft hope to provide the same benefits as those seen in the automotive industry. Increases in the efficiency and power density of the electric motors and the power electronics have reached a level where they are approaching that of modern gas turbine engines. The greatest factor that limits introduction of electric aircraft is the specific energy and energy density of batteries (gravimetric density measured in Wh/kg and volumetric density measured in Wh/l). Though electric propulsion can be more efficient than that of air-breathing engines, the power density of jet fuel or aviation gas greatly exceeds that for current production Lithium (Li) Ion battery chemistries. Jet fuel has a specific energy in excess of 12,000 Wh/kg, while current full rate production Li Ion batteries have specific energies less than 250 Wh/kg. A battery that would provide the same energy as that provided by jet fuel would weigh approximately 48 times as much as the equivalent fuel. Clearly, such systems are not yet practical for long-range transport aircraft. However, there are a number of missions that require less energy and power.

Such missions operate at lower altitudes and for shorter distances. A number of general aviation aircraft can support such mission.

Battery technology is rapidly progressing. New generation chemistries using high-density, solid Lithium anode technology and a conventional cathode (e.g., NMC or nickel manganese cobalt-oxide) promise specific energies in excess of 400 Wh/kg. Another chemistry that is showing promise is Lithium Sulfur (LiS). LiS batteries use conventional Lithium or solid Lithium anode construction, but the active cathode material is Sulfur. Sulfur is lightweight and much less expensive than the materials used in conventional Li Ion cells. Theoretically, it has the ability to achieve specific energies well in excess of 400 Wh/kg.

Conventional Li Ion chemistries exhibit a relatively flat voltage across a large range of operation. This is not true for LiS chemistries. Figure 4.1 shows a comparison of the discharge curves for a LiS cell and a Li Ion cell with a similar operating voltage range (in this case, a Lithium Titanate (LTO) cell is shown). One can see that the discharge voltage is relatively flat across a large portion of the operating range for the Li Ion cell. However,

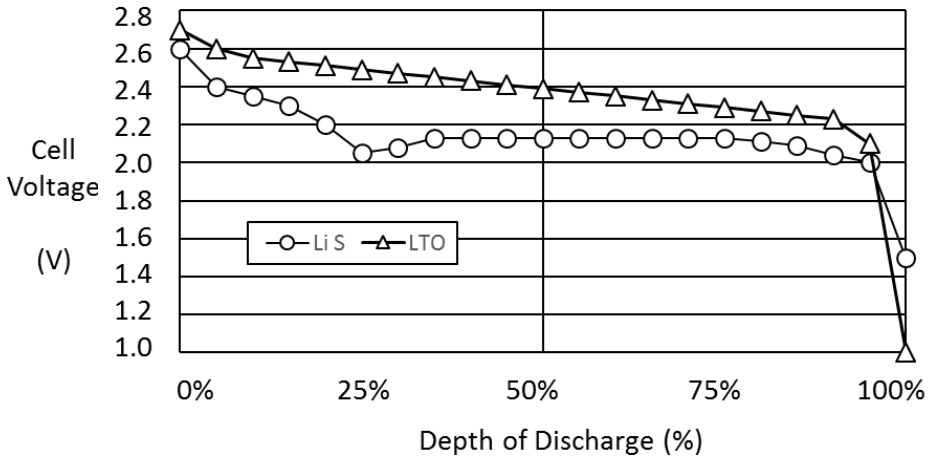

Figure 4.1. Comparison of LiS and Traditional Li Ion (LTO) discharge curves.

the LiS cell exhibits an upper plateau with an average voltage range around 2.3 V and a lower plateau with an average voltage around 2.1 V. This behavior is further described in Section IV. The transition from the upper plateau to the lower plateau presents a challenge for maintaining a smooth discharge profile. It should also be pointed out that the general non-monotonic shape of the LiS discharge profile makes cell management more difficult. This will be described in later sections.

4.3 Current LiS Battery Solutions

LiS cells in various sizes with specific energies over 200 Wh/kg have been available for a number of years in low production volumes. These early generation cells supported relatively low discharge and charge rates[16] as well as low cycle life. Many evolving electric aircraft applications require high C-rate applications and moderate cycle life. There are classes of aircraft, such as high-altitude, long-endurance UAV aircraft, that can operate with low C-rates and for a low number of cycles[73]. Such aircraft have been flown using LiS technology successfully over the last few years. As LiS battery technology has progressed, it may be possible to support more conventional, manned aircraft[74]. Current cell technology supporting moderate (i.e., 2-C) discharge performance and a specific energy in excess of 300 Wh/kg are commercially available. Published data for LiS chemistry is projecting specific energy of 400 Wh/kg by late 2019, with corresponding increase in continuous discharge rates.

4.4 Review of LiS Cell Chemistry

With increasing demand for battery energy and energy density for applications like electric vehicles and electric flight, significant work is being done to look at battery chemistries that will be able to go beyond the current limitations of conventional lithium ion technology. Lithium sulfur chemistry has a theoretical energy density of around 2600 Wh/kg, with a future practical value of around 800 Wh/kg, around three times as energy dense as current Li Ion technology[75].

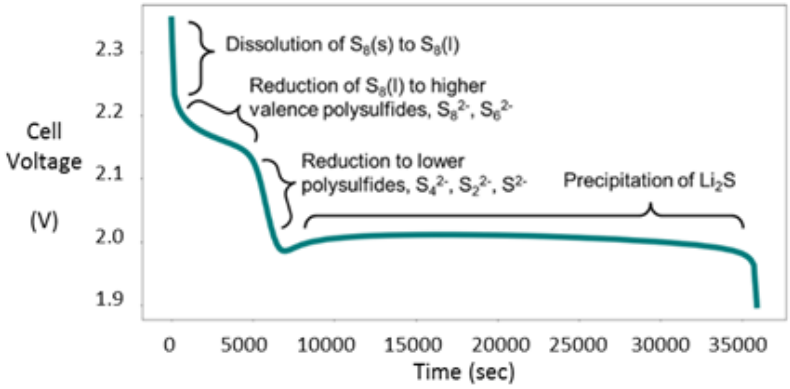

Figure 4.2. Typical Lithium Sulfur Discharge Profile

Lithium sulfur batteries utilize a lithium metal anode and a sulfur/carbon composite cathode. The lithium metal anode presents many challenges on its own because lithium metal is highly reactive and unstructured. Within LiS cells, the active cathode material is solid sulfur, which is inherently insulating, and because of this, carbon is added to the cathode for increased conductivity, which can reduce the energy density. As the battery discharges (as shown in Figure 4.2), the sulfur material undergoes a complex set of reactions. The initial source of sulfur is amorphous solid S_8, which dissolves to liquid S_8. The charge transfer reactions then begin with the reduction of liquid sulfur (gaining electrons) and becoming charged. The charged sulfur species (S_n^{2-}, n = 2, 4, 6, 8) are collectively known as polysulfides. The final process in discharge is the precipitation of Li_2S that corresponds to the long plateau around 2.1 V that makes up the majority of

the capacity. As the reduction of sulfur proceeds via complicated multi-step mechanism, a variety of intermediate polysulfides of the general formula Li_2S_n are formed. The polarity of those sulfur compounds varies widely with sulfur being non-polar and Li_2S, the terminal species, being polar. The polysulfides are of intermediate polarity and often quite well soluble in the electrolyte. Because the polysulfide species are soluble in the electrolyte, they can easily travel between the cathode and the anode along with the lithium ions. Instead of useful oxidation and reduction cycles, parasitic reduction and oxidation reactions of the intermediate polysulfides occur, depleting the active material of both the cathode and the anode. This yields a reduction in capacity and results in the battery voltage moving to the resting voltage, even when the battery is not being discharged. Due to these complexities, this chemistry is much more complex than traditional Li Ion chemistry.

4.5 Reference Platform

As an assessment of the suitability of LiS chemistry for electric aircraft propulsion, a study of the performance of current LiS cells to meet the size, weight and power (SWaP) needs for a general aviation application was undertaken. In this study, a model of a Cessna Caravan 208B (see Figure 4.3) is fitted with a LiS battery pack in the cargo pod and the existing gas turbine engine is to be replaced with an electric motor / motor controller. This form of conversion has been previously proposed[76,77]. However, the focus in this assessment is specifically to evaluate the ability of a LiS-based battery for such an application.

In this study, we assume the weight of the aircraft (less battery system) with 2 passengers is 2325 kg (5115 lbs). We allocate 1213 kg (2669 lbs) for the battery system. The aircraft uses a single 3-bladed propeller with a diameter of 2.591 m (8.5 ft).

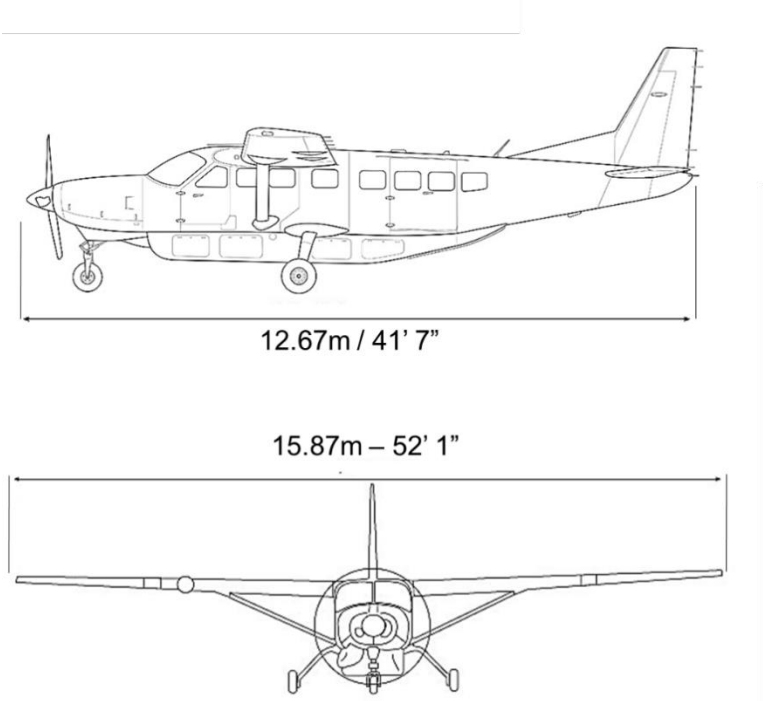

Figure 4.3. Reference Aircraft – Cessna Caravan 208B Super Cargomaster EX.

4.6 Reference Flight Profile (BAE)

A reference flight profile was established which consisted of a 5 m/s rate of climb upon takeoff to an altitude of 3000 m (9842 ft). The aircraft would cruise at 130 kts (66.9 m/s), for a range of 225 km (140 mile) and then descend and land.

With knowledge of the aircraft weight (W), which includes the passengers and battery, the cruise speed (V), the rate-of-climb (Vz), and drag coefficient (C_D) we can compute the power for level flight (P_r) and the power required for climb (P_a) from the equations:

$$P_r = \tfrac{1}{2}\rho S V_z^3 C_D \tag{4.1}$$

$$V_z = \left(P_a - P_r\right)/W \tag{4.2}$$

$$P_a = V_z W + P_r \tag{4.3}$$

The resulting discharge power profile for the battery based on the flight / propulsion requirements is presented in Table 4.1. Note that power for flight electronics, etc. are also included in the overall power demands.

Table 4.1. Preliminary Vehicle Power Demand by Flight Phase / Time

Flight Phase	Duration (minutes)	Power (kW)
Standing (STD)	5	5.0
Taxi (TXI)	5	45.2
Takeoff (TOF)	1	345.0
Climb (CLI)	9	345.0
Cruise (ENR)	60	148.4
Descent (DSC)	10	112.5
Landing (LND)	5	120.0
Taxi (TXI)	5	45.2
Standing (STD)	5	5.0

The total energy that the pack needs to discharge is 213 kWh. We include an additional 20% increase in capacity, resulting in total required energy capacity of 257 kWh.

4.7 Battery Pack Sizing

Battery packs are constructed from a number of cells arranged in a lattice. The overall voltage of the pack is achieved by the number of cells in connected in series, while the power and energy capability are achieved by the total number of cell arranged in parallel strings. Once the pack topology (the number of series cells (N_S) and parallel cells (N_P)) is established, the pack is evaluated for performance. Once a suitable number of cells is determined, the heat load, pack size and pack weight are determined. As the battery pack is discharged, the pack energy will decrease. This is manifested in an overall reduction in pack voltage. Note that the act of discharging causes an ohmic reduction (i.e., $\Delta V = i \times R$) of the voltage at the battery pack terminals. We further assume that the output voltage should not drop below some specified value to allow the motor controllers and power converters to operate in their nominal range. For the purpose of the study, we assume the maximum pack voltage is 800 V and the minimum pack voltage is 600 V.

In this study, the pack topology was used to scale the power demands that would be seen by a single cell. Actual cells were tested against the scaled profile to characterize ability of the cells to generate the requisite power. This test data was then used to develop a physics-based model of the cell. Once that model is formulated, differing flight profiles could be evaluated to understand system performance.

The selected cell has a maximum voltage (i.e., fully charged) of 2.6 V. The selected cells have a capacity (C) of 19.5 Ah and are rated for a continuous discharge of 39 A (a 2-C rate). The nominal voltage ($^{V}cell_{nom}$) is 2.1 V and the cell has a cutoff voltage of 1.9 V. It is critical keep the cell terminal voltages above the cutoff voltage to minimize damage to

the cell.

The number of cells in series (N_S) to make the maximum pack voltage is calculated from the equation:

$$N_S = \frac{V_{pack,\max}}{V_{cell,\max}} = \frac{800}{2.6} = 308 \qquad (4.4)$$

The minimum number of cells is parallel (NP) is calculated from the required energy from the equation:

$$N_P = \frac{E}{V_{cell,nom} C N_S} = \frac{257000\ Wh}{2.1\ V\ x\ 19.5\ Ah\ x\ 308} = 20 \qquad (4.5)$$

An alternate way to determine N_P is to look at the maximum power rating and the maximum cell discharge rate. This alternate formula for N_P is given by:

$$N_P = \frac{P_{max}}{N_S V_{cell,nom} C_{Crate,\max}} = 484000\ W / \left(308\ x\ 2.1V\ x\ 19.5\ Ah\ x\ 2/h\right) = 19 \qquad (4.6)$$

From a weight perspective, we can also calculate the number of cells using a gravimetric packing factor, the weight of the cells, and the weight of the battery pack. We assume a packing factor of 1.3[1]. The number of cells in parallel is then computed from

$$N_P = \frac{W_{pack}}{N_S W_{cell} K_{gr}} = \frac{1214\ kg}{308\ x\ 0.1365\ kg\ x\ 1.3} = 22 \qquad (4.7)$$

We want to maximize total energy, so we use 22 cells in parallel. This results in a battery pack with a total energy capacity of 277.4 kWh.

Not only do we want to understand if a LiS battery pack can provide the power for electric propulsion, but we need to assess the weight and volume requirements of such

[1] Typical ranges can be from 1.2 to 1.7.

battery systems. In this study, we assume a gravimetric packing factor of 1.3, resulting in a pack that would weigh approximately 1214 kg. The design must also look at volumetric packing factor. This is a function of the cell volume along with the cell-to-cell arrangement. The cell-to-cell arrangement is primarily influenced by the cooling approach. Two cooling approaches were considered:

- Forced airflow over the cells. The cells are fixed in frames that allow air to flow between the cells (see Figure 4.4 (a)).
- Forced air through heatsink fins mounted on the cell. The cells are sandwiched together with metal heatsink fins. Air is forced through the heatsink fins (see Figure 4.4 (b)).

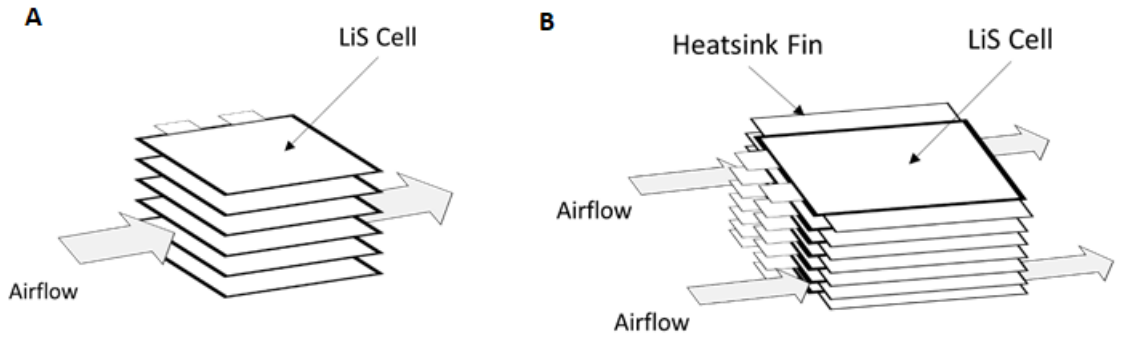

Figure 4.4. General Cell Arrangement for (a) Forced Air Cooling between Cells and (b) Forced Air Cooling through Heatsink Fins.

A thermal analysis looked at the balance between the cell ohmic heating and the forced air cooling approach. The heat balance can be expressed as the condition where the heating is negated by the cooling:

$$\dot{Q}_{heat} = \dot{Q}_{cool} \tag{4.8}$$

This equality can be expressed as

$$i_{cell,\max}^2 R_{cell} = hA\Delta T \quad (4.9)$$

Where h is the characteristic surface area for each approach (based on cell area or heatsink fin area) and flowrate, while ΔT is the temperature differential between the cooling air and the cell steady-state temperature.

Table 4.2. Comparison of Pack Volumes.

Cooling Approach	Pack Volume (m^3)	Required Cooling Airflow (cfm)
Air Blown between Cells	3.57	501
Air Blown through Heatsink Fins	3.52	1421

The size of the heat exchanger fins, cell-to-cell spacing and airflow were all varied to ensure that the cooling solution would be able to provide sufficient cooling to maintain the cell temperature. The differing fin geometries and cell spacing details along with the cell volume information is then used to calculate the pack volume.

We assumed that the battery pack would need to fit in an underbelly cargo pod with a volume of 4 m^3. The subsequent pack geometries are presented in Table 4.2. Though the use of heatsink fins has slightly better packing efficiency than the pack that uses cooling air blown over the cells, the approach requires significantly greater airflow as it has less overall surface area for heat transfer. This increased airflow would require a larger cooling system design.

4.8 LiS Pack Performance

Though the basic sizing analysis would indicate we have sufficient energy in the pack, we need to ensure that the overall pack voltage stays above the pack minimum (600 V) and that the cell voltages do not drop below the cell cutoff voltage (1.9 V). A simplified stepwise simulation was run which used the power discharge profile to determine the cell and pack

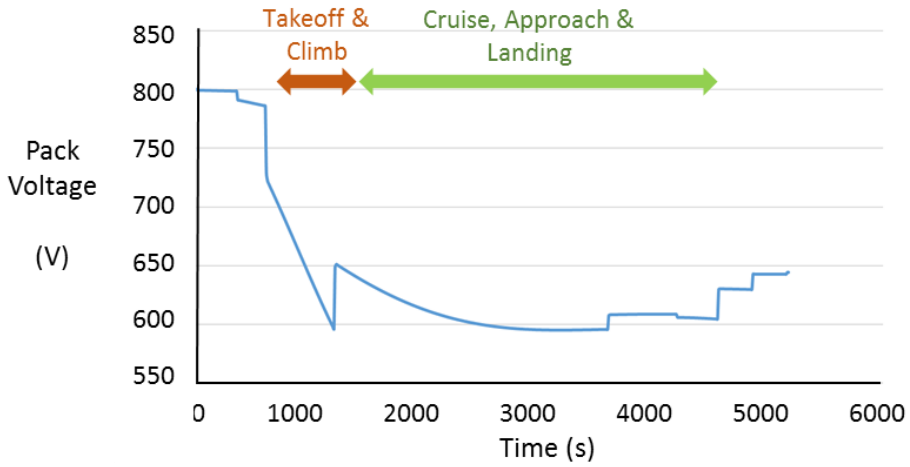

Figure 4.5. Estimated Pack Voltage during Flight.

voltages. This simulation assumed constant pack temperature and cell impedance that varied with state-of-charge. This is presented in Figure 4.5.

From the analysis, we see that the minimum pack voltage stays near 600 V and inspection of the cell voltage shows the minimum cell voltage is 1.93 V. This analysis assumes a cell impedance changes with state-of-charge (SoC) and does not assess the degradation of cell performance as the cells are cycled and aged. A more thorough analysis is required to understand the behavior of the LiS cells for this application, particularly at the end of the climb phase and toward the end of the cruise flight segment where the pack is at greatest risk of dropping below the minimum cell voltage.

Cell-level testing was completed to assess the performance of the cell. The power profile was scaled to that for a single cell and was used as discharge load. As was noted in simplified analysis in Figure 4.5, the pack (and correspondingly each cell) was close to hitting the voltage threshold. Actual test measurements confirmed this behavior, with the

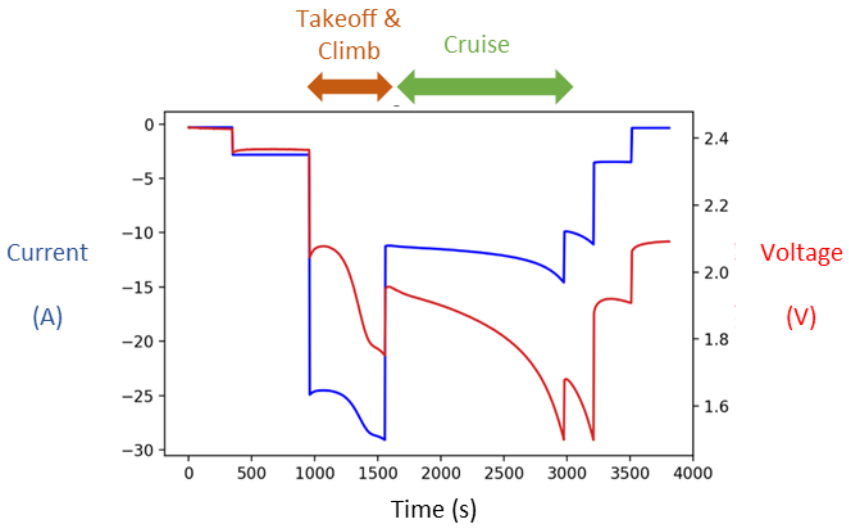

Figure 4.6. Measured Flight Profile Comparison (Cell).

cell voltages near or below the cell cutoff voltage at the end of the climb and towards the end of the cruise phase. The test data are presented in Figure 4.6. The jagged shape of the voltage profile at a time of 3000 seconds is a result of the battery cycler folding back when the cell voltage dropped below 1.5 V. At this point, the effective pack voltage would have been well under 600 V. The remainder of the cruise flight-phase test protocol was suspended and the approach and landing profiles were executed.

A more detailed understanding of the cell behavior is required to understand the rapid drop in cell voltage during the cruise phase.

4.9 LiS Modeling

Many different models have been developed for the study of lithium sulfur batteries at the cell level. These models are generally empirical, equivalent circuit models, 0-dimendional electrochemical engineering models, or 1-dimensional (1D) electrochemical engineering models. The empirical models are based on large collections of data and predict behavior based on measured the current/voltage responses. Equivalent circuit models (such as used for the initial analysis presented in Figure 4.5) assume that batteries can be represented as a combination of simple circuit elements. Electrochemical engineering models are based on electrochemical physics that describe how voltage, current, and the species interplay under different operating conditions. Zero dimensional models are also referred to as lumped models because they do not include spatial variations of variables. The one-dimensional models describe how chemical species move throughout the regions of the battery.

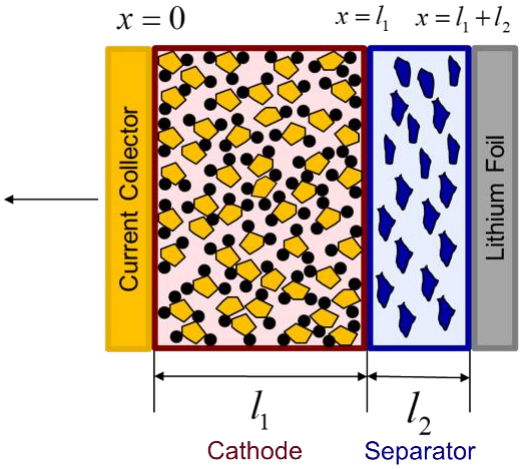

Figure 4.7. Schematic of Lithium Sulfur Battery.

In this study, a 1D mathematical model for Lithium Sulfur batteries was formulated and used to predict the performance of the battery. A schematic of the model

is shown in Figure 4.7.

The cathode is shown in red with yellow amorphous solid sulfur and conductive carbon particles in black. The separator is the blue section and represents a porous separator filled with electrolyte. As the battery discharges, lithium metal oxidizes to lithium ions while the electrons do work on an outside load that is connected to the battery. The lithium ions travel through the separator into the cathode. The solid sulfur dissolves into liquid sulfur, which is reduced through several electrochemical reactions until the S^{2-} reacts with the lithium ions to form the precipitate, Li_2S. This discharge model was developed by Kumaresan et. al.[4] and includes transport, kinetic, and thermodynamic effects. The model accounts for concentration changes in time and position for eight liquid species and two solid species. The material balance for each specie is included and accounts for charge transfer reactions (gaining or losing electrons or charge) and precipitation reactions. The species flux is described by the Nernst Planck relation, which is due to either diffusion or migration in this model. Diffusion is the motion due to concentration gradients while migration is caused by electric field potentials and depends on both the charge and concentration of the specie and the potential gradient.

Due to the presence of precipitation reactions that affect the morphology of the cathode, the effective diffusion changes during discharge. To account for this, the model tracks the porosity, volume fractions, and specific surface area as they change with time. The specific surface area where the electrochemical reactions take place is a function of the changing porosity. For precipitation reactions, the volume fraction of the solid specie is dependent on the concentration of the liquid precursors and the solubility constant.

The change in porosity is calculated by considering how the volume fractions change.

In electrochemical systems, the current for a reaction is the rate at which that reaction is taking place. In the Kumaresan model, like many other models, the kinetics of the system is described by the Butler Volmer equation, an exponential expression that depends on concentration of the species involved and the overpotential. Overpotential is a concept in

Table 4.3. Estimated Parameters.

Thermodynamic, Kinetic and Transport Parameters	Design Parameters
Diffusivities (8)	Initial Concentrations (7) and Volume Fractions (2)
K_{sp} of S_8(s) and Li_2S	Region Lengths
Exchange Current Densities (6)	Filler Fractions
Contact Resistance	Surface to Volume Ratio
Conductivity	Capacity

electrochemistry that essentially relates to how efficient the overall cell is at driving a certain reaction. Ohm's Law describes how the solid phase potential changes with position. The model also enforces charge conservation. The model results in a large system of nonlinear equations that is nontrivial to initialize correctly and solve efficiently. The model was written and solved in MAPLE.

4.10 LiS Modeling Results

To assist in understanding the performance of lithium sulfur batteries under flight conditions, low-rate production Lithium Sulfur Pouch Cells were characterized and use to develop the 1D electrochemical model. The key model parameters are detailed in Table 3. The power of this model is the insight it provides into the cell behavior.

For an accurate prediction, the model parameters need to be adjusted to meet the performance of the specific cells being used. Estimation techniques were used to estimate

the various parameters and states in the model. The measurements used in the estimator consist of the cell voltage and current. The measurements were collected for constant charge / discharge conditions. The current draw is defined, and the voltage response is measured. The difference between the experimental voltage output and the model voltage predictions were minimized in the estimator. The experiments were performed at 20°C and for a number of C-rates (0.1 C to 2 C). A large number of cells were tested to help isolate the effects of capacity fade.

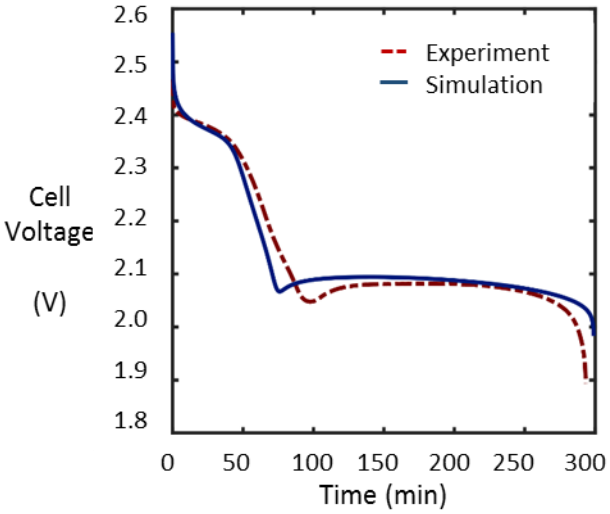

Figure 4.8. Comparison of Measured and Simulated LiS Cell Discharge at 0.1 C.

Sample results are shown in Figure 4.8. The model predicts the battery behavior very well for simple discharge scenarios.

Testing at the cell and pack level can be costly and can pose safety risks if the cell behavior is not well understood. The benefit of the electrochemical model is that it can be used to study the behavior of differing pack topologies to various discharge profiles. Both steady state and transient behavior can be assessed. The comparison between the model predictions and the initial flight profile from the experiment are included in Figure 4.9. The model predicts the trends in the voltage response well. For the flight profile, the average error between the model and experiment is 2.5 mV.

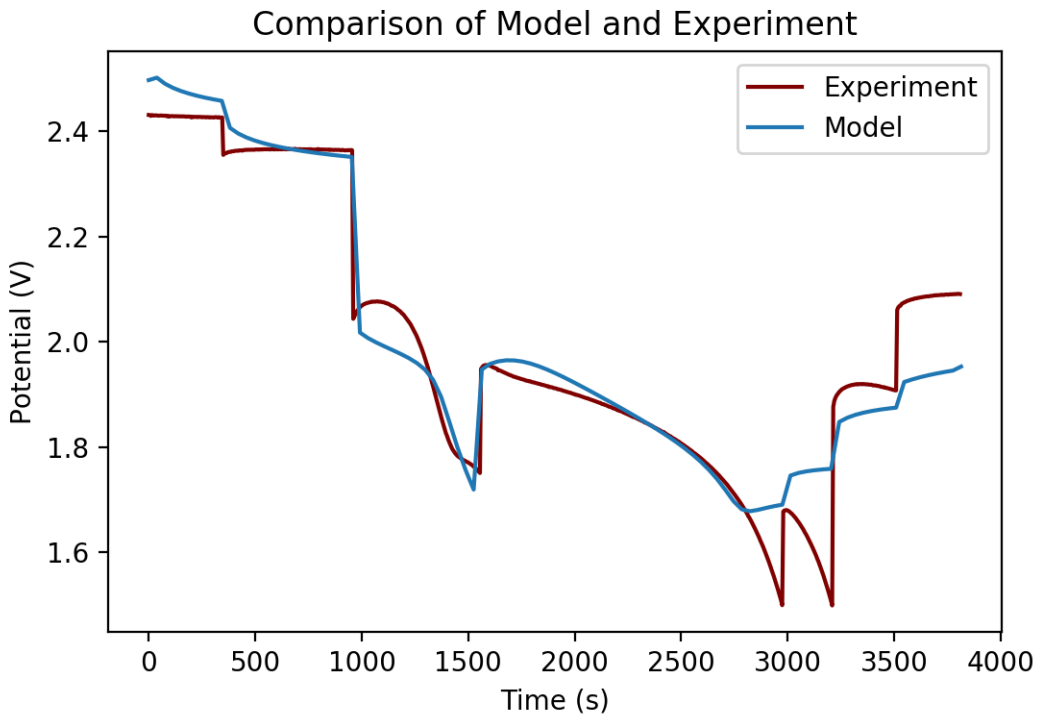

Figure 4.9. Measured versus Predicted Flight Profile Using Advanced Model (Cell).

Analysis of the parameters in the resulting model indicated that Li ion concentration that accumulates in the cathode during discharge (and the related cathode porosity) were significantly decreased at higher C-rates. This corresponds to a significant decrease in conductivity (i.e., an increase in electrical resistance) under high discharge conditions. This behavior occurs in conventional Li Ion chemistries, though the magnitude of the effect appears much higher for the LiS chemistry that was studied in this work. Though the initial model assumed a variation in cell impedance as a function of SoC, the substantial increase of impedance with C-rate was not initially understood.

4.11 LiS Pack Management

All high-capacity batteries require some form of battery management system (BMS). The BMS is an electronic system that manages cell or battery pack behavior, such as by

protecting the battery from operating outside its safe operating voltage, current and temperature areas, monitoring cell and battery state, performing precharge and balancing operations, calculating and logging state information and communicating with other vehicle subsystems. One of the key functions is state-of-charge (SoC) calculation. For traditional Li Ion cells, this can be accomplished by measuring the voltage of the pack when there is no current (i.e., the open circuit voltage). The SoC is then directly calculated from the open circuit voltage. However, the non-monotonic nature of the LiS voltage / SoC curve is such that the SoC cannot be directly computed from the open circuit voltage, as there are multiple SoCs for a specific open circuit voltage. This is further complicated by the effect of the polysulfide shuttle behavior within the lower voltage plateau. If the battery was allowed to rest, the cell voltage will move to the nominal resting voltage. Simple voltage measurements are not useful for understanding the remaining capacity in the LiS battery pack. One of the benefits of the advanced 1D electrochemical modeling approach is that it can be programmed into the BMS and used to estimate the pack SoC and that information can be maintained in computer memory for monitoring and to assist in managing charge and discharge operations.

4.12 Impact of Future LiS Cell Performance

As noted in the simulation and the cell testing, the pack as envisioned was not able to complete the cruise phase due to the large drop in cell voltage (and resulting loss of pack voltage) midway through the flight. Deeper analysis of the model and the test data indicates that the cell was seeing increased impedance because during high C-rate operations and the general increase in cell impedance at lower SoCs as the cell is discharged. Though the pack was designed to have a 20% contingency in energy, this energy is not available. The sudden drop in the cell voltage was occurring at moderate C-rates (0.6) and at 50% SoC. Analysis of the data indicated that at the cell impedance has doubled at 50% SoC compared to the impedance at the beginning of the flight (100% SoC).

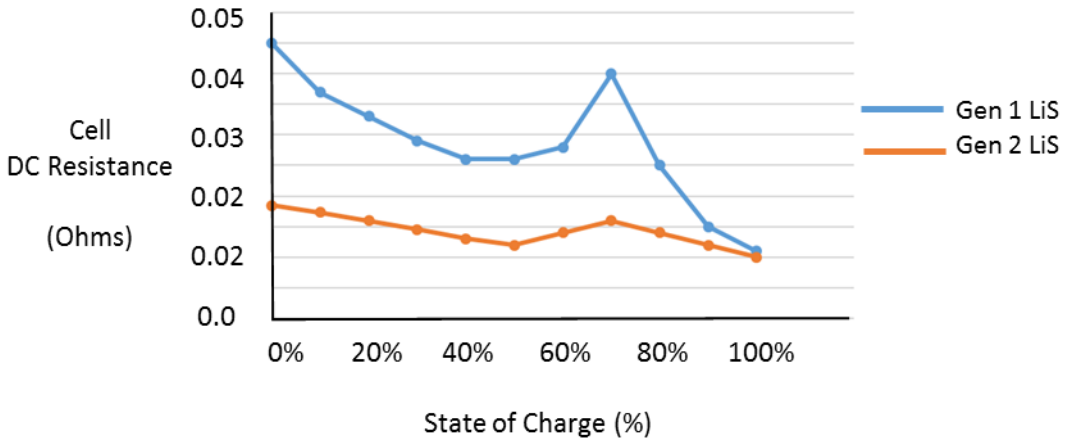

Figure 4.10. Comparison of Cell Resistance (Current LiS Cell and Next Generation LiS Cell).

Though the cell open circuit voltage is around 2.1 V, the effective ohmic (i.e., i x R) drop at this condition is greater than 0.3 V. This condition is forcing the cell to drop below its cutoff voltage. Not only does this result in reduced range, but the ability of the system to provide sufficient power during an aborted landing for a climb is greatly compromised.

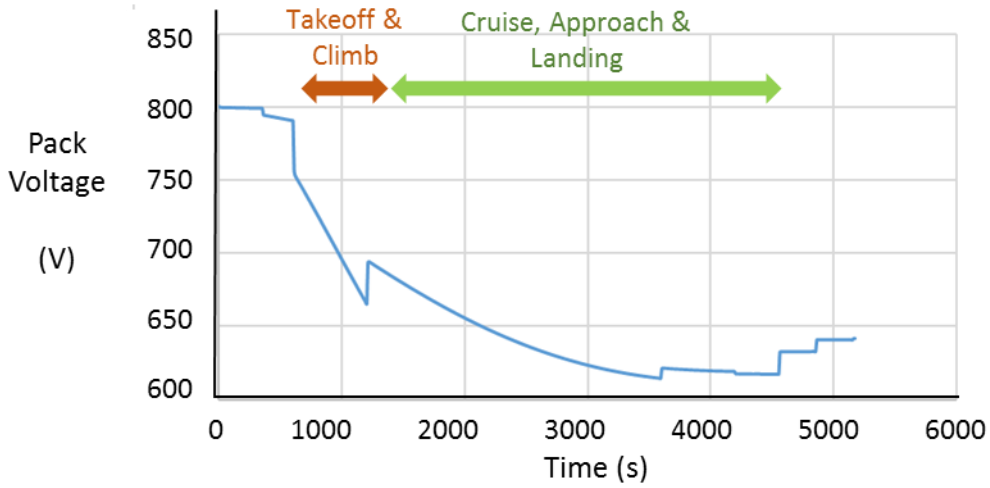

Figure 4.11. Simulated Pack Voltage for Flight Profile using Next Generation LiS Cells.

For this study, a cell with a specific energy of 300 Wh/kg was analyzed and tested. Higher density LiS cell technology is being commercialized with specific energies in excess of 400 Wh/kg. Not only are the next generation LiS cells realizing greater specific energies, but are also exhibiting lower impedance. A comparison of the cell impedance for the current generation cell and a new generation of cells is shown in Figure 4.10. As can be seen, the cell impedance in the next generation LiS chemistries are less impacted by SoC. A simulation using such cells was performed to assess the level of voltage margin that would be afforded. A simulation (presented in Figure 4.11) using data from the latest 400 Wh/kg cell showed the cell voltages stayed well above cell cutoff voltage during the flight profile. Further study and characterization of next generation LiS cells is needed to fully assess them for this application.

The primary purpose of this research was to understand the basic sizing of a LiS battery for an electric aircraft application. Though a battery of sufficient energy and power could be developed to meet the size and weight requirements, the design was affected by increases in cell impedance during the operation. It is known that cell impedance also increases with increased usage. Similarly, cell capacity also decreases with increased usage. The analysis presented herein focused on beginning-of-life (BOL) performance. Specific testing of the system to establish performance at end-of-life (EOL) was not completed, but testing was done as part of the characterization to assess capacity fade as a function of cell charge / discharge cycling. This is shown in Figure 4.12. As in evidenced by this figure, the cell studied in the research exhibited significant capacity fade in a relatively few cycles. This is a less aggressive cycle than is proposed for the general aviation problem studied in this research.

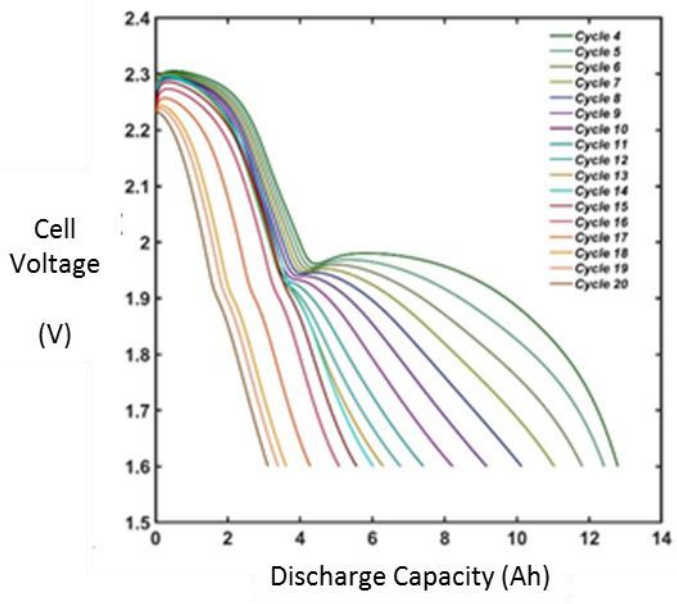

Figure 4.12. Cell Capacity as a Function of Charge / Discharge Cycle (C/2 Discharge).

4.13 Conclusions

A concept for using a LiS battery to provide electric power for a general aviation aircraft was studied. Initial sizing analysis indicated that such a pack would be able to achieve the weight and volume claims for electric flight, but the design was limited in range owing to the inability to maintain the pack voltage within the prescribe voltage range. Several key findings were noted:

- Though LiS chemistry has sufficient energy density for the proposed application, the increase of cell impedance as SoC decreases and for high discharge rates can result in significant cell and pack-level voltage drop during discharge, limiting the usable pack capacity and performance.
- Advanced 1D electrochemical modeling could be applied to LiS cell chemistry.
- Use of the advanced 1D electrochemical modeling provided deep insights into the behavior of the cell operation.
- LiS chemistries are more challenging for cell management and pack design due to the non-monotonic nature of their voltage / SoC curves.
- Current LiS cells have limited cycle life, particularly for higher C-rate discharge applications. This limits their use for applications that require significant (> 500) operational cycles.
- Initial analysis of next generation LiS cell chemistries indicate that their increased energy density and improve impedance characteristics will improve the usable pack capacity and performance.

Research should continue to evaluate the abilities of LiS chemistry for electric aircraft

propulsion.

Chapter 5

A Coupled Electrochemical-Thermal Model for Lithium Sulfur Batteries

Note: Part of this chapter was published as an ECS abstract and presented at the Pacific Rim Meeting on Electrochemical and Solid State Science (PRiME), October 2020.

5.1 Introduction

Lithium sulfur batteries are a promising option for next-generation energy storage in electric transportation, and some companies have reported values over 400 Wh/kg[78]. The push for more energy density within batteries can result in higher resistive batteries. For lithium sulfur batteries in particular, a study has shown that the cell resistance increases with increased capacity[79]. As the energy stored within battery packs increase, the importance of thermal management for safety and performance also grows, which requires an accurate thermal model for design and control. A joint understanding of the thermal and electrochemical behavior is especially important in a system as nonlinear and complex as lithium sulfur batteries. However, the majority of lithium sulfur physics-based models are isothermal and do not consider thermal effects. To that end, we propose coupling a thermal and electrochemical model for lithium sulfur batteries.

To describe the electrochemical behavior, our work utilizes physics-based models that give insight into the internal states of a battery, which describe phenomena that can contribute to decreased performance under certain conditions. The lithium sulfur model in this study is the one-dimensional physics-based model developed by Kumaresan et al.[4] that considers transport, kinetics, thermodynamics, and morphological changes within

the lithium sulfur cell under isothermal conditions. The corresponding set of equations results in a numerically stiff system with variables evolving across many orders of magnitude.

Mathematical thermal models have been developed for lithium sulfur batteries, including both 2D[80] and lumped models[81]. These models are based on the general energy balance for batteries by Bernardi et al.[82] and include heat generation terms that are functions of thermodynamics, overpotentials, and material conductivities. The work by Stroe et al.[81] also detailed an experimental plan for determination of parameters, as well as their experimentally derived values. The results from the 2D model study found that the temperature gradients within the cell were negligible, which indicates that a lumped model may capture the thermal behavior well.

In this work, we extend mathematical modeling of lithium sulfur batteries by coupling the 1D LiS model with a thermal model based on the work by Stroe[81], which includes heat generation due to internal resistance and entropic contributions. Suitable approximations are made to estimate the various source terms within the thermal model. Coupling the thermal model with a more accurate predictive electrochemical model allows further insight into battery performance and future use in estimation and control.

5.2 Model Development

The 1D LiS battery model equations that describe the electrochemical behavior are detailed in Chapter 2. The thermal model was developed based on the work by Pals and Newman[83]. The temperature is a function of ohmic heating and heat due to the electrochemical reactions. Heat transfer is described by Fourier's Law within the battery. The ohmic heating is to the resistance of the passage of current throughout the battery. We have ignored ohmic heating in the current collector and the anode. The reversible heat generation of the reactions is modeled through the sum of each individual reaction. The reversible heating is a function of the current of that reaction, temperature of the cell, and the entropic heat coefficient. The entropic heat coefficient can be either positive or negative and is the heating due to the entropy changes during the reactions. We use a Maxwell relation to calculate the entropic heat coefficients from entropy changes for individual reactions as calculated by molecular simulations reported by Kuz'mina and associates[84]. The irreversible heating is caused primarily by the reaction overpotentials. For the thermal boundary conditions, natural convection is assumed outside the cell. The initial temperature and the ambient air temperature are 298 K. For this work, we have developed a single sandwich model, and for our future work, we will be considering more layers to more accurately depict the thermal behavior.

The thermal balance for the cathode includes heat flux and heat generation terms from reversible, irreversible, and ohmic heating

$$\rho_1 C_{p,1} \frac{\partial T_1}{\partial t} = -\frac{\partial q_1}{\partial x} + Q_{reversible} + Q_{irreversible} + Q_{ohmic,1} \tag{5.1}$$

Where ρ_1 is the density of the cathode, C_p is the heat capacity, T_1 is the temperature within

the cathode, q_1 is the heat flux.

A similar balance can be written for the separator:

$$\rho_2 C_{p,2} \frac{\partial T_2}{\partial t} = -\frac{\partial q_2}{\partial x} + Q_{ohmic,2} \tag{5.2}$$

The local thermal fluxes, q, are defined by the constitutive equation

$$q = -\lambda \frac{\partial T}{\partial x} \tag{5.3}$$

Where λ_1 is the thermal conductivity.

Each of the electrochemical reactions' contributions to the total reversible heat generation is considered through summing them up within the cathode

$$Q_{rev} = \sum_j Q_{rev,j} \tag{5.4}$$

Where j is the electrochemical reaction.

For each electrochemical reaction j, there is reversible heat generated described by the following:

$$Q_{rev,j} = a i_j T_1 \frac{\partial U_j}{\partial T} \tag{5.5}$$

Where a is the area available for electrochemical reactions within the cathode, i_j is the current due to reaction j, T is the temperature of the cathode, dU/dT is the entropic heat coefficient due to reaction j.

In order to calculate the entropic heat coefficient for each reaction, the values for the net entropy change for a similar reaction scheme were taken from work by Kuz'mina et. al.[84] The entropy values were then calculated for the reaction scheme for this model. The values for the entropic heat coefficient were calculated according to the following equation taken from[85]

$$\Delta S_j = n_j F \frac{\partial U_j}{\partial T} \tag{5.6}$$

Where ΔS is the entropy change for each reaction j, n denotes the number of electrons transferred, and F is Faraday's constant.

The irreversible heat during discharge is

$$Q_{irrev} = \sum_j Q_{irrev,j} \tag{5.7}$$

Where each individual reaction's contribution is

$$Q_{irrev,j} = a i_j \left(\phi_s - \phi_l - U_{j,ref} \right) \tag{5.8}$$

Where ϕ_s is the potential in the solid phase, ϕ_l is the potential in the liquid phase, and U_j is the equilibrium potential for reaction j.

Ohmic heat produced by the flow of current is defined as

$$Q_{ohmic,l} = -i_s \frac{\partial \phi_s}{\partial x} - i_{l,e} \frac{\partial \phi_{l,e}}{\partial x} \tag{5.9}$$

Where i_s is the current in the solid phase and $i_{l,e}$ is the current in the liquid phase within the cathode.

Substitute the following equation for the electrolyte phase current density:

$$i_{l,e} = F \sum_i z_{l,i} N_{l,i} \tag{5.10}$$

Where z_i is the charge number of species i, N_i is the flux of species i.

Ohm's law for the solid phase current is

$$i_s = -\sigma \frac{\partial \phi_s}{\partial x} \tag{5.11}$$

Where σ is the electronic conductivity of the solid phase.

After substituting, the equation in the cathode is

$$Q_{ohmic,1} = \sigma\left(\frac{\partial \phi_s}{\partial x}\right)^2 - \frac{\partial \phi_{e,1}}{\partial x} F \sum_i z_{1,i} N_{1,i} \tag{5.12}$$

The following boundary conditions apply as well:

At the cathode/CC interface where x=0, the boundary condition is

$$q = -h(T_1 - T_{amb}) \tag{5.13}$$

Where h is the heat transfer coefficient, T_{amb} is the ambient temperature.

The continuity equations hold at the cathode/separator interface, $x=L_{cat}$

$$T_1 = T_2 \tag{5.14}$$

$$q_1 = q_2 \tag{5.15}$$

The convective boundary condition applies to the separator/anode interface, $x=L_{cat}+L_{sep}$

$$q = -h(T_{amb} - T_4) \tag{5.16}$$

5.3 Results

To understand the rate dependence of the thermal behavior, three different rates were compared with low natural convection (h=1 W/m²K) in Figure 5.1. Everything is compared on a capacity basis. As the rate increases, there is increased polarization, and these losses result in depressing the voltage curve and capacity loss at the end of discharge. As expected, the temperature rise increases with higher rates (Figure 5.1 (b)). The temperature rise is greatest initially with another increase at the point of inflection between the two plateaus. To understand the heat sources, the heats have been included. Ohmic heating (Figure 5.1 (c)) increases dramatically at the transition between the two plateaus and decreases until another steep increase at the end of discharge, indicating the conductivity is lowest during those rises. The ohmic heating is about 5x larger for the 1C

rate than 0.5C due to ohmic heating in the electrolyte phase. The heat generation from the reactions shown in Figure 5.1 (d) is around an order of magnitude larger than ohmic heating. The reversible heating (---) is larger than the irreversible heat (– – –) during the first plateau, and then the irreversible heat increases steadily until the end of discharge, indicating the overpotentials are larger in the second half of discharge. For the ohmic heating and the reaction heats, the increase in rate accompanies a similar increase in Q.

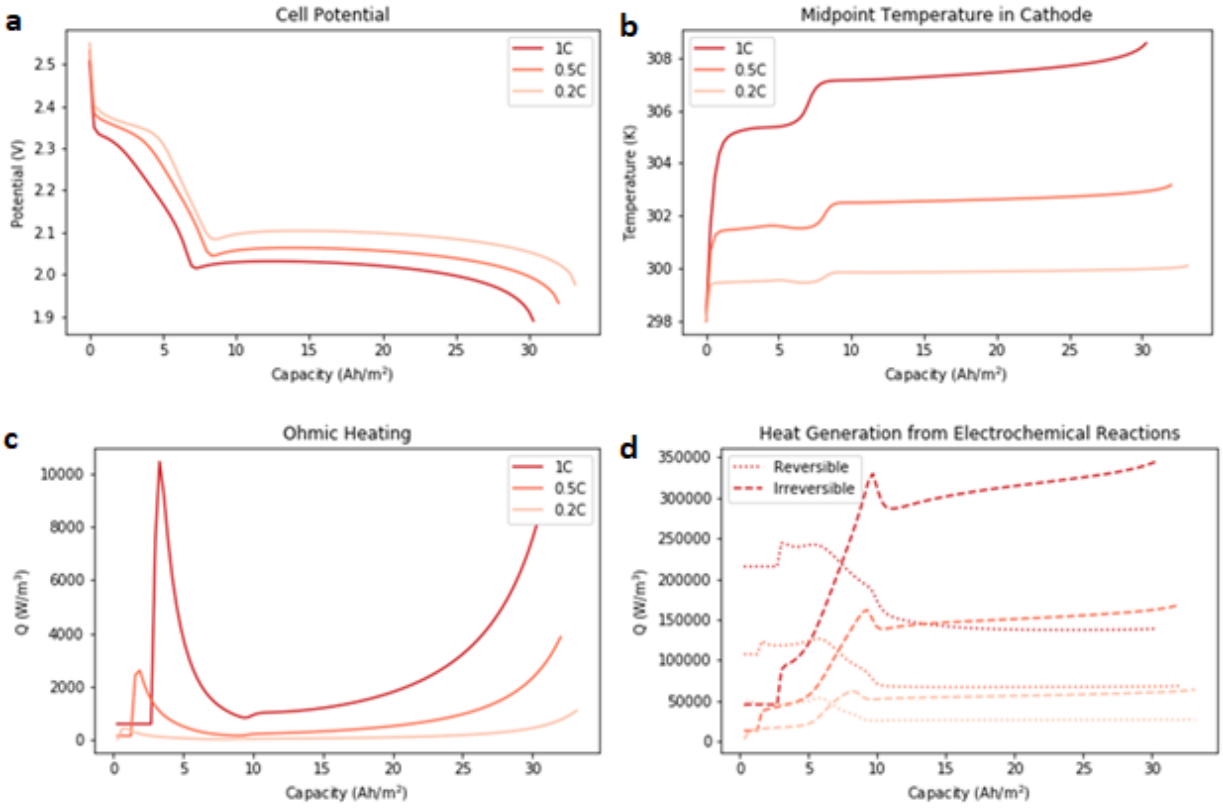

Figure 5.1. Rate Dependence of thermal behavior with low natural convection at 1C (dark red), 0.5C (medium red), 0.2C (light red).

To understand the effect of cooling, different convective conditions were considered for low natural convection (h=1 W/m²K) to forced air cooling (h=100 W/m²K) at 1C. The voltage profile has been included in Figure 5.2 (a); for each of the convective conditions, the same electrochemical behavior is predicted due to the simplification that

none of the electrochemical parameters are functions of temperature. The kinetic parameters especially would be expected to have sensitivity to temperature changes. Figure 5.2 (b) shows the midpoint temperature of the cathode during discharge with different heat transfer coefficients. As the rate of convection is increased, the rise in temperature decreases significantly, and for the highest rate of convection, the temperature increase is negligible. With natural convection, the maximum temperature rise under these conditions is about 10K.

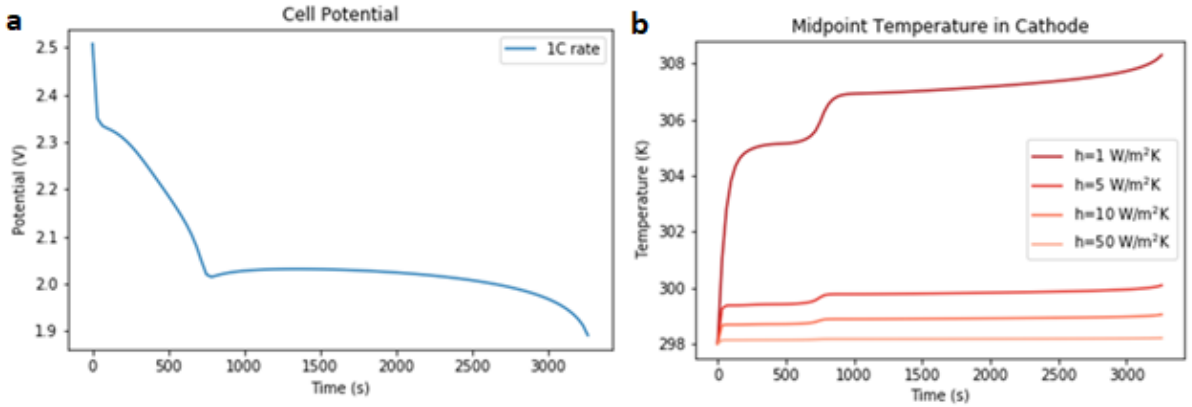

Figure 5.2. Variance convective heating conditions at 1C (a) voltage profile, (b) cathode midpoint temperature at different heat transfer coefficients.

To further compare the thermal sources in the model, Figure 5.3 shows the temperature rise with and without heat generation from the reactions at the 1C and natural convection conditions. With only ohmic heating, the temperature rise is basically negligible even at the high rate. When considering the reaction heat generation, the temperature rise is around 10 K at the discharge. Under these conditions, the heat generation from the electrochemical reactions dominate over the ohmic heating. The transport parameters may not reflect the actual liquid phase conductivity in a real cell, which highlights the importance of measuring these parameters.

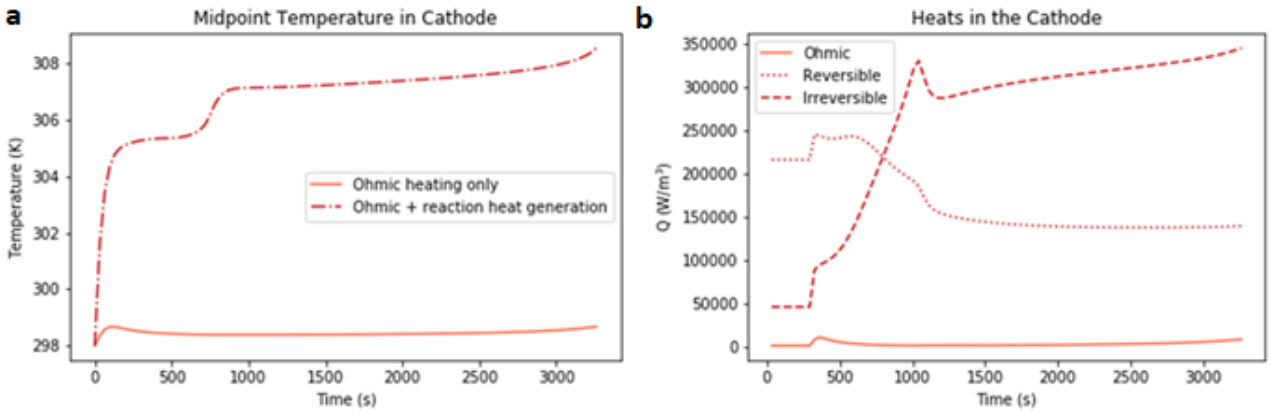

Figure 5.3. Closer look at the Heating terms for 1C operation and natural convection.

5.4 Conclusions

A coupled electrochemical-thermal model for lithium sulfur batteries has been developed. The thermal part of the model is affected by the electrochemical behavior; however, the other parameters are currently not functions of temperature. The results from the model indicate that the ohmic heating within the cell is negligible even at high rates. However, this may not be the case in real cells where transport limitations as well as insulating sulfur may reduce the electrolyte phase conductivity. The thermodynamic parameters were taken from MD simulations for a similar reaction scheme, and the contributions from the electrochemical reactions were within reason. For a more detailed examination of the thermal behavior, collaboration with experimentalists that could perform thermal characterization of lithium sulfur cells is vital. The effect of temperature on the kinetic, transport, and thermodynamic parameters is another interesting area of study that is lacking in both modeling and experimental efforts.

Chapter 6

LiS speciation modeling work in collaboration with Pacific Northwest National Laboratory and Brookhaven National Laboratory

6.1 Introduction

We have previously developed an efficient Tank-in-Series model[60] (Chapter 2) that is capable of simulating voltage curves, and since it is a physics-based model, it can be used to identify the evolution of intermediate polysulfide species with discharge. An ongoing collaboration with Pacific Northwest National Laboratory (PNNL) and Brookhaven National Laboratory (BNL) involves developing a parameter estimation framework to fit experimental data from coin cells made by PNNL. After fitting the model to experimental data, we can look at the internal concentration of different polysulfides species changing with state-of-charge, which will then be used to match these in a qualitative manner to BNL's XRD data where they have proposed different spectra for different polysulfides at various states-of-charge.

6.2 Coin Cell Preparation and Electrochemical Characterization

The coin cells were made by PNNL with integrated Ketjen Black/Sulfur (IKB/S) composite with a weight ratio of IKB:S of 1:4. The sulfur loading for each cell is 4 mg cm^{-2} with a porosity of 45%. The E/S ratio of the cells are 4 µl/mg, which is considered lean

conditions. The coin cells were assembled in an Ar-filled glovebox with a lithium anode 250 μm thick. The separator is a Celgar-2400 with 1.9 cm diameter; the electrolyte is made of 1 M lithium bis(trifluoromethanesulfonyl)imide (LiTFSI, Gotion), 1,3-dioxolane (DOL, Gotion) and 1,2-dimethoxyethane (DME, Gotion) (1: 1, v/v), 0.3 M $LiNO_3$. Before assembling the coin cells, the IKB:S particles were separated according to size. Seven coin cells were made with particles less than 20 μm (SM), and the other 7 cells were made with particles of around 90 μm (LG).

The cells were tested at 0.1C on a LANHE battery tester at 30°C with a voltage window of 1.8 to 2.8 V, and each cell was stopped at various states of discharge and charge.

6.3 X-Ray Diffraction Characterization

After the cells were cycled, they were disassembled in an Ar-filled glovebox and dried overnight. The dried discs were sealed into an aluminum-lined pouch cell under Ar. The sealed pouches were sent to beamline 28-ID-2 of the National Synchrotron Light Source II (NSLS-II) at Brookhaven National Laboratory. CeO_2 powder (674b, NIST) in a Kapton capillary (1.1 mm in diameter) was used for calibration. The diffraction data was collected with X-rays with a wavelength of 0.19316 Å, and integration of the data was carried out over 0.5 – 15^0 of a 2q range (d = 0.37-11.07 Å); masks were used to exclude the beam stop and the edges of the detector.

6.4 Model Development

The Kumaresan model[4] utilizes a reference state of almost 100% state-of-charge to define parameters. The formulation of the Butler-Volmer and Nernst expressions are framed in relation to a reference state. Let us call the expression below an effective overpotential

$$\eta_{j,eff} = V - U_{j,ref} \tag{6.1}$$

which as written in the model is constant due to the definition of $U_{j,ref}$

$$U_{j,ref} = U_j^{\theta} - \frac{RT}{nF}\sum_i s_{i,j} \ln\left[\frac{C_{i,ref}}{1000}\right] \tag{6.2}$$

Where $C_{i,ref}$ is a constant reference concentration. The effective overpotential for each reaction j does not change with state of charge and is therefore not a true overpotential that describes how far a reaction is from equilibrium. A true overpotential will be equal zero when the system is relaxed and at equilibrium. The Butler-Volmer expression is also defined against a reference exchange current density.

$$i_j = i_{0\,j,ref}\left[\left(\frac{C_R}{C_{R,ref}}\right)^{p_{i,j}} e^{\frac{(1-\alpha)nF}{RT}\eta_{j,eff}} - \left(\frac{C_O}{C_{O,ref}}\right)^{q_{i,j}} e^{\frac{-\alpha nF}{RT}\eta_{j,eff}}\right] \tag{6.3}$$

Where C_R is the concentration of the anodic species, C_O is the concentration of the cathodic species.

Previous work from our group for lithium sulfur modeling[60,86] used the Butler-Volmer expression from Kumaresan with reference values but included a concentration-dependent overpotential expression

$$\eta_j = V - U_j \tag{6.4}$$

$$U_j = U_j^{\theta} - \frac{RT}{nF}\sum_i s_{i,j} \ln\left[\frac{C_i}{1000}\right] \tag{6.5}$$

Where the reference concentration is replaced with the varying concentration. With this model formulation, the overpotentials did not tend to zero as the cell relaxed. To maintain thermodynamic consistency and use a true overpotential expression especially with ongoing electrochemical impedance spectroscopy, the model formulation has been

updated to the Newman formulation below[87]

$$\eta_j = V - U_j$$
$$U_j = U_j^{\theta} - \frac{RT}{nF}\sum_i s_{i,j} \ln\left[\frac{C_i}{1000}\right]$$
$$i_0 = nFk_f^{(1-\alpha)}k_b^{\alpha} \tag{6.6}$$
$$i_j = i_0 C_R^{\alpha p_{i,j}} C_O^{(1-\alpha)q_{i,j}} \left[e^{\frac{(1-\alpha)nF}{RT}\eta_j} - e^{\frac{-\alpha nF}{RT}\eta_j} \right]$$

The formulation in the Kumaresan model reduces to the Newman formulation when considering a reference state, but for this and future work, the Newman formulation is preferred for the true overpotential definition and the lack of a reference state when most of the parameters have been assumed and not determined experimentally. The base parameters taken from Kamyab et. al.[56] have been calculated according to this formulation.

6.5 Estimation Framework

The initial guess for input parameters was taken from the work by Kamyab et. al. [56] and calculated for the Newman formulation of the i_o values with no reference. The design parameters for sulfur loading, porosities, and thicknesses were taken from the experimental conditions provided by PNNL and are shown in Table 6.1 below.

Table 6.1. Design parameters for the 14 coin cells from PNNL.

Parameter	Value
Areal sulfur loading (mg/cm^2)	4
Sulfur volume fraction [a]	32%
Cathode thickness (µm) [a]	60
Separator Thickness (µm) [a]	24
Cathode porosity [a]	45%
Separator porosity [a]	41%
Carbon/binder volume fraction [a]	23%
Calculated E/S ratio (mL/g)	0.86

[a] Input to model

The estimation framework was written in Matlab. The error function that is minimized during optimization is the root mean square error (RMSE) between the experimental voltage curve and the model voltage predictions. The optimizer for parameter estimation is the Genetic Algorithm (GA), which is well-adapted to handle a nonlinear optimization problem with a large parameter space that is presented here. GA is based on natural selection and for each iteration generates a population of points where the best point approaches the optimal. The next population is generated through randomly-selected parents that are used to create the children through crossover from two parents or mutation of one parent. The population then evolves towards an optimal solution[88]. The initial guess to the optimizer is not used; the bounds are therefore very important.

The experimental data chosen for estimation was LG 5, which is representative of the LG particle data. At this point, the parameter estimation was focused on discharge. Throughout the discharge curve, there were four different cell stops where speciation splits are requested.

6.6 Estimation Results

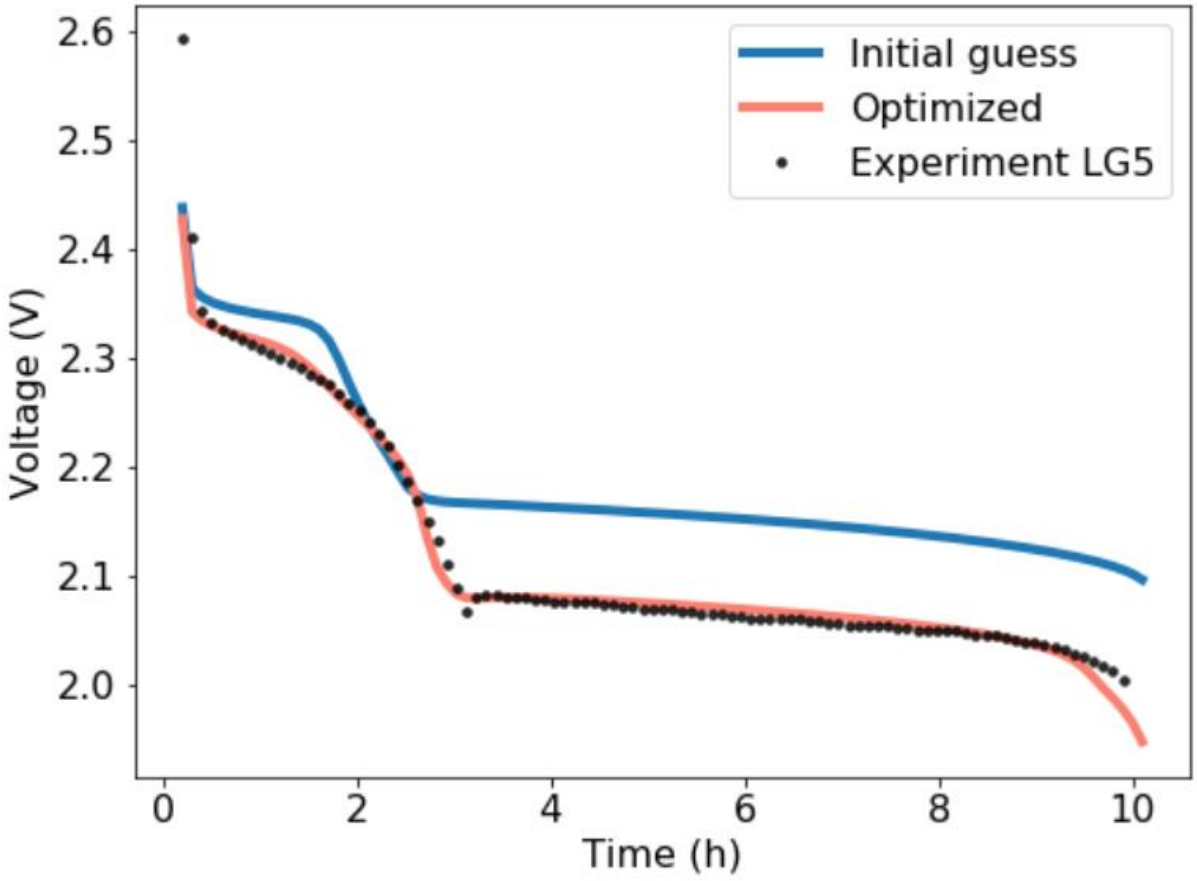

Figure 6.1. Voltage comparison of experiment data of LG particle cell #5 (dotted), the guess with initial parameters (solid blue line), and the optimized output (solid orange line) from parameter estimation by GA.

The parameters that were estimated in optimization are U_j^{θ}, k_k, and $K_{sp,k}$ that primarily determine the thermodynamics of the electrochemical reactions and the kinetics and equilibrium of the precipitation reactions. The voltage curve begins at around 3 V with a sharp drop to the first plateau around 2.35 V. For estimation, the 500 mV drop at the beginning and the first few data points were not considered; the window is 1-98% SOC. The root mean square error (RMSE) between the initial parameter guess and the

experimental data is 80 mV, and after optimization, the voltage with the best estimated parameters has 19 mV of RMSE. The major features are captured, such as the first plateau, transition, and the second plateau. In Table 6.2, the parameter values have been listed. The largest change in parameters is the value for K_{sp} of Li_2S; this dictates the ratio of soluble reactants to the precipitate. The estimate value is many orders of magnitude lower, indicating that the equilibrium of the precipitation is heavily favoring the precipitated form. Another change in the parameter set of note is the middle U values are very close together, which blurs the distinction in the voltage curve between those two reactions and results in a smoother transition to the second plateau. To further reduce the RMSE, the kinetic parameters could be optimized as well.

Table 6.2. Estimated parameters with initial guess and final optimized value.

Parameter	Initial Guess	Optimized Value
U_2^θ (V)	2.39	2.38
U_3^θ (V)	2.37	2.29
U_4^θ (V)	2.24	2.26
U_5^θ (V)	2.04	2.07
U_6^θ (V)	2.01	1.81
k_{S8} (s^{-1})	1.0	0.41
k_{Li2S} (m^6 mol^2 s^{-1})	$1x10^{-4}$	$1.2x10^{-4}$
$K_{sp,S8}$ (mol m^{-3})	19	17
$K_{sp,Li2S}$ (mol^3 m^{-9})	$1x10^5$	0.018

Table 6.3 contains the speciation breakdown at the % SOC of interest where the coin cell was stopped and dried. The two most prevalent species are highlighted in black while the other species are in gray. The solid species have also been included. The total molar inventory of each species has been calculated and shown in units of $mmol/m^2$. It is important to note that the expected precipitated species after the cells were dried would

be $Li_2S_{n(s)}$ for the polysulfide n.

The speciation breakdown shows a distinction between the high and low plateaus and the consequential polysulfide splits. Both the 85% and 74% SOC occur before the nucleation point and the start of the second plateau. The most prominent species are S_8^{2-} and S_6^{2-} for the highest SOC, and S_6^{2-} and S_4^{2-} for the next SOC. The second set of SOC's are firmly in the second plateau, and have predictably lower-order polysulfide species that dominate. At the very end of discharge, Li2S is one of the two most abundant species.

Table 6.3. Speciation at specific SOC's corresponding to the coin cell stop conditions. Units are mmol/m^2.

	85% SOC	**74% SOC**	**26% SOC**	**1% SOC**
$S_8(s)$	0.0225	$7.23*10^{-4}$	$9.64*10^{-11}$	$4.16*10^{-12}$
$S_8(l)$	0.0965	$8.65*10^{-8}$	$2.99*10^{-13}$	$4.85*10^{-12}$
S_8^{2-}	91.5	0.826	$1.50*10^{-5}$	$1.26*10^{-10}$
S_6^{2-}	82.6	25.2	0.0602	$4.47*10^{-11}$
S_4^{2-}	34.2	351	111	$1.53*10^{-3}$
S_2^{2-}	$9.38*10^{-3}$	3.23	135	30.0
S^{2-}	$5.53*10^{-9}$	$1.10*10^{-5}$	$4.01*10^{-6}$	$3.48*10^{-5}$
$Li_2S(s)$	$3.07*10^{-7}$	$3.13*10^{-7}$	0.747	1.22

6.7 Unsupervised Machine Learning Methods on the X-Ray Diffraction Data

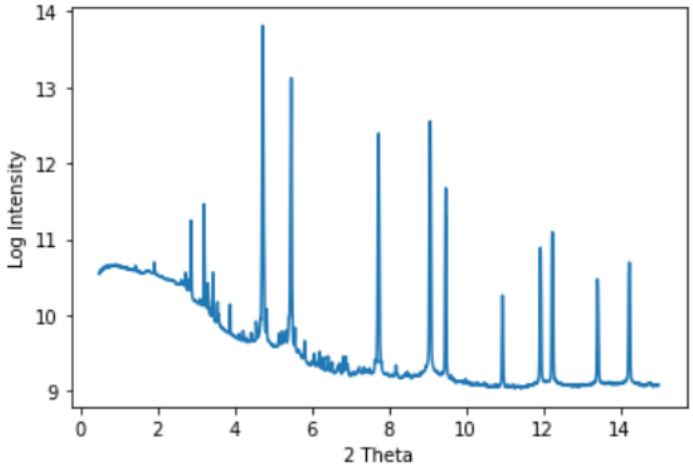

Figure 6.2. Typical log-scaled XRD spectra with intensity versus 2 Theta.

In addition to the parameter estimation and speciation identification, data science methods were applied to the XRD data. Principle Component Analysis (PCA) is an unsupervised machine learning method that helps to identify the explanatory factors within the dataset. The dataset naturally divides itself into several distinctions: LG/SM, discharge/charge, and SOC above or below a set voltage. Through exploring the dataset with PCA, the features within the spectra can be associated with the given coupling; the XRD domain scientists can explain the selected features and relate them to materials.

A typical XRD spectra is shown in Figure 6.2. Each of the peaks holds information about the solids within the cell from the intensity and 2θ location. The mean of the dataset captures the most variance in one spectrum, shown in Figure 6.3.

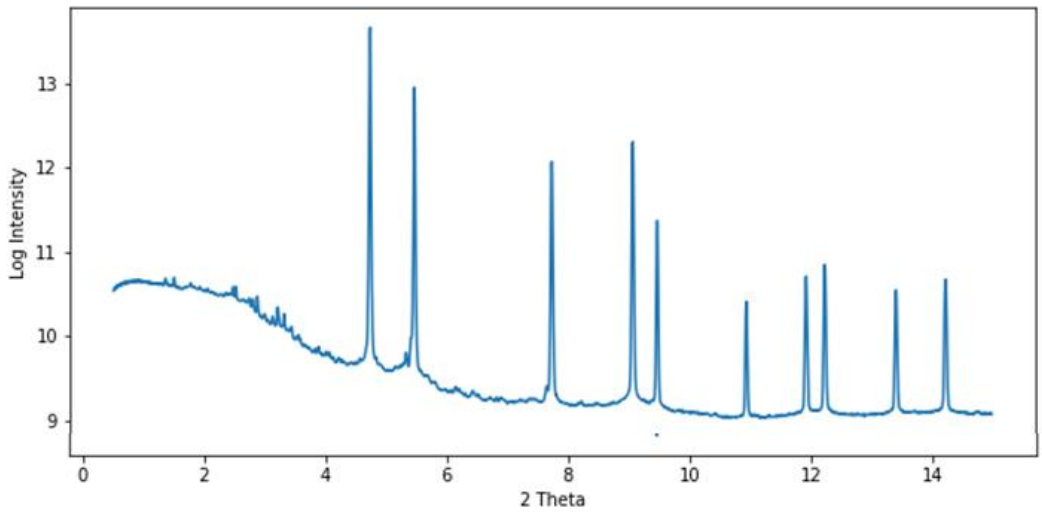

Figure 6.3. Mean of the XRD data, which captures the single-most variance within the dataset.

One way to compare the unique features of two spectra is to take the difference, which is included in Figure 6.4; the unique features become more apparent.

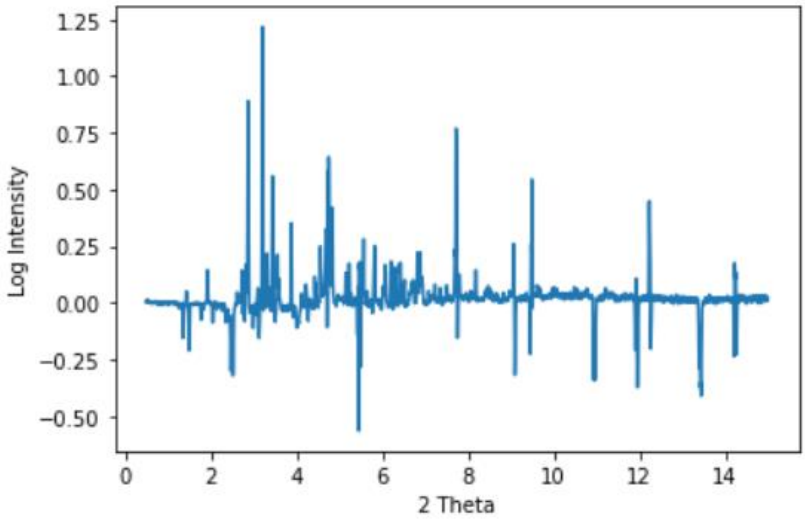

Figure 6.4. Difference between two log-scaled spectra. The peaks indicate shifts between the data.

Principal component analysis (PCA) is an unsupervised machine learning technique that is commonly used to reduce high-dimensional data while still capturing the most information possible. In this case, the high-dimensional data is every 2 Theta measurement and peak. PCA works by first standardizing the data to ensure each variable

contributes equally; the mean of the data is calculated and subtracted from each spectrum. Next, the covariance matrix is computed, which helps identify if two variables are highly correlated to eliminate redundancy. The eigenvectors and eigenvalues of the covariance matrix are then computed to identify the principal components. The principal components are combinations of the initial variables but chosen in such a way that the maximum variance is captured with component 1 and so on. The principal components are orthogonal to each other, which means that the information they contain is independent of the other components[89].

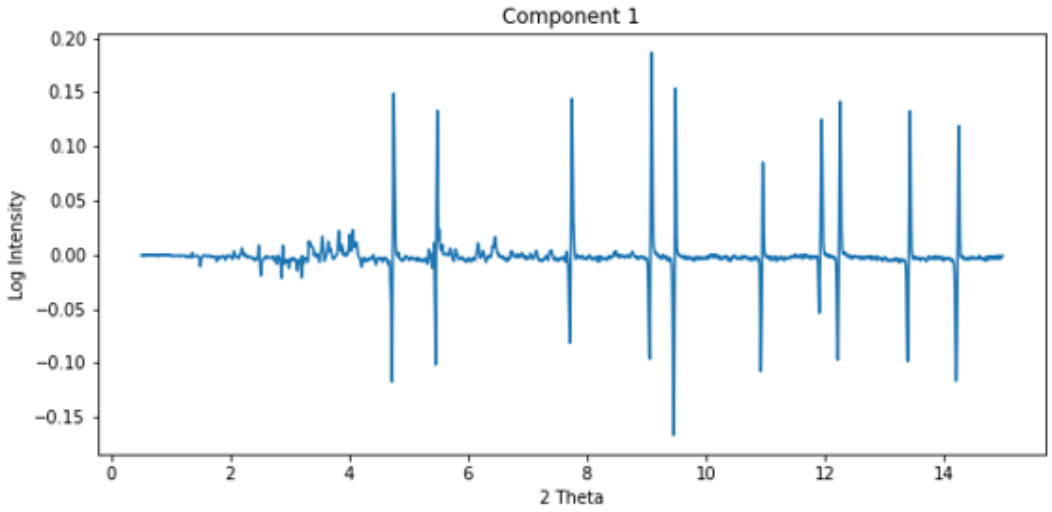

Figure 6.5. Principal Component 1 that contains 40% of the explained variance within the dataset.

After applying PCA on this dataset, there are 14 total principal components (the eigenvectors) each with 14 eigenvalues for each spectrum. To calculate a spectrum, the mean is added to a principal component that is multiplied by the spectrum's eigenvalue for that component; including more principal components increases the explained variance. The eigenvalues for each datapoint represent changes from the principal component by shifting the peaks left or right depending on the sign and magnitude. The principal components resemble the difference between two spectra, Figure 6.5.

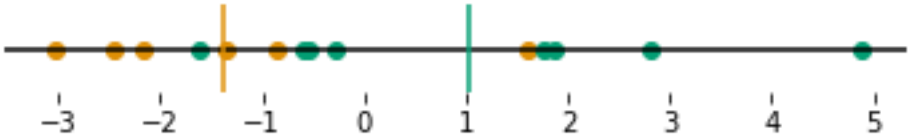

Figure 6.6. Line plot of the eigenvalues of the principal component 1, where assigned charging data is orange and discharge is green. The population means are shown as vertical lines and calculated to be statistically different from each other.

As noted earlier, the data has natural segregations into LG vs SM particle sizes, charging vs discharging, and voltage/state-of-charge cutoffs. To explore assigning components and the peak shifts to physical meaning, each of the 14 data points was categorized as one of the two populations, for example charging versus discharging. Then, for each of the components, a double-sided student t test with 95% confidence was performed on the eigenvalues of each datapoint with the null hypothesis of the population means being identical. For the charge/discharge split, the first component with 41% of the explained variance had a statistically significant p value of 0.05 or less, Figure 6.6. The charge is orange; discharge is green. The pristine cells were assigned charge.

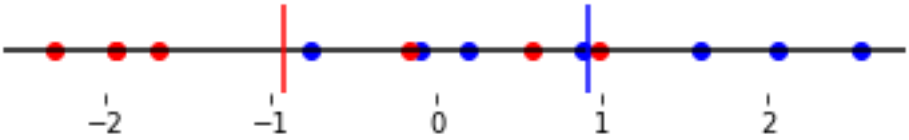

Figure 6.7. Line plot of the eigenvalues of the principal component 2, where LG data is blue and SM is red. The population means are shown as vertical lines and calculated to be statistically different from each other.

The next split that was considered is LG/SM particles. After each of the points were identified as either LG/SM, the same statistical t test was performed on each of the population means. The second principal component eigenvalues with 20% explained variance were statistically significant, shown in Figure 6.7. The large particles are in blue; the small particles are in red. Principal Component 2 (PC2) is shown in Figure 6.8. The range of the log intensity of the peaks for PC2 is about 5x smaller than each of the principal

components. The captured variance is focused on the curvature of the baseline rather than the magnitude of the peaks.

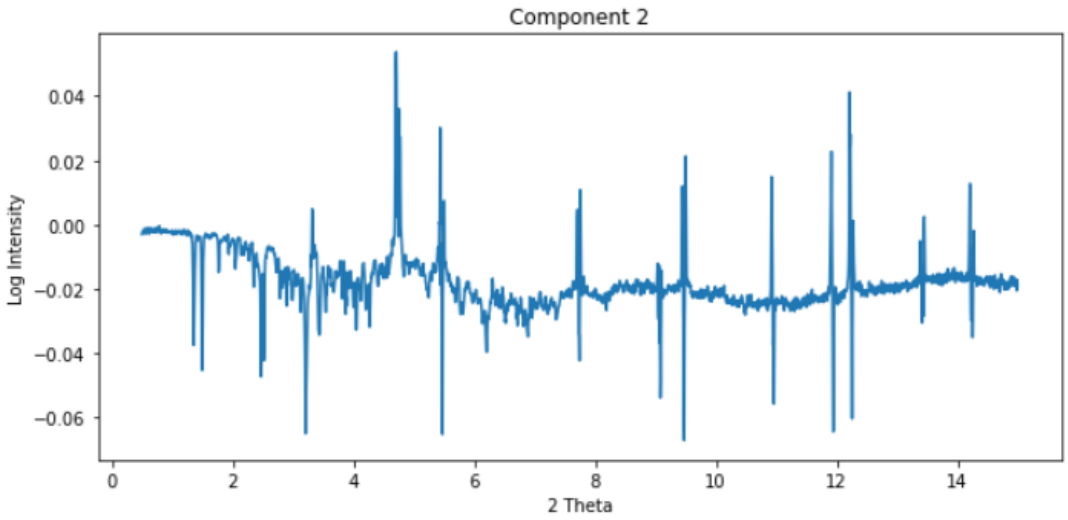

Figure 6.8. Principal Component 2 that contains 20% of the explained variance of the dataset.

Another statistical t test was performed on the data with a cutoff voltage of 2.3 V. The third principal component was statistically significant, shown below in Figure 6.9. Brown is above 2.3 V; pink is below 2.3 V.

Figure 6.9. Line plot of the eigenvalues of the principal component 3, where brown indicates cells stopped at an SOC above 2.3 V and pink is below that. The population means are shown as vertical lines and calculated to be statistically different from each other.

The principal component 3 is shown in Figure 6.10 and captures 12% of the explained variance. The peaks that have corresponding negative peaks at about the same 2 Theta indicate shifts in peaks left or right depending on the sign of the eigenvalues for a given spectrum. Some of the peaks do not have a corresponding up or down peak, which means that the peak is novel in the spectrum and contains new information, not just peak

shifts. With the expertise from the group at BNL, the peaks and shifts shown in each of the components can be correlated to the solid products.

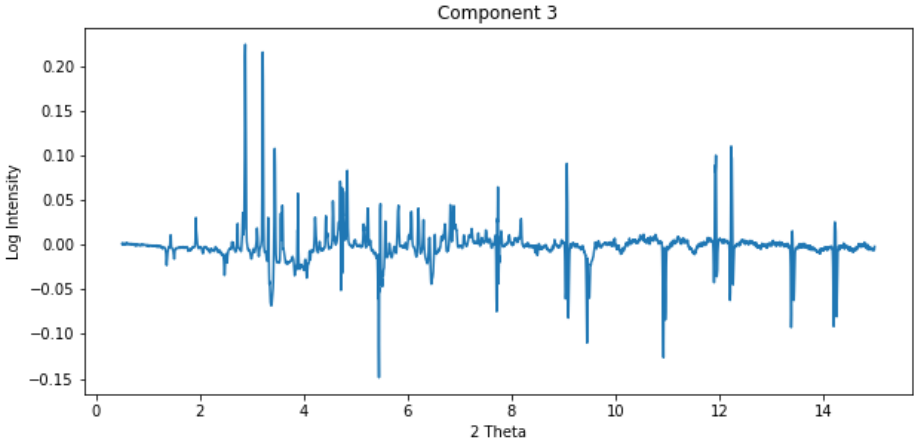

Figure 6.10. Principal component 3 that captures 12% of the explained variance.

Chapter 7

Conclusions and Perspective on Future Directions

7.1 Summary of Thesis Work

The work herein represents a sustained effort to develop efficient models that can collaboratively analyze and interpret experimental data. The Tanks-in-Series model is a step forward in bridging the gap between predictive and computationally intensive 1D models that describe full-cell behavior with transport effects and 0D lumped models designed for parameterization and computational efficiency. These efficient tools have been utilized to predict effects of electrolyte engineering, thermal behavior, and speciation with SOC. Cultivating and maintaining collaborations with experimentalists ensures relevancy of modeling efforts, and the beneficial exchange of ideas and direction gives our work a sense of purpose and place within the research community. The next sections highlight recommendations for furthering the important work outlined here.

7.2 Speciation Work

The speciation work from Chapter 3 should continue to focus on interpretation of electrolyte engineering. The reaction for these batteries is very complex and extremely important when considering polysulfide shuttle. The electrolyte determines the speciation mix, which directly affects the degradation. The addition of alternative chemistry can help elucidate the reaction scheme for a certain electrolyte system that is considered. The full-cell modeling predictions should be coupled with experimental work to accelerate work. The extension of the work within Chapter 3 is to include the $S_3^{\bullet-}$ radical

anion within the reduction scheme; there are a few different ways to go about this. Another avenue to pursue is adding in disproportionation reactions. The chemistry is quite complex so there are many options in regards to this, which underscores the importance of active collaborations with experimentalists to guide the modeling efforts.

7.3 Thermal Modeling

The coupled-thermal model is not truly coupled yet; the electrochemical behavior does not take the temperature information as an input. The natural next step in that work is to the include an Arrhenius-type dependence on the temperature for kinetics within the model. To further understand the possible limitations of the current model formulation, a wide-scale parameter study would be very useful. A sweep of the kinetic, thermodynamic, and transport parameters within the electrochemical model will impact the thermal behavior of the cell, and it would be most useful to be able to compare the thermal model predictions to experimental work. Cultivating and maintaining close collaborations with experimentalists is vital in ensuring the relevance of modeling work such as this, and this work would greatly benefit from thermal data at different rates and under different convective conditions to compare with model trends.

7.4 Control Applications

The Tanks-in-Series model is a really great candidate to use for cycling and control applications. Ongoing work within our group is exploring the reversibility of the 1D LiS model with the Newman formulation detailed in Chapter 6. Other groups have included extra terms within the precipitation reactions to ensure numerical stability. The development of a charging has been difficult for the 1D LiS discharge model. There have

been cycling studies that considered different mechanisms of polysulfide shuttle. With the numerical expertise within our group and the efficient and accurate Tanks-in-Series model, a control-based approach to developing a variable-current charging protocol to minimize degradation via polysulfide shuttle would be a very useful and stimulating direction for this work.

Bibliography

1. E. Jarratt, New lessons from the epic story of Moli Energy, the Canadian pioneer of rechargeable lithium battery technology, [Online; accessed 2021/06/03].
2. Brookhaven National Laboratory, National Synchrotron Light Source II, [Online; accessed 2021/06/05].
3. Y. V. Mikhaylik and J. R. Akridge, *J. Electrochem. Soc.*, **151**, A1969 (2004).
4. K. Kumaresan, Y. Mikhaylik, and R. E. White, *J. Electrochem. Soc.*, **155**, A576 (2008).
5. J. P. Neidhardt, D. N. Fronczek, T. Jahnke, T. Danner, B. Horstmann, and W. G. Bessler, *J. Electrochem. Soc.*, **159**, A1528–A1542 (2012).
6. D. N. Fronczek and W. G. Bessler, *J. Power Sources*, **244**, 183–188 (2013).
7. K. Yoo, M. K. Song, E. J. Cairns, and P. Dutta, *Electrochim. Acta*, **213**, 174–185 (2016).
8. A. F. Hofmann, D. N. Fronczek, and W. G. Bessler, *J. Power Sources*, **259**, 300–310 (2014).
9. M. Marinescu, L. O'Neill, T. Zhang, S. Walus, T. E. Wilson, and G. J. Offer, *J. Electrochem. Soc.*, **165**, A6107–A6118 (2018).
10. T. Zhang, M. Marinescu, S. Walus, and G. J. Offer, *Electrochim. Acta*, **219**, 502–508 (2016).
11. M. Marinescu, T. Zhang, and G. J. Offer, *Phys. Chem. Chem. Phys.*, **18**, 584–593.
12. N. Erisen, N. B. Emerce, S. C. Erensoy, and D. Eroglu, *Int. J. Energy Res.*, **42**, 2631–2642 (2018).

13. C. Michaelis, N. Erisen, D. Eroglu, and G. M. Koenig, *Int. J. Energy Res.*, **43**, 874–883 (2018).
14. T. Zhang, M. Marinescu, L. O'Neill, M. Wild, and G. Offer, *Phys. Chem. Chem. Phys.*, **17**, 22581–22586 (2015).
15. Y. X. Ren, T. S. Zhao, M. Liu, P. Tan, and Y. K. Zeng, *J. Power Sources*, **336**, 115–125 (2016).
16. T. Cleaver, P. Kovacik, M. Marinescu, T. Zhang, and G. Offer, *J. Electrochem. Soc.*, **165**, A6029–A6033 (2018).
17. Y. Diao, K. Xie, S. Xiong, and X. Hong, *J. Power Sources*, **235**, 181–186 (2013).
18. S. Xiong, K. Xie, Y. Diao, and X. Hong, *J. Power Sources*, **246**, 840–845 (2014).
19. D. Aurbach, E. Zinigrad, H. Teller, and P. Dan, *J. Electrochem. Soc.*, **147**, 1274 (2000).
20. G. Bieker, M. Winter, and P. Bieker, *Phys. Chem. Chem. Phys.*, **17**, 8670–8679 (2015).
21. K. H. Chen, K. N. Wood, E. Kazyak, W. S. LePage, A. L. Davis, A. J. Sanchez, N. P. Dasgupta, *J. Mater. Chem. A*, **5**, 11671–11681 (2017).
22. C. Fang, J. Li, M. Zhang, Y. Zhang, F. Yang, J. Z. Lee, M.-H. Lee, J. Alvarado, M. A. Schroeder, Y. Yang, B. Lu N. Williams, M. Ceja, L. Yang, M. Cai, J. Gu, K. Xu, X. Wang, Y. S. Meng, *Nature*, **572**, 511–515 (2019).
23. C.-S. Kim, A. Guerfi, P. Hovington, J. Trottier, C. Gagnon, F. Barray, A Vijh, M. Armand, K. Zaghib, *J. Power Sources*, **241**, 554–559 (2013).
24. D. A. Dornbusch, R. Hilton, M. J. Gordon, and G. J. Suppes, *J. Ind. Eng. Chem.*, **19**, 1968–1972 (2013).

25. M. Wild, L. O'Neill, T. Zhang, R. Purkayastha, G. Minton, M. Marinescu, G. J. Offer, *Energy Environ. Sci.*, **8**, 3477–3494 (2015).
26. M. Marinescu, T. Zhang, and G. J. Offer, *Phys. Chem. Chem. Phys.*, **18**, 584–593 (2016).
27. N. B. Emerce and D. Eroglu, *J. Electrochem. Soc.*, **166**, A1490–A1500 (2019).
28. M. Safari, C. Y. Kwok, and L. F. Nazar, *ACS Cent. Sci.*, **2**, 560–568 (2016).
29. V. Ramadesigan, P. W. C. Northrop, S. De, S. Santhanagopalan, R. D. Braatz, V. R. Subramanian, *J. Electrochem. Soc.*, **159**, R31–R45 (2012).
30. A. Subramaniam, S. Kolluri, C. D. Parke, M. Pathak, S. Santhanagopalan, and V. R. Subramanian, *J. Electrochem. Soc.*, **167**, 013534 (2020).
31. S. Waluś, C. Barchasz, R. Bouchet, J. C. Leprêtre, J. F. Colin, J. F. Martin, E. Elkaïm, C. Baehtz, and F. Alloin, *Adv. Energy Mater.*, **5**, 1500165 (2015).
32. M. T. Lawder, V. Ramadesigan, B. Suthar, and V. R. Subramanian, *Comput. Chem. Eng.*, **82**, 283–292 (2015).
33. A. Tomaszewska, Z. Chu, X. Feng, S. O'Kane, X. Liu, J. Chen, C. Ji, E. Ender, R. Li, L. Liu, Y. Li, S. Zheng, S. Vetterlein, M. Gao, J. Du, M. Parkes, M. Ouyang, M. Marinescu, G. Offer, B. Wu, *eTransportation*, **1**, 100011 (2019).
34. K. S. Han, J. Chen, R. Cao, N. N. Rajput, V. Murugesan, L. Shi, H. Pan, J.-G. Zhang, J. Liu, K. A. Persson, and K. T. Mueller, *Chem. Mater.*, **29**, 9023–9029 (2017).
35. Z. Liu, A. Mistry, and P. P. Mukherjee, *J. Electrochem. Energy Convers. Storage*, **15**, 10802 (2018).
36. S. Li, M. Jiang, Y. Xie, H. Xu, J. Jia, and J. Li, *Adv. Mater.*, **30**, 1–29 (2018).
37. F. Y. Fan, W. C. Carter, and Y.-M. Chiang, *Adv. Mater.*, **27**, 5203–5209 (2015).

38. A. Bhargav, J. He, A. Gupta, and A. Manthiram, *Joule*, **4**, 285–291 (2020).

39. D. Lu, Q. Li, J. Liu, J. Zheng, Y. Wang, S. Ferrara, J. Xiao, J. G. Zhang, and J. Liu, *ACS Appl. Mater. Interfaces*, **10**, 23094–23102 (2018).

40. R. Fang, S. Zhao, Z. Sun, D. W. Wang, H. M. Cheng, and F. Li, *Adv. Mater.*, **29**, 1606823 (2017).

41. J. Brückner, S. Thieme, H. T. Grossmann, S. Dörfler, H. Althues, and S. Kaskel, *J. Power Sources*, **268**, 82–87 (2014).

42. R. Xu, J. Lu, and K. Amine, *Adv. Energy Mater.*, **5**, 1500408 (2015).

43. M. Barghamadi, A. S. Best, A. I. Bhatt, A. F. Hollenkamp, M. Musameh, R. J. Rees, and T. Rüther, *Energy Environ. Sci.*, **7**, 3902–3920 (2014).

44. J. Cao, Q. Meisner, T. Glossmann, A. Hintennach, Y. Wang, P. Redfern, L. A. Curtiss, and Z. Zhang, *ACS Appl. Energy Mater.*, **3**, 3198–3204 (2020).

45. J. Zheng, D. Lv, M. Gu, C. Wang, J.-G. Zhang, J. Liu, and J. Xiao, *J. Electrochem. Soc.*, **160**, A2288–A2292 (2013).

46. H. L. Wu, L. A. Huff, and A. A. Gewirth, *ACS Appl. Mater. Interfaces*, **7**, 1709–1719 (2015).

47. R. Bouchal, A. Boulaoued, and P. Johansson, *Batter. Supercaps*, **3**, 397–401 (2020).

48. A. Gupta, A. Bhargav, and A. Manthiram, *Adv. Energy Mater.*, **9**, 1803096 (2019).

49. È. Boros, M. J. Earle, M. A. Gîlea, A. Metlen, A. V. Mudring, F. Rieger, A. J. Robertson, K. R. Seddon, and A. A. Tomaszowska, *Chem. Commun.*, **46**, 716–718 (2010).

50. S. I. Tobishima, H. Yamamoto, and M. Matsuda, *Electrochim. Acta*, **42**, 1019–1029

(1997).

51. M. Ghaznavi and P. Chen, *J. Power Sources*, **257**, 394–401 (2014).
52. M. Ghaznavi and P. Chen, *J. Power Sources*, **257**, 402–411 (2014).
53. M. Ghaznavi and P. Chen, *Electrochim. Acta*, **137**, 575–585 (2014).
54. T. Danner, G. Zhu, A. F. Hofmann, and A. Latz, *Electrochim. Acta*, **184**, 124–133 (2015).
55. D. Moy, A. Manivannan, and S. R. Narayanan, *J. Electrochem. Soc.*, **162**, A1–A7 (2015).
56. N. Kamyab, P. T. Coman, S. K. Madi Reddy, S. Santhanagopalan, and R. E. White, *J. Electrochem. Soc.*, **167**, 130532 (2020).
57. A. N. Mistry and P. P. Mukherjee, *J. Phys. Chem. C*, **122**, 18329–18335 (2018).
58. M. Marinescu, L. O'Neill, T. Zhang, S. Walus, T. E. Wilson, and G. J. Offer, *J. Electrochem. Soc.*, **165**, A6107–A6118 (2018).
59. J. Shim, T. J. Ko, and K. Yoo, *J. Ind. Eng. Chem.*, **80**, 283–291 (2019).
60. C. D. Parke, A. Subramaniam, S. Kolluri, D. T. Schwartz, and V. R. Subramanian, *J. Electrochem. Soc.*, **167**, 163503 (2020).
61. V. Thangavel, K. Xue, Y. Mammeri, M. Quiroga, A. Mastouri, C. Gu, P. Johansson, M. Morcrette, and A. A. Franco, *J. Electrochem. Soc.*, **163**, A2817–A2829 (2016).
62. V. Thangavel, A. Mastouri, C. Guéry, M. Morcrette, and A. A. Franco, *Batter. Supercaps*, 152–162 (2020).
63. F. Gaillard, E. Levillain, and J. P. Lelieur, *J. Electroanal. Chem.*, **432**, 129–138 (1997).
64. F. Gaillard, E. Levillain, M. C. Dhamelincourt, P. Dhamelincourt, and J. P. Lelieur,

J. Raman Spectrosc., **28**, 511–517 (1997).

65. B. Kim and S. Park, *J. Electrochem. Soc.*, **140**, 115–122 (1993).
66. D.-H. Han, B.-S. Kim, S.-J. Choi, Y. Jung, J. Kwak, and S.-M. Park, *J. Electrochem. Soc.*, **151**, E283 (2004).
67. Z. Wang, Y. Tang, X. Fu, J. Wang, Z. Peng, L. Zhang, and J. Huang, *ACS Appl. Mater. Interfaces*, **12**, 55971–55981 (2020).
68. Q. Zou, Z. Liang, G. Y. Du, C. Y. Liu, E. Y. Li, and Y. C. Lu, *J. Am. Chem. Soc.*, **140**, 10740–10748 (2018).
69. H. Shin, M. Baek, A. Gupta, K. Char, A. Manthiram, and J. W. Choi, *Adv. Energy Mater.*, **10**, 1–21 (2020).
70. J. Xie, Y. W. Song, B. Q. Li, H. J. Peng, J. Q. Huang, and Q. Zhang, *Angew. Chemie - Int. Ed.*, **59**, 22150–22155 (2020).
71. R. N. Methekar, V. Ramadesigan, J. C. Pirkle, and V. R. Subramanian, *Comput. Chem. Eng.*, **35**, 2227–2234 (2011).
72. V. R. Subramanian, V. Ramdesigan, P. W. C. Northrop, S. De, B. Suthar, and M. T. Lawder, *Systems and Methods for Improving Battery Performance*, US 10,037,395 B2, (2018).
73. Sion Power Lithium Sulfur Batteries Soar to New Heights, [Online, accessed 2019-05-01].
74. E. Fisler, and A. Datta, Fundamental Studies of Lithium Sulfur Batteries for eVTOL Aircraft, *Proceedings of Vertical Flight Society Forum 75*, Paper 75-2019-0341, Philadelphia, PA, May 2019.
75. M. Hagen, D. Hanselmann, K. Ahlbrecht, R. Maça, D. Gerber, and J. Tübke, *Adv.*

Energy Mater., **5** (2015).

76. W. Garvey, J. Salerno, and M. McMillin, MagniX Promises Electric Motor For Cessna 208 Caravan, [Online, accessed 2019-05-01].
77. B. Schmidt, California startup converts Cessna plane to electric, [Online, accessed 2019-05-01].
78. A. Fotouhi, D. J. Auger, K. Propp, S. Longo, and M. Wild, *Renew. Sustain. Energy Rev.*, **56**, 1008–1021 (2016).
79. G. J. Offer and M. Wild, Lithium Sulfur Batteries, p. 149, John Wiley & Sons, New Jersey (2019).
80. D. Adair, K. Ismailov, Y. Massalin, and Z. Bakenov, *Mod. Environ. Sci. Eng.*, **2**, 246–250 (2016).
81. D. I. Stroe, V. Knap, M. Swierczynski, and E. Schaltz, *ECS Trans.*, **77**, 467–476 (2017).
82. D. Bernardi, E. Pawlikowski, and J. Newman, *Electrochem. Soc. Ext. Abstr.*, **84–2**, 164–165 (1984).
83. C. R. Pals and J. Newman, *J. Electrochem. Soc.*, **142**, 3282 (1995).
84. E. V. Kuz'mina, E. V. Karaseva, N. V. Chudova, A. A. Mel'nikova, and V. S. Kolosnitsyn, *Russ. J. Electrochem.*, **55**, 978–988 (2019).
85. F. Yun, W. Jin, L. Tang, W. Li, J. Pang, and S. Lu, *J. Electrochem. Soc.*, **163**, A639–A643 (2016).
86. C. D. Parke, A. Subramaniam, V. R. Subramaniand, and D. T. Schwartz, *ChemElectroChem*, **8**, 1098–1106 (2021).
87. J. Newman and W. Tiedemann, *AIChE J.*, **21**, 25–41 (1975).

88. What Is The Genetic Algorithm?, [Online, accessed 2021-06-03].

89. Z. Jaadi, A Step-by-Step Explanation of Principle Component Analysis (PCA), [Online, accessed 2021-06-01].